Numerical analysis of Bow Tunnel Thruster Performance

Anoop Mohan

Master of Science Thesis

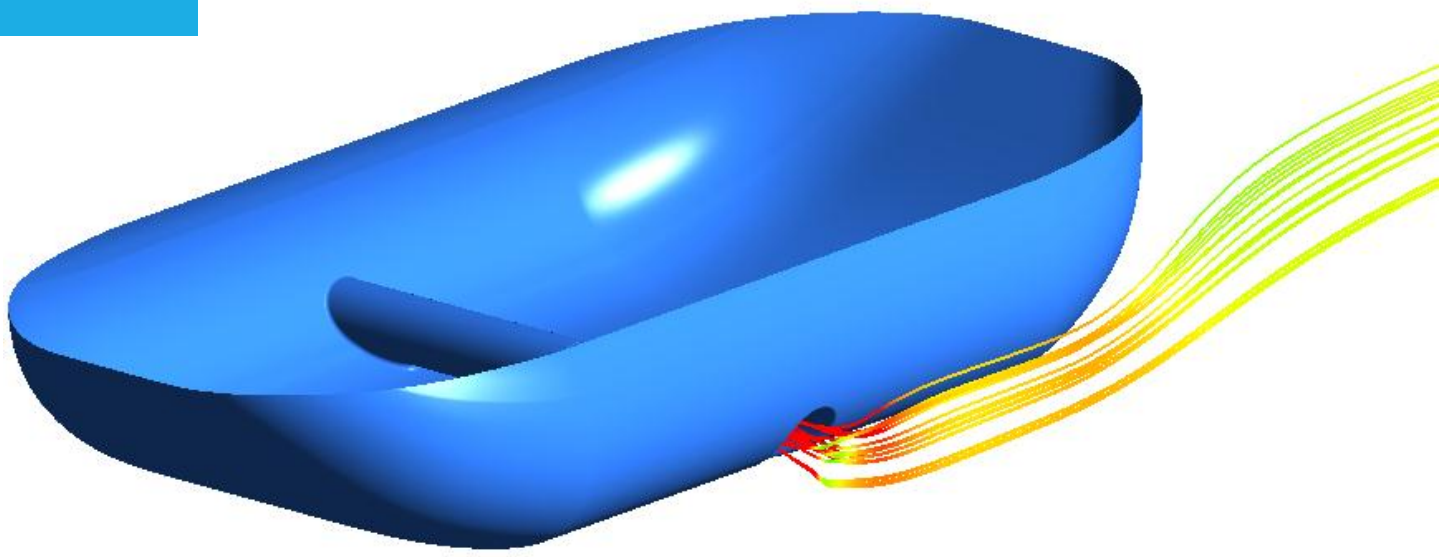

TU Delft

Challenge the future

Numerical Analysis of Bow Tunnel Thruster Performance

Master of Science Thesis

By

Anoop Mohan

in partial fulfillment of the requirements for the degree of

Master of Science

in Marine Technology – Track Science – Specialization Ship Hydromechanics (MT – SC - SH)

at the Delft University of Technology, Faculty of Mechanical, Maritime and Materials Engineering to be defended publicly on Tuesday April 4, 2017 at 1:30 pm.

Student number:	1542400	
Thesis committee:	Prof. dr. ir. R. H. M. Huijsmans	TU Delft
	Prof. dr. ir. T. J. C. van Terwisga	TU Delft
	Dr. ir. M. Godjevac	TU Delft
	Dr. ir. E. A. Munts	Royal IHC

Abstract

A previous work at Royal IHC, following the observation from sea trials of trailing suction hopper dredgers (TSHD) that the turning performance of bow tunnel thrusters significantly reduced at slow forward speeds, studied the flow behaviour and performance of bow tunnel thrusters at slow forward speeds using Computational Fluid Dynamics (CFD). Simulations were performed, on model scale, first with a simplified wedge model of a containership and then with a simplified wedge model of a TSHD with the thruster modelled by an actuator disk. The numerical results deviated significantly from experimental results from literature. The present work aims to investigate this deviation. Simulations are also performed with a full thruster unit to compare with the actuator disk approach. Also, possible improvement in thruster effectivity is explored by altering the tunnel geometry of the TSHD wedge.

First, a grid convergence study is performed on the containership wedge. Next, simulations are carried out for a range of forward speeds - for selected thrusts for the actuator disk approach, and corresponding rpm's for those thrusts for a full thruster unit. In case of the actuator disk approach, the numerical results show a steady increase of transverse force (F_y) with increasing forward speed, contrary to observations in sea trials. The circulation around the wedge, resulting from interaction of the jet from the tunnel and the cross-flow due to the forward speed, results in the wedge to behave as a slender body in a flow. This results in a transverse force, analogous to Kutta-Joukowski lift, that results in increased F_y. A full thruster unit in place of the actuator disk result in a different flow behaviour and variation of F_y with forward speed. In this case, an initial decline in F_y is observed before it increases monotonically. Comparison with experimental result of the containership wedge and numerical results by both actuator disk and thruster unit show considerable deviation. The transverse force due to the circulation around the hull presents a plausible explanation.

The conclusions from the grid convergence study for the containership model are utilized in meshing the TSHD wedge. Simulations performed for a range of forward speeds, first with actuator disk approximation, indicated lowered thruster performance as was observed in sea trials. The pressure contours over the hull imply that the resultant of the forces around the inlet – due to low pressure caused by high velocities of the flow into the tunnel – and those around the outlet – due to low pressure caused by high velocities of outflow – is such that there is a net thrust deduction. Simulations with thruster unit also show lowered thruster effectivity.

The tunnel of the TSHD wedge is then given a forward bend of 45^o at the tunnel inlet and outlet in order to explore the possibility of improving thruster performance. It is expected that the changed geometry will result in better inflow at tunnel inlet, and the action of the cross-flow on the jet will result in a 'straightened' jet with lesser interaction with the hull compared to a jet from a straight tunnel. The CFD results, with actuator disk approximation, indicate that thruster effectivity improves in case of higher forward speeds and reduces for lower speeds. It is advisable to perform the study with smaller tunnel bending angles such that the jet-flow interaction is favourable for the entire range of speeds.

Acknowledgments

This thesis is the culmination of an year of research - initially at IHC MTI, Delft and then for the most part at Royal IHC, Kinderdijk – which I can only describe as a fruitful learning experience.

I am indebted to Royal IHC for the opportunity and the facilities for my MSc thesis. Special thanks are due to León Seijbel and Edwin Munts who selected me for the position. Edwin also guided me throughout the project with great patience, dedication and attention to detail. He helped me define the goals of the project and familiarise with ANSYS ICEM CFD and CFX. The many discussions I had with Edwin, and his feedback and overall support were immensely helpful. He also showed me a work ethic which I find worth emulating. Many thanks to my colleagues at Delft including Nikos, Mark and Vivek with whom I share a friendly camaraderie. At Kinderdijk, Jeroen, Bram, Remy, Alex, Leonard, Ron, and David contributed to a pleasant working environment. The daily trips with Jeroen saved me a lot of time, effort, and of course, money.

I am grateful to Professors Tom van Terwisga and René Huijsmans for the guidance and support they have provided throughout the thesis work, and for providing valuable insights into hydromechanics. Their advices were instrumental in enhancing the quality of the thesis. The feedback I received on presenting my results was particularly beneficial. I gratefully acknowledge Dr. Milinko Godjevac for being part of my thesis committee at a short notice. Lourdes Gallastegui, my academic counsellor at 3mE, has been a constant source of encouragement as I faced quite a few personal hurdles in my academic journey. John Stals, the Central Student Counsellor, also provided me with immense support. My sincere gratitude to Peter Naaijen for his time and effort when I was starting out in Delft. I am also grateful to Dr. Arie Romeijn, the coordinator of my track, who has been patient and accommodating.

To my friends Jiya, Ebin, Pradeep and Mo, I am forever in your debt for helping me endure when the going got tough. To Aravind, Ashkar, Anupa, and my wonderful friends in Aachen, I am grateful for giving me emotional refuge and moral support without my ever having to ask. Many thanks are due to Ratnakar Gadi and Tommy Olsen for those thoroughly enjoyable and educative group assignments.

Finally, I owe much to my parents and brother who have been unwavering in their support. They have always shared my dreams and never failed to encourage my endeavours to bring them to fruition. For this, and for everything else, I cannot thank them enough.

Contents

List of Figures

List of Tables

Nomenclature

A_{tunnel}	Cross-sectional area of the tunnel	$[m^2]$
$C_{F_{TH}}$	Thrust deduction factor	[-]
$C_{F_{Nienhuis}}$	Force coefficient as defined by Nienhuis	[-]
D	Diameter of the tunnel	$[m]$
F_s	Safety factor in uncertainty estimation	[-]
F_y	Transverse force on the hull	$[N]$
h	Typical cell size in a grid	$[mm]$
K_T	Thrust coefficient	[-]
m	Ratio of mean jet velocity and forward ship speed	[-]
n	Revolutions per minute (rpm) of the thruster	[-]
T	Thrust	$[N]$
$T_{full\ scale}$	Thrust in case of full scale	$[N]$
T_{model}	Thrust in case of model scale	$[N]$
U_ϕ	Uncertainty (applies to F_y in this work)	$[N]$
V_{AD}	Volume of the actuator disk region	$[m^3]$
V_{jet}	Mean jet velocity	$[m/s]$
V_s	Forward ship speed	$[m/s]$

Greek Letters

α_1, α_2	Coefficients in the formulation for error estimation	[-]
ϵ_ϕ	Discretization error (applies to F_y in this work)	$[N]$
Φ_0	Estimate of the exact solution (for F_y in this work)	$[N]$
Φ_i	Any integral or other functional of a local flow quantity (F_y in this work)	$[N]$
Φ_{fit}	The value obtained with the second order polynomial fit	$[N]$
λ	Length scale	[-]

σ	Standard deviation	$[N]$
ρ	Density	$[kg/m^3]$
Δ_ϕ	Data range parameter	$[N]$

1 Introduction

Bow tunnel thrusters enhance manoeuvrability of vessels during mooring and while operating at slow speeds. They can be designed to provide additional station keeping power when dynamic positioning. In case of trailing hopper dredgers wherein the present work is especially relevant, the thrusters are important for slow speed manoeuvring and course keeping. Figure 1.1 shows a typical bow tunnel thruster.

Figure 1.1 Bow tunnel thruster with protection grid. Picture adapted from [4].

It was observed in a study conducted by MARIN for Royal IHC[6] that the turning performance by using the bow thrusters is significantly reduced when the dredging vessel under consideration was moving forward at a speed of 5 knots compared to when the ship was at rest. The decrease in effectivity of tunnel thrusters with increasing forward speed has been a subject of several studies[1,2,4].

1.1 Summary of the previous work

Although the performance of lateral tunnel thrusters on ships has been investigated by many researchers for decades, Computational Fluid Dynamics modelling is a relatively late entrant in the scene. Among the earliest works are those by Ridley[9] wherein an attempt was made to correlate full-scale data to model test data pertaining to conditions with forward speed and operational thruster. Beveridge[7] examined the interaction between the ambient flow of a hull and bow thruster inflow and outflow theoretically and experimentally, and concluded that it is bow-thruster outflow, not inflow, which is an important factor in bow-thruster jet interaction at forward speed. Baniela[4] studied the effectiveness of a bow tunnel thruster with slow speed ahead, describing the general reasons for the decrease in performance, and explored anti-suction tunnel as a possible design option that can improve the effectiveness. Karlikov and Sholomovich [12] studied the interaction of thruster-generated jets with the flow near the hull at low flow velocities.

Nienhuis[1] analysed the effectivity of thrusters with numerical and experimental tools. The effects of ship speed and current on the lateral forces developed by the tunnel thruster was

considered in some detail. For this purpose, model tests were performed on a wedge-shaped hull hereafter referred to as the Nienhuis wedge. The experimental results were used to validate the computations.

Motivated by the observation at Royal IHC[6] that the turning ability using a bow tunnel thruster is significantly decreased in forward speed conditions, the performance of a tunnel thruster was studied for varying tunnel cross-sections using CFD by Schaap[2]. The effectivity of the thruster is represented by the thrust deduction factor C_F which is calculated from the transverse forces on the hull and the thrust. CFD simulations are performed for a simplified wedge model of a containership with a bow tunnel thruster, as defined by Nienhuis[1], and validated with model test results provided by Nienhuis[1]. Upon validation, while qualitative validity is established, large differences are observed between the quantitative results of the model tests from [1] and those of CFD simulations [2]. In these simulations, the tunnel thruster was modeled by an actuator disk. Simulations are then presented for the hull geometry of interest – a hopper wedge model based on a trailing suction hopper dredger - wherein the transverse forces are obtained and compared for varying bow tunnel cross-sections. A systematic tunnel cross-section variation is derived and three different shapes(SAABB cross section series) are computed at different ship speeds: a circular cross-section (S1010A), flattened cross-section (S0610A) and a streamlined cross-section (S0602A), as shown in Figure 1.2.

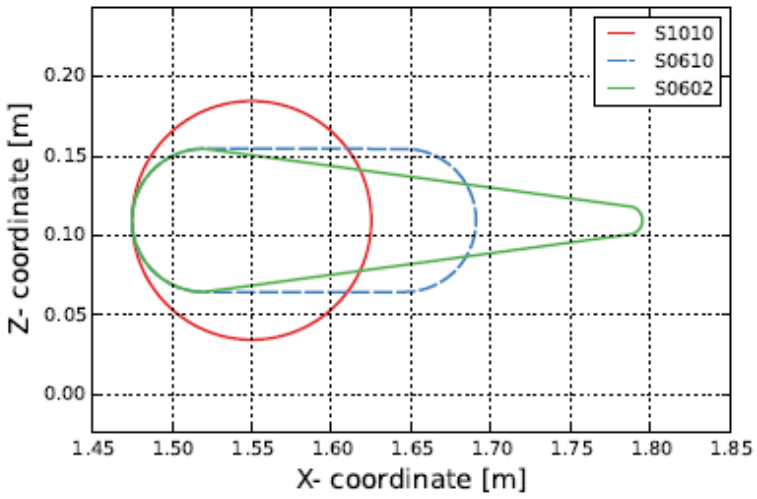

Figure 1.2: SAABB cross section series used in the study. From [2].

It is observed that the thruster effectivity is improved by increased transverse force although resistance is increased as well. The study by Schaap[2] forms a basis to the current work.

1.2 Objectives

The objective of the present work is to further investigate the deviation between the numerical and experimental results of thruster effectivity as observed in the work by Schaap[2]. In particular, the effect of the actuator disk approach is investigated by including a full thruster unit in the CFD simulations. Additionally, another concept for improving thruster efficiency is explored, namely that of a forward bent tunnel inlet and outlet.

1.3 Problem approach

Simulations can be performed for Nienhuis wedge with a tunnel thruster approximated with an actuator disk in order to do a grid convergence study. The “converged” grid is then used to study tunnel thruster effectivity for a range of forward ship speeds. The actuator disk is then replaced by a thruster (including propeller, hub, and strut) and simulations performed. The latter CFD results are expected to correspond better to the available experimental results. The 2 approaches may be compared for the same forward speed-thrust combinations. The tunnel thruster effectivity for a Hopper wedge with a full thruster can then be analysed.

1.4 Tools

As opposed to the work by Schaap[2], the present work is carried out using ANSYS software. The geometry is meshed with ANSYS ICEM CFD. The resulting unstructured mesh consists of tetrahedral and prism elements. ANSYS ICEM CFD generates hybrid tetrahedral grids consisting of layers of prism elements near the boundary surfaces to better model the near-wall physics and tetrahedral elements in the interior. The simulations are then performed using ANSYS CFX, which employs vertex-based finite volume method to solve the Reynolds Averaged Navier Stokes equations.

1.5 Outline of the report

In chapter 2, the numerical formulation is presented, including the governing equations and the solution procedure. Fundamentals of Computational Fluid Dynamics, including Reynolds averaging and turbulence modeling are summarized. In chapter 3, CFD results are presented for the Nienhuis wedge operating at low forward speeds, with a functioning tunnel thruster. In the initial section, the thruster is modelled by an actuator disk in order to compare the results with those from [2]. Next, the actuator disk is replaced by a full thruster unit. Chapter 4 describes the simulations for a hull corresponding to a Trailing Suction Hopper Dredger, referred to as Hopper wedge. As in chapter 3, the actuator disk approximation as well as a full thruster unit are used to investigate the action of tunnel thruster in forward speed conditions.

2 Numerical Formulation

A theoretical background relevant to the present work is provided. It entails an introduction to Computational Fluid Dynamics (CFD), with emphasis on finite volume method used by ANSYS CFX. An overview of Reynolds-Averaged Navier Stokes(RANS) equations, the discretization method ANSYS CFX solves, and a brief description of turbulence models are included.

2.1 Concepts Underlying CFD

CFD deals with the prediction of fluid flow, heat and mass transfer, chemical reactions, and related phenomena by solving numerically the set of governing mathematical equations.

2.1.1 Governing Equations

The motion of a fluid can be described completely in terms of the Navier-Stokes or momentum equations supplemented by the continuity equation(conservation of mass) and, if required, the energy equation(conservation of energy). For an incompressible fluid, the continuity equation is given as:

$$\nabla . \overrightarrow{V} = 0 \tag{2.1}$$

and the momentum equation, as:

$$\frac{\partial \vec{V}}{\partial t} + \left(\vec{V} . \nabla\right)\vec{V} = -\frac{1}{\rho}\nabla p + \nabla . \tau \tag{2.2}$$

where $\vec{V}$ is the velocity vector, ρ is the density, p the pressure and τ the stress tensor.

These equations (along with the conservation of energy equation) form a set of coupled, nonlinear partial differential equations. For most engineering problems, it is not possible to solve these equations analytically. However, approximate computer-based solutions can be obtained for the governing equations for a variety of engineering problems. This is the crux of Computational Fluid Dynamics (CFD).

2.1.2 Strategy of CFD

Broadly, the strategy of CFD is to replace the continuous problem domain with a discrete domain using a grid. In the continuous domain, each flow variable is defined at every point in the domain. In the discrete domain, each flow variable is defined only at discrete points. CFD simulations involve discretization of the partial differential equations and numerically solving the resulting algebraic equations. Several CFD techniques exist, such as Finite Difference, Finite Element, Finite Volume and Spectral methods. The main difference between the techniques are based on the discretization process and the way in which the flow variables are approximated.

Finite Difference method, for instance, describes the unknowns of a flow problem by means of point samples at the node points of a grid. Finite difference approximations of derivatives of flow variables in terms of the nodal values are generated using truncated Taylor series. The derivatives appearing in the governing equations are replaced by finite differences resulting in algebraic equations for the values of the flow variables at each grid point. Finite Element

methods use simple piecewise functions valid on elements to describe the local variations of unknown flow variables. Spectral methods approximate the unknowns by means of truncated Fourier series or series of Chebyshev polynomials.

Of the solution methods that CFD codes use, the Finite volume technique is the most well-established, and is the one used by ANSYS CFX. The method was originally developed as a special finite difference formulation.

2.1.3 Finite Volume Method

Once a mesh has been formed, the region of interest, referred to as the computational domain, is divided into small control volumes where the conservation law will be applied. This division can be done in two ways, as shown in Figure 2.1, depending on where the solution is stored. One is the cell-centered finite volume scheme where the solution is stored at the center of each cell. In this case, the cell is the control volume. The other one, used by ANSYS CFX, vertex-based finite volume scheme where control volumes are constructed around each mesh vertex. In Figure 2.1, the shaded regions represent the control volumes.

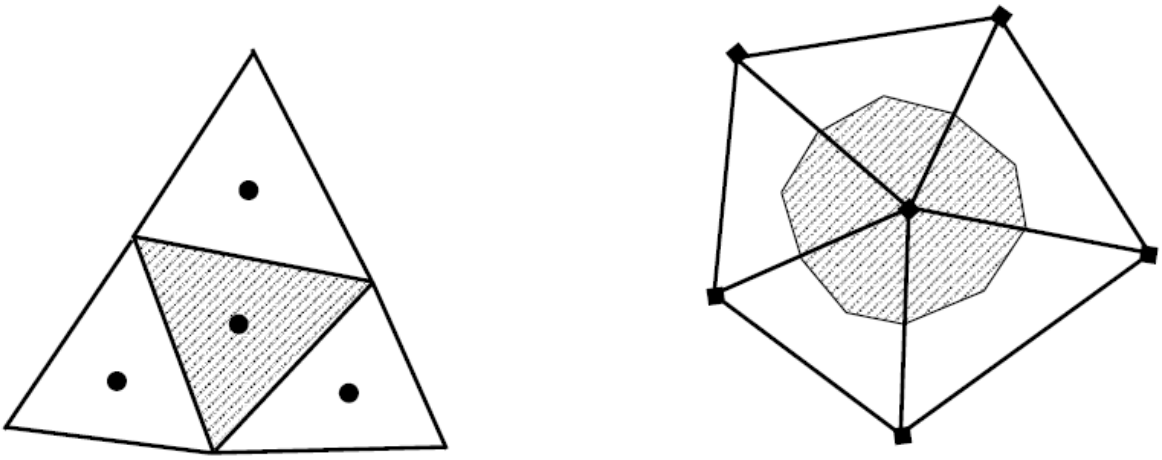

(a) (b)

Figure 2.1 Illustration of cell-centered (a) and vertex-centered (b) type control volume constructions. Adapted from [25]

The equations are discretized and solved iteratively for each control volume. As such, approximate values of each variable at discrete points throughout the domain are obtained. A full picture of the flow behaviour is thus derived. In the finite volume approach, the integral form of the conservation equations are applied to each control volume to get discrete equations for the node. For example, the integral form of the continuity equation for steady, incompressible flow is

$$\int_S \vec{V}.\hat{n}\ dS = 0 \tag{2.3}$$

where S refers to the surface of the control volume and $\hat{n}$ is the outward normal at the surface. The physical implication of the equation is that the net volume flow into the control volume is zero. In vertex-based approach, the velocity (or any other flow variable, for that matter) are then described by simple piecewise polynomial functions. The integral equation is then

transformed into an algebraic equation. Similarly, discrete equations can be obtained for conservation of momentum (and energy, if required). Boundary conditions are then applied and the system of discrete equations solved iteratively to obtain a sufficiently converged solution.

2.1.4 Modeling of Turbulence

Turbulent flows are characterized by large, random fluctuations in velocity and pressure in both space and time. Though the flows are highly unsteady and contain large range of scales, the mean or average motion is usually well-defined. Most engineering problems involve turbulent flows and thus turbulence modeling is important in their CFD solutions.

RANS equations

Reynolds Averaged Navier Stokes (RANS) equations makes feasible the estimation and resolution of all the scales of turbulent flows. The reduced computational requirements for the RANS equations, while still significant, are orders of magnitude less than that required for the original Navier-Stokes equations. The assumption (known as the Reynolds decomposition) behind the RANS equations is that the time-dependent turbulent velocity fluctuations can be separated from the mean flow velocity. If the velocity field $\vec{V}$, as seen in equations 2.1 through 2.3, has the components (u, v, w), the Reynolds decomposition is given as

$$u(t) = \bar{u} + u'(t) \tag{2.3}$$

which implies, $\vec{V} = \bar{\vec{V}} + \vec{V}'(t)$, where $\vec{V}'$ has the components (u', v', w').

Applying this decomposition to the Navier Stokes equations results in RANS equations given as:

$$\nabla . \overrightarrow{\bar{V}} = 0 \tag{2.4}$$

$$\frac{\partial \overrightarrow{\bar{V}}}{\partial t} + \left(\overrightarrow{\bar{V}} . \nabla\right) \overrightarrow{\bar{V}} = -\frac{1}{\rho} \nabla \bar{p} + \frac{1}{\rho} \nabla . (\bar{\tau} - \rho \overline{\vec{V}' \vec{V}'}) \tag{2.5}$$

This transform introduces a set of unknowns called the Reynolds stresses, given by $\overline{\vec{V}' \vec{V}'}$, which are functions of the velocity fluctuations. A turbulence model is required to estimate the Reynolds stresses and produce a closed system of solvable equations.

Turbulence modeling

Based on the turbulent-viscosity hypothesis, a number of models are used to estimate the Reynolds stresses. The zero equation models are very robust, as they are calculated algebraically from the flow variables, and do not require solving ordinary differential equations. However, these models are not very accurate. The one equation models are those in which the transport equations are solved for one quantity, the turbulent kinetic energy, k. They are more accurate than the one equation models. But, they have the drawback of being incomplete since they require a length scale, a flow dependent quantity, which needs to be specified [16].

The two equation models involve transport equations being solved for two turbulence quantities. They are more complete as they do not require any flow dependent specification. $k - \epsilon$ and $k - \omega$ are the most widely used two-equation models used in commercial CFD codes [26].

In case of $k-\epsilon$, the transport equations are solved for the two quantities: the turbulent kinetic energy k and the turbulent viscous dissipation rate ϵ. It models turbulence based on how the turbulent energy is dissipated by the eddies in the form of heat. $k-\epsilon$ model gives good results in the free stream region, has a good convergence rate and requires lesser memory than equivalent models. But k goes to zero at the walls, hence resolution is poor close to the walls and in regions of adverse pressure gradients. Hence $k-\epsilon$ is not suitable for systems with rotating fluids, boundary layer separations, or geometries with curved surfaces.

The $k-\omega$ model is based on a relation between the turbulent kinetic energy k and the turbulent frequency ω. $k-\omega$ deals well with domains having adverse pressure gradients. Hence it is well suited to the near wall regions (boundary layer and viscous sub-layers). But it can have a strong influence and sensitivity on the incoming turbulence length-scale. It is also not as good in the free stream region as the $k-\epsilon$ model. It takes up more time for convergence and more memory than the $k-\epsilon$ model.

ANSYS CFX provides numerous common two-equation turbulence models and Reynolds–stress models. The present work employs the widely tested shear stress transport (SST) turbulence model. The SST model is as economical as the widely used k-ε model, but it offers higher fidelity, especially for separated flows, providing excellent answers on a wide range of flows and near-wall mesh conditions via blending of $k-\omega$ and $k-\epsilon$ formulations. A description, along with equations, of the model is provided in Appendix A. The SST model also includes an automatic wall treatment for maximum accuracy in wall shear. The automatic wall treatment switches between a low-Reynolds number formulation (i.e. direct resolution of the boundary layer) at low y^+ (dimensionless wall distance) values and a wall function approach at higher y^+ values, thus allowing the user to take advantage of a fine near-wall mesh when present.

3 CFD study of the Nienhuis wedge

The CFD study will first include simulations with the Nienhuis wedge shown in Figure 3.1, with dimensions as given in Table 3.1. The thruster is initially approximated by an actuator disk, and then by a propeller including hub and strut. The computations are validated using results from literature[12].

For the actuator disk case, transient simulations are employed whereas in the case with the full propeller, a frozen rotor (steady state) approach is used to model the rotating propeller. Transient simulations for the latter case for selected ship speeds gave average values of solutions close to the values obtained with frozen rotor approach. Hence, steady state simulations are deemed sufficient to capture the flow field, and there is no need to resort to the time-consuming transient simulations.

3.1 Nienhuis wedge with Actuator disk

In order to perform simulations on the wedge, an optimal grid has to be obtained. A grid convergence study, as given in section 3.1.2, yields the required optimal grid which is used for the simulations thereafter. Prior to the description of the grid convergence study, the computational model is described in the next section.

3.1.1 Computational model

Domain

The computational domain is shown in Figure 3.2, its dimensions being 9L x 8L x 2.5L, where L is the ship length. The coordinate system places the origin at the bow, on the baseline. The x-axis points from bow to stern, the positive y-axis is towards starboard, and the positive z-axis points upwards. The jet from the actuator disk delivers is directed in the positive y-direction.

An actuator disk is used in the simulations to model the thrust of the thruster. A body force is applied in the region occupied by the thruster as highlighted in Figure 3.5. The body force in the actuator disk region is given as

$$F_b = \frac{T}{V_{AD}} \tag{3.1}$$

where T is the applied thrust and V_{AD} the volume of the actuator disk. Since the body force is directed in the positive y-direction, it is implied that the thrust acts in the opposite direction. For thrust deduction, the transverse force on the hull must be obtained in the direction opposing the thrust, i.e. in the positive y-direction.

The thrust is assumed to have a uniform distribution radially over the actuator disk, with no tangential forces. The actuator disk geometry is shown in Figure 3.4 and the dimensions are as given in Table 3.2. The dimensions correspond to the propeller dimensions as employed in the experiments by Nienhuis [1].

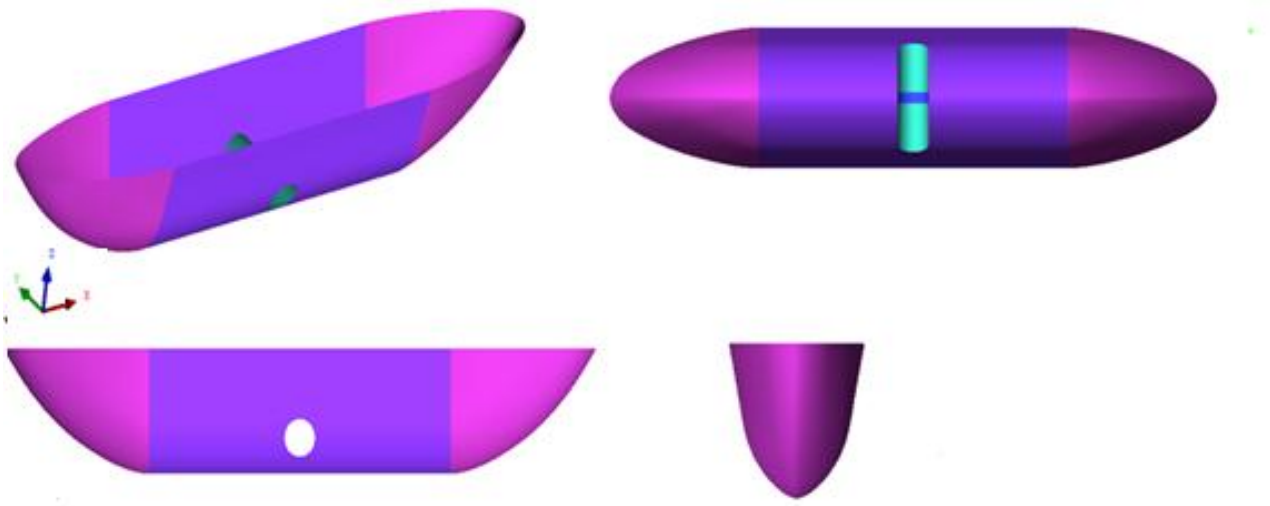

Figure 3.1 Nienhuis wedge

Particular	Unit	
Length straight section	[mm]	1500
Length overall	[mm]	3100
Beam	[mm]	546
Draft	[mm]	508
Tunnel diameter	[mm]	150
Tunnel center z location	[mm]	152

Table 3.1 Main particulars of the Nienhuis wedge

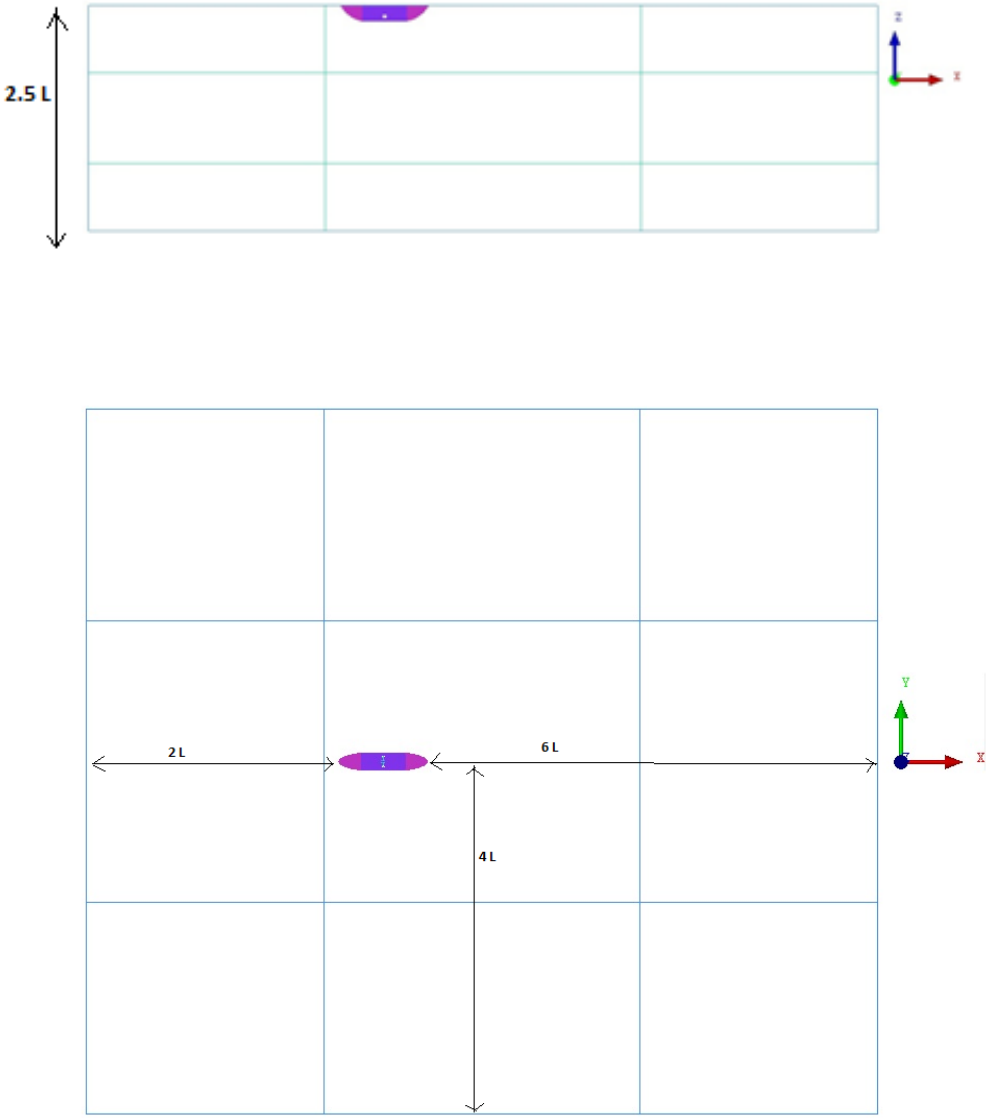

Figure 3.2 Overview of the computational domain

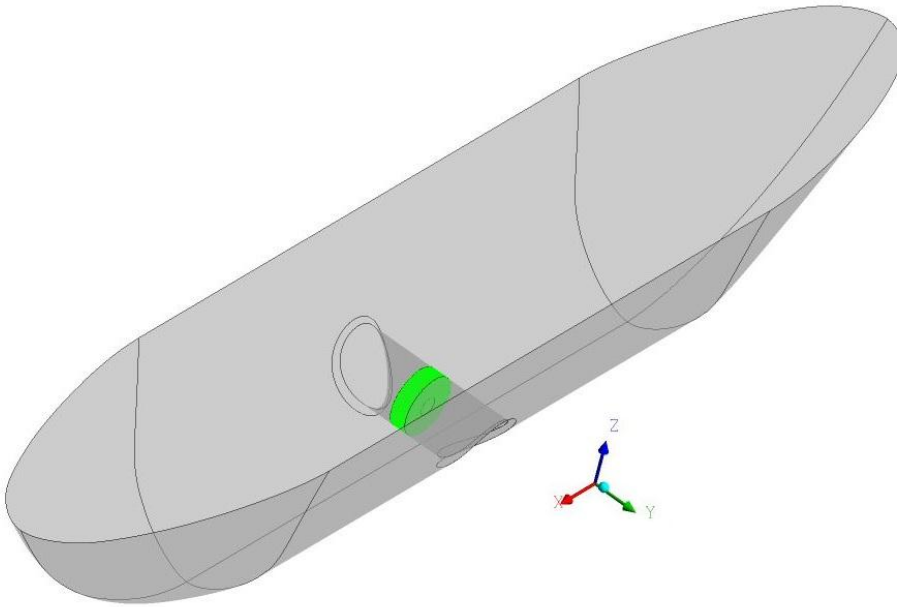

Figure 3.3 Actuator disk in the tunnel

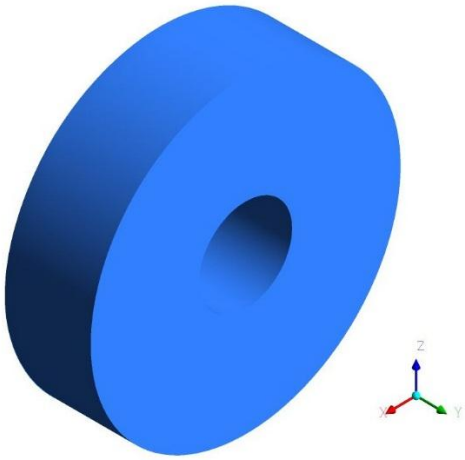

Figure 3.4 Geometry of the actuator disk

Particular	Unit	
Inner radius	[m]	0.0225
Outer radius	[m]	0.075
Thickness	[m]	0.0415
Center coordinates	[m]	1.55 0.0 0.152

Table 3.2 Particulars of the actuator disk

Computational approach

A transient approach is employed for computations with the propeller modelled as an actuator disk wherein unsteady RANS equations (described in section 2.1.1) are solved using ANSYS CFX. Simulations are run until a converged solution is obtained.

Figure 3.5 shows an overview of the boundary conditions on the computational domain. The hull is set as a no-slip wall, while the water surface – the top of the domain – is treated as a free slip wall. The domain and hull are assumed to be stationary and a flow with velocity V_{ship} is imposed on the inlet boundary. On the outlet boundary a constant pressure is prescribed. On the sides of the computational domain, opening boundary condition with entrainment – suitable when flow direction is unknown - is imposed.

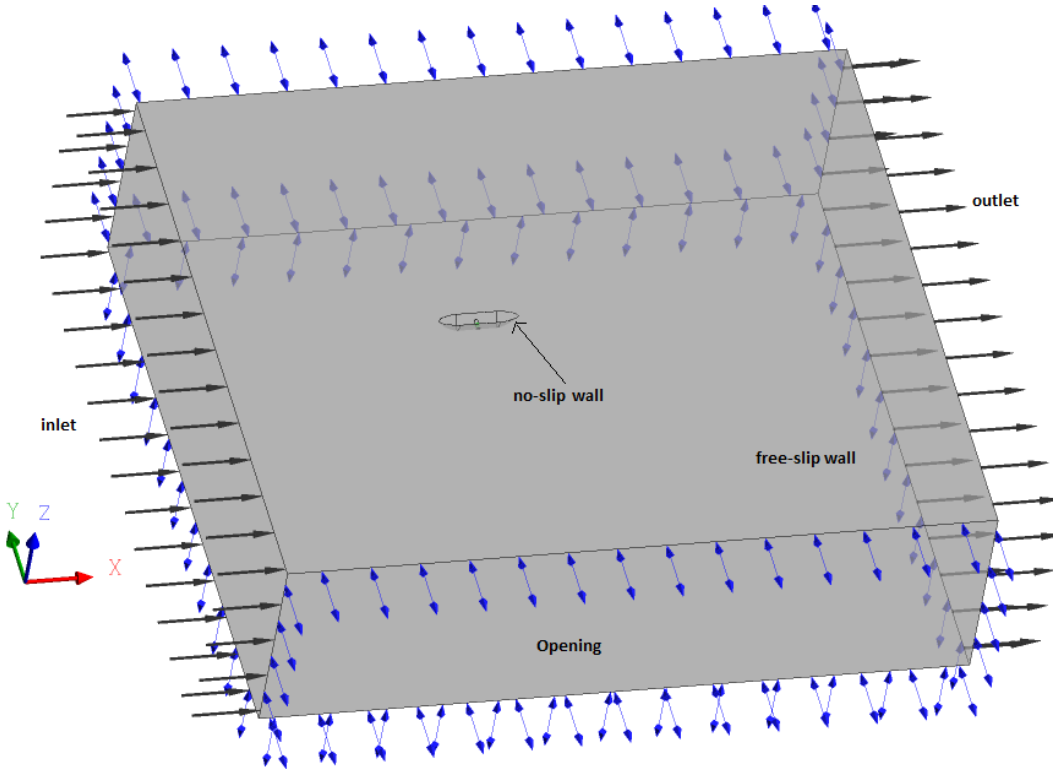

Figure 3.5 Overview of boundary conditions

Discretization

Second-order upwind discretization is used in both space and time. The turbulence model uses first-order upwind discretization.

3.1.2 Grid convergence study

A grid convergence study is performed to quantify the discretization uncertainty. The method by Eça and Hoekstra[11], explained in Appendix B, is used. The four systematically refined grids considered for this purpose are given in Figure 3.8. For simulations, the thrust delivered by the actuator disk and the forward speed of the ship are obtained based on the values taken from a full scale simulation typically for a trailing suction hopper dredger, as described in [6].

The relationship between the thrust and speed in full scale and model scale can be written in terms of the length scale $\lambda(=\frac{L_{full\ scale}}{L_{model}})$ as explained in Appendix A.

$$T_{full\ scale} = T_{model}\,\lambda^3 \tag{3.2}$$

$$V_{full\ scale} = V_{model}\,\sqrt{\lambda} \tag{3.3}$$

Based on the dimensions of the Nienhuis wedge and that of the trailing suction hopper dredger in [6], $\lambda \approx 40$. The hopper has a length ($L_{full\ scale}$) of 120 [m] and the actuator disk generates a thrust ($T_{full\ scale}$) of 114 [kN]. Thus, a thrust T_{model} = 1.78 N and the a forward speed V_{ship} = 0.4 m/s are calculated to be used in the simulations for the grid convergence study.

Alteration of hull geometry at tunnel ends

Initially, simulations were carried out with sharp tunnel edges at the intersection of the tunnel and the hull. In order to obtain grid convergence, three simulations on systematically refined grids were performed. Figure 3.6 shows the behaviour of F_y, the total lateral force on the ship, plotted against number of cells in each grid. A monotonic increase in F_y is noted with increasing refinement of the grids, indicating the absence of grid independence. Further investigation suggested that the sharp tunnel edges leading to flow separation at the locations as a possible reason for the behaviour. To avoid this effect, the tunnel ends were rounded by using a fillet between the tunnel and the hull as shown in Figure 3.7. Using this geometry, another grid convergence study was carried out for F_y.

Convergent behaviour is obtained with the new geometry using 4 grids, shown in Figure 3.8. Uncertainty – an interval containing the exact solution with 95% coverage - is estimated using the method by Eça and Hoekstra [11] (as described in Appendix B) is given in Table 3.3 and Table 3.4, and the results given in Figure 3.9.

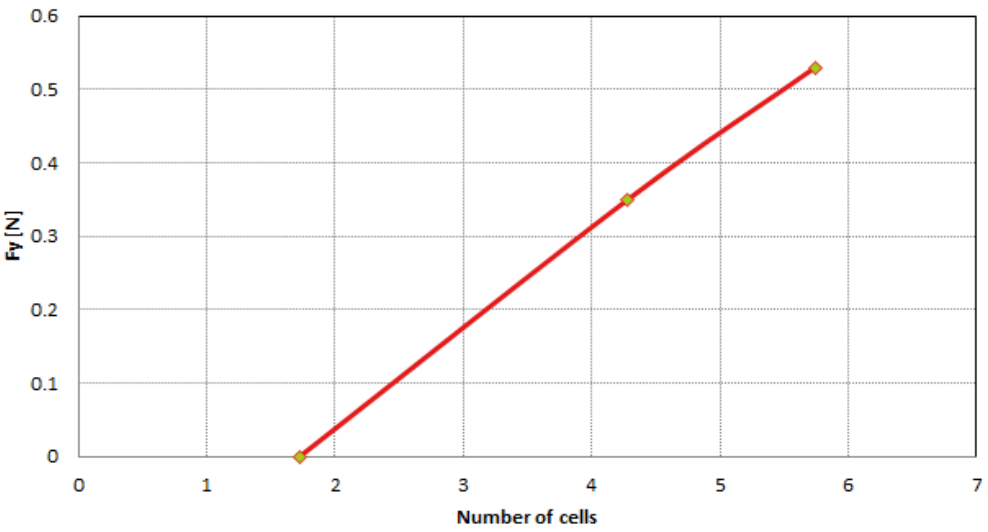

Figure 3.6 Lack of grid convergence for hull with sharp tunnel ends

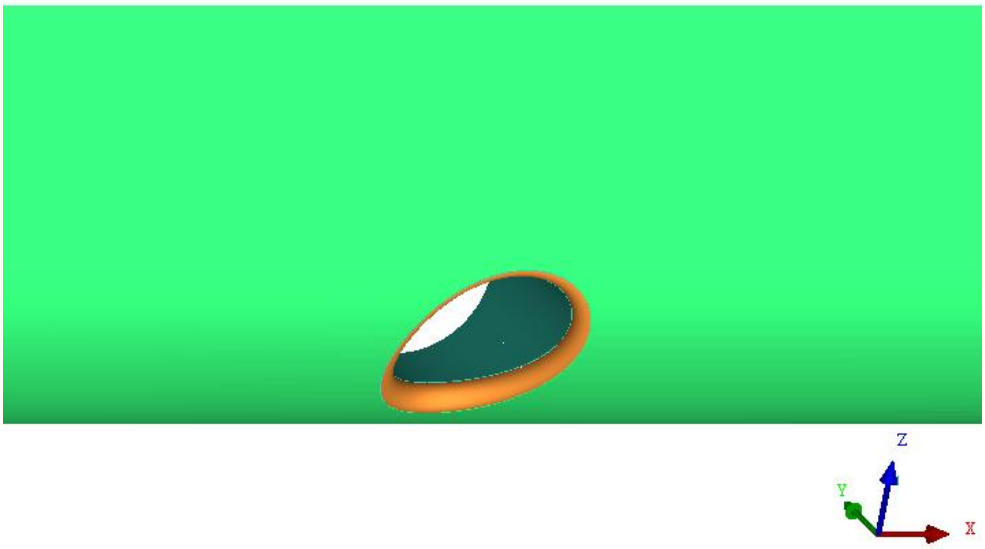

Figure 3.7 Altered hull geometry at tunnel ends

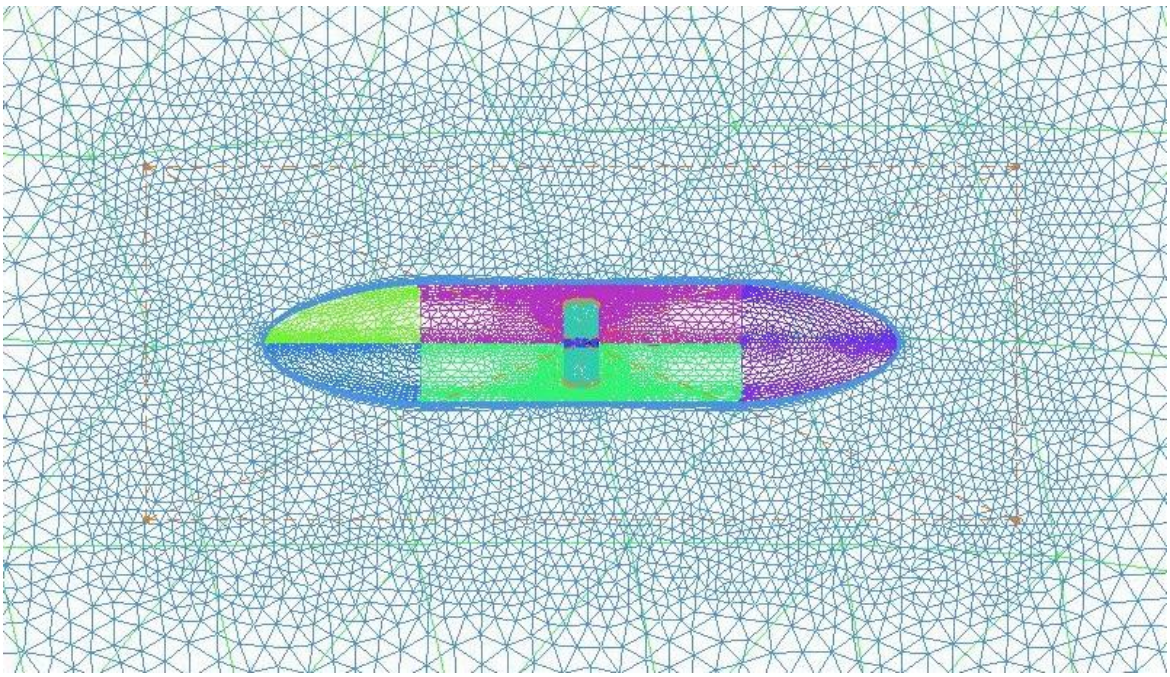

(a) Mesh 1. h = 64 mm. 732,975 cells.

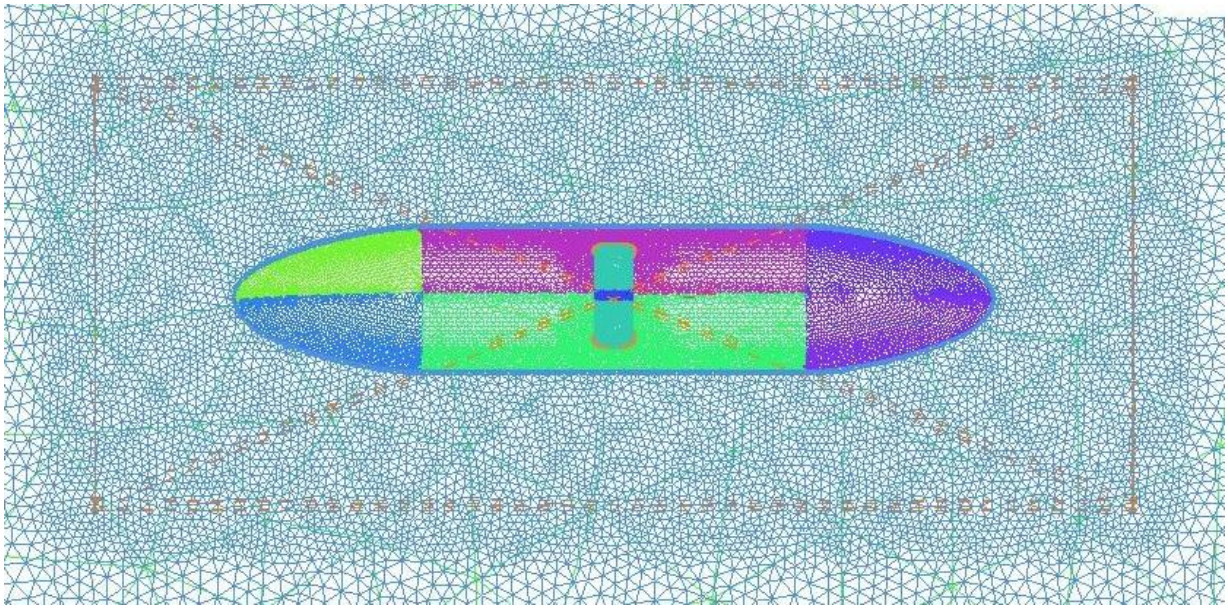

(b) Mesh 2. h = 32 mm. 7,741,850 cells

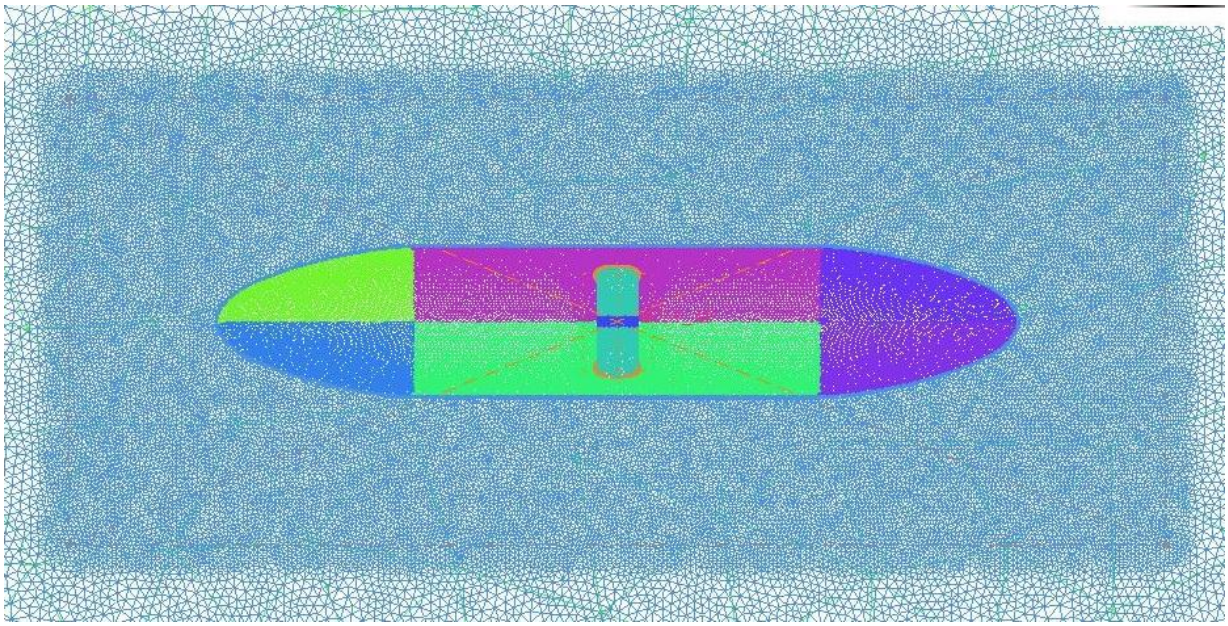

(c) Mesh 3. h = 16 mm. 16,532,590 cells.

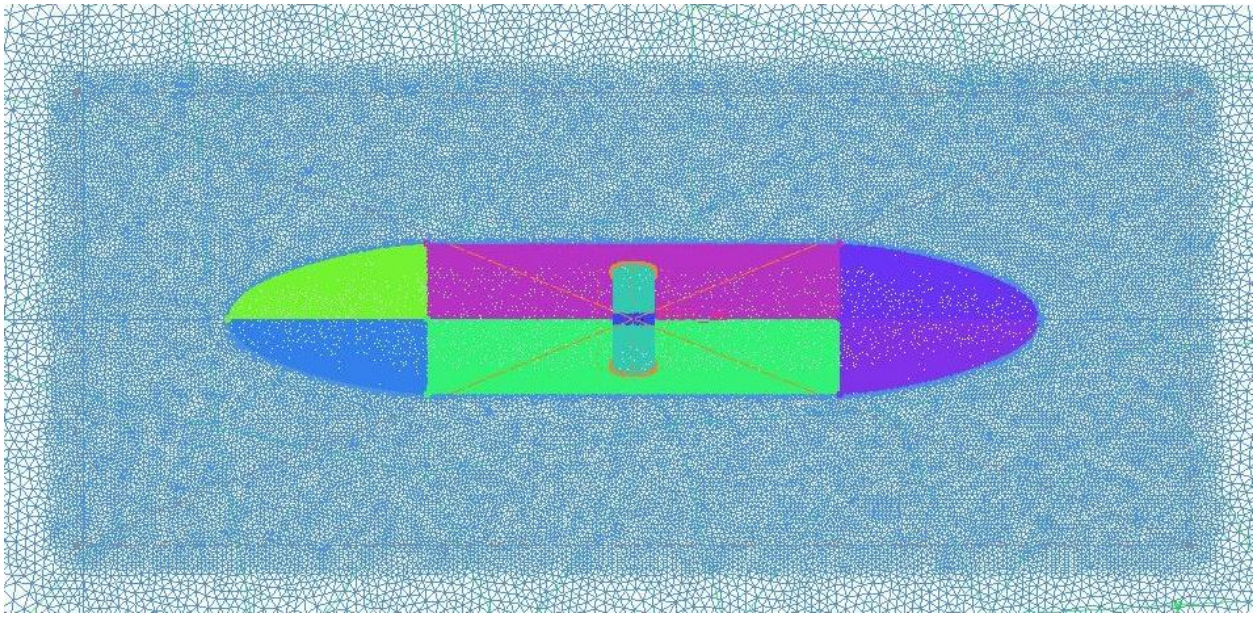

(d) Mesh 4. h = 8 mm. 17,415,165 cells.

Figure 3.8 The grids used in the grid study

σ	Δ_Φ	F_s
0.0415	0.0967	3

	h	Φ_i	Φ_{fit}	$\Phi_i - \Phi_{fit}$	ε_Φ	U_Φ
Mesh 1	64	-2.96	-2.96	-0.0023	0.272	0.859
Mesh 2	32	-2.77	-2.75	0.0165	0.082	0.303
Mesh 3	16	-2.67	-2.70	-0.0329	0.018	0.129
Mesh 4	8	-2.71	-2.69	0.0189	0.022	0.125

Table 3.3 Uncertainty estimation. Non-weighted approach

σ	Δ_Φ	F_s
0.0455	0.0967	3

	h	w_i	Φ_i	Φ_{fit}	$\Phi_i - \Phi_{fit}$	ε_Φ	U_Φ
Mesh 1	64	0.067	-2.960	-2.969	-0.009	0.246	0.792
Mesh 2	32	0.133	-2.770	-2.739	0.031	0.056	0.244
Mesh 3	16	0.267	-2.670	-2.701	-0.031	0.044	0.209
Mesh 4	8	0.533	-2.710	-2.701	0.009	0.004	0.067

Table 3.4 Uncertainty estimation. Weighted approach

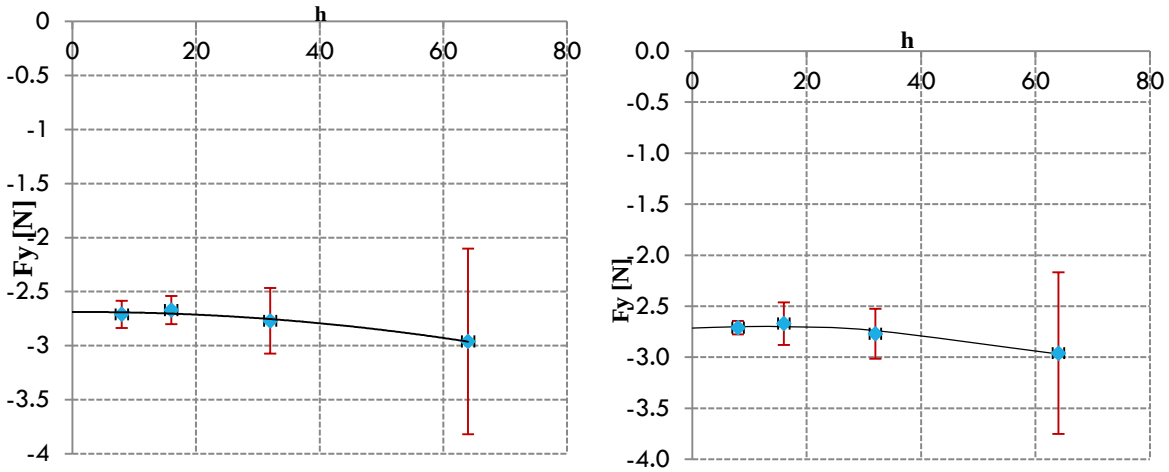

(a) (b)

Figure 3.9 Results of grid study using the method by Eça and Hoekstra [11]. Non-weighted (a) and weighted (b) approaches

Non-weighted approach(Table 3.3, Figure 3.9(a)) and weighted approach(Table 3.4, Figure 3.9(b)) are explained in Appendix B. It is noted that the standard deviation σ is slightly smaller for the non-weighted approach which implies the uncertainties obtained therein is relatively more reliable.

A possible reason for lack of convergence in case of original hull geometry with sharp tunnel-hull intersections is the flow separation at the sharp edges at tunnel inlet and exit. When the edges are made smooth with fillets, the boundary layer is able to follow the smooth turn in corner, thereby minimizing flow separation.

3.2 Investigations with Actuator Disk

After confirmation of grid convergence, the effect of forward speeds of the vessel on thruster performance was investigated. The computational model is as given in section 3.1.1, and mesh 2 is chosen as the optimally suited grid for the simulations. A constant thrust of 1.78 N, as in the previous section, is considered at first. A higher value of thrust, 10 N, is considered thereafter. The following forward speeds are considered: V_{ship} = 0.015 m/s, V_{ship} = 0.1 m/s, V_{ship} = 0.2 m/s, V_{ship} = 0.3 m/s, and V_{ship} = 0.4 m/s.

3.2.1 Computational Results

Thrust T = 1.78 N

The flow fields obtained for the different forward speed cases are given in Figure 3.11 through Figure 3.15. The bending of the jet towards the hull can be observed as forward speed increases. The deflection of the jet is observed to cause a redistribution of pressure as it becomes oriented in the longitudinal direction. The pressure contours on the hull can be compared for the cases with forward speeds with the minimum speed (nearly zero speed) case. Further, the hull can be split into different parts, as shown in Figure 3.16. The transverse forces on the various parts are

tabulated for each forward speed case. The redistribution of lateral forces on the hull due to forward speed can thus be better described, as given in Table 3.5 through Table 3.9.

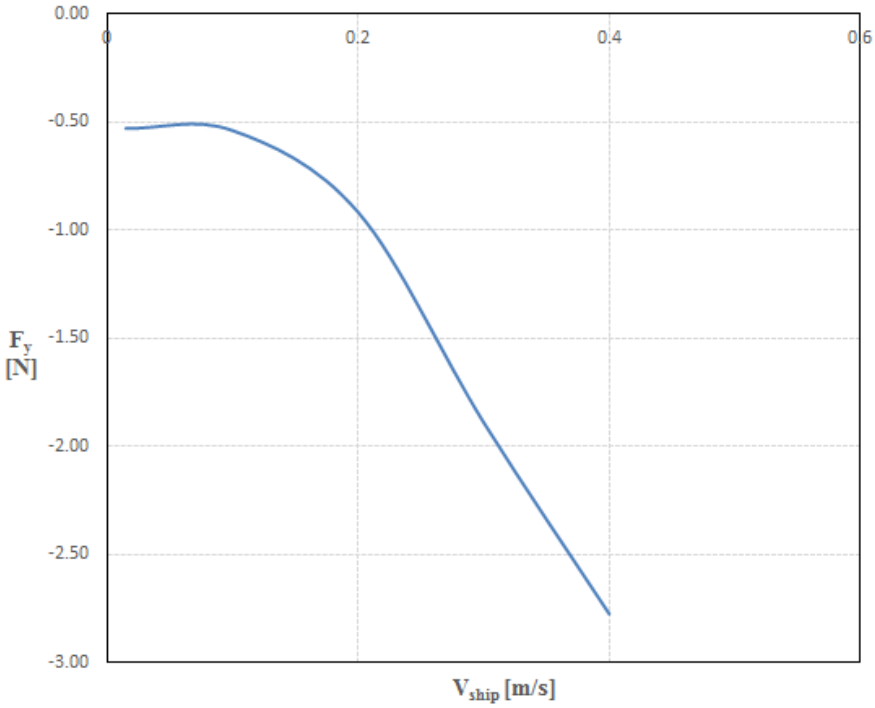

Figure 3.10 Transverse force F_y vs forward speed for T = 1.78 N

The variation of the transverse force F_y with forward speed of the wedge is shown in Figure 3.10. There is a steady increase in magnitude in F_y as the forward speed V_{ship} increases. As mentioned in section 3.1.1, the computed transverse force F_y must be positive to indicate thrust deduction. The negative sign implies that F_y is in the direction of thrust, indicating a net gain in thrust. This gain in thrust increases as forward speed increases. The distribution of pressure over the hull, for each forward speed, can be considered in an attempt to explain this observation.

A jet in the near-absence of cross-flow is seen in Figure 3.11(a) wherein it suffers a minor deflection towards the hull. As CFX did not provide sufficiently converged results for an inlet velocity of 0, therefore a small value (V_{ship} = 0.015 m/s) was used as the boundary condition. The corresponding pressure contours in Figure 3.11(b) and (c) show a uniform pressure over the hull except around the tunnel ends where the high velocities at the entry and exit lead to lower pressures. It is seen that F_y is negative implying a gain in thrust which is contrary to experimental observation[6]. From Table 3.5, it is observed that F_y is positive for the wedge, bow and stern parts, and it is the contribution on the tunnel ends that makes the net F_y on the hull in the direction of the thrust. This means that the largest contribution to the total force comes from the acceleration of the flow at the inlet of the tunnel.

At the slightly higher forward speed V_{ship} = 0.1 m/s, as in Figure 3.12, the flow field is only slightly different from the lowest speed case. The pressure is uniform over the hull, except in the vicinity of the tunnel ends where the in- and outflow cause a lower pressure due to high

velocities. Based on Table 3.6, as in the previous case, the contribution from tunnel ends results in a net gain of thrust. The acceleration at the inlet side creates a larger force than the bending of the jet does at the outlet side of the tunnel.

At V_{ship} = 0.2 m/s, the deflection of the jet is more significantly visible (Figure 3.13(a)) in the flow field. From the pressure distributions in Figure 3.13(b) and (c), the pressure is largely uniform over the hull though areas of low pressure are seen to develop in the wedge part, around the tunnel ends. This is particularly significant on the outlet side. This results in the net transverse force contribution on the wedge part to decrease in magnitude. This is further confirmed in Table 3.7 which shows that the forces on bow and stern have been increasing while the contribution on the wedge part has reduced to a small value in the direction opposing thrust. For V_{ship} = 0.3 m/s and V_{ship} = 0.4 m/s, it is observed from Figure 3.14 and Figure 3.15 that the jet is significantly bent towards the hull. The contours show redistribution of pressure on the hull. As the forward speed increases, the forces on bow and stern also increase in magnitude while the net force on the wedge part decreases until it becomes negative – i.e. in the direction of thrust – at V_{ship} higher than 0.2 m/s. The forces on bow and stern increase in magnitude, while always directed in the direction of the thrust, such that by V_{ship} = 0.3 m/s the combination of these components decide the magnitude and direction of the net F_y. The force on tunnel ends does not vary significantly with forward speed. The transverse force on the tunnel, which is shearing in nature, remains positive and increases with forward speed.

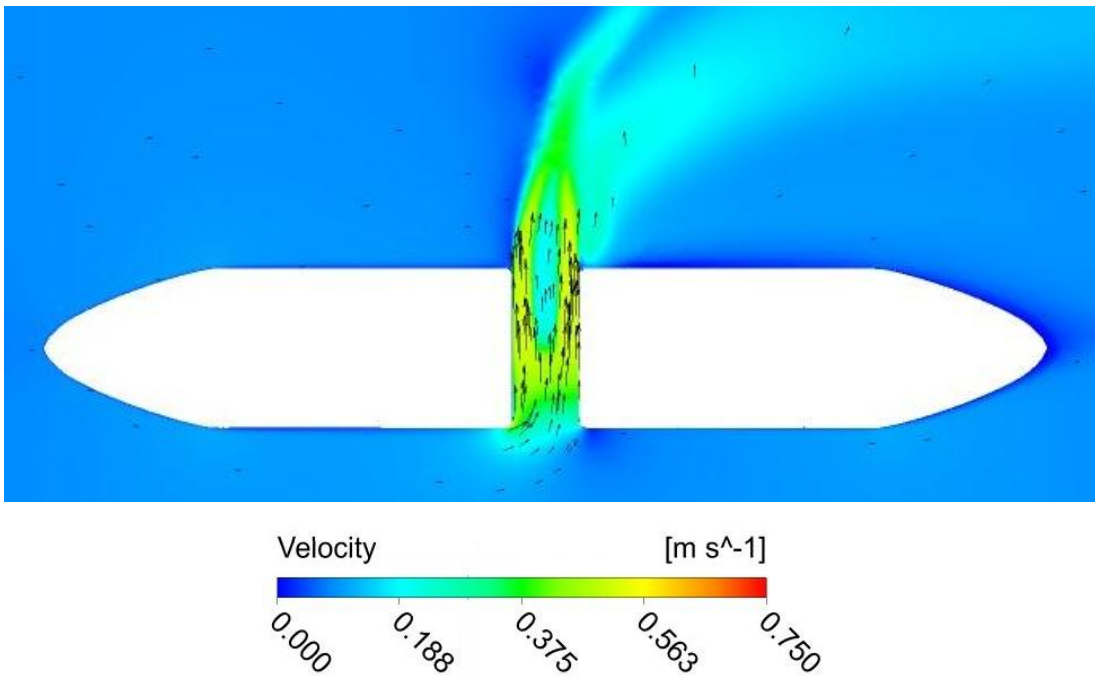

(a) Velocity magnitude distribution

(b) Hydrodynamic pressure. The inlet side(Port)

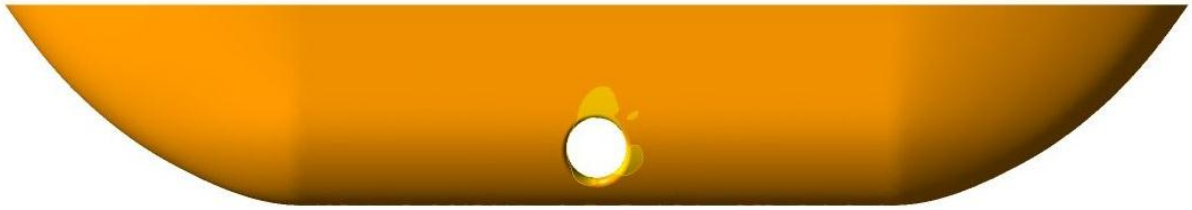

(c) Hydrodynamic pressure. The outlet side (Starboard)

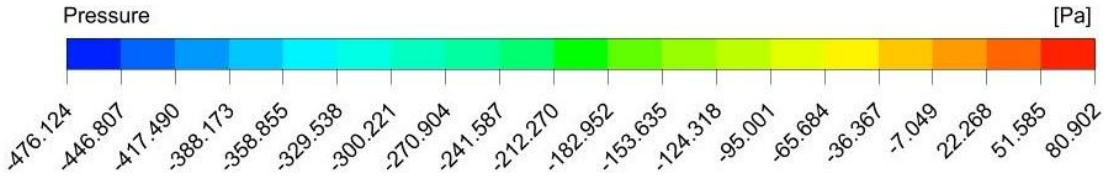

Figure 3.11 V_{ship} = 0.015 m/s, T = 1.78 N

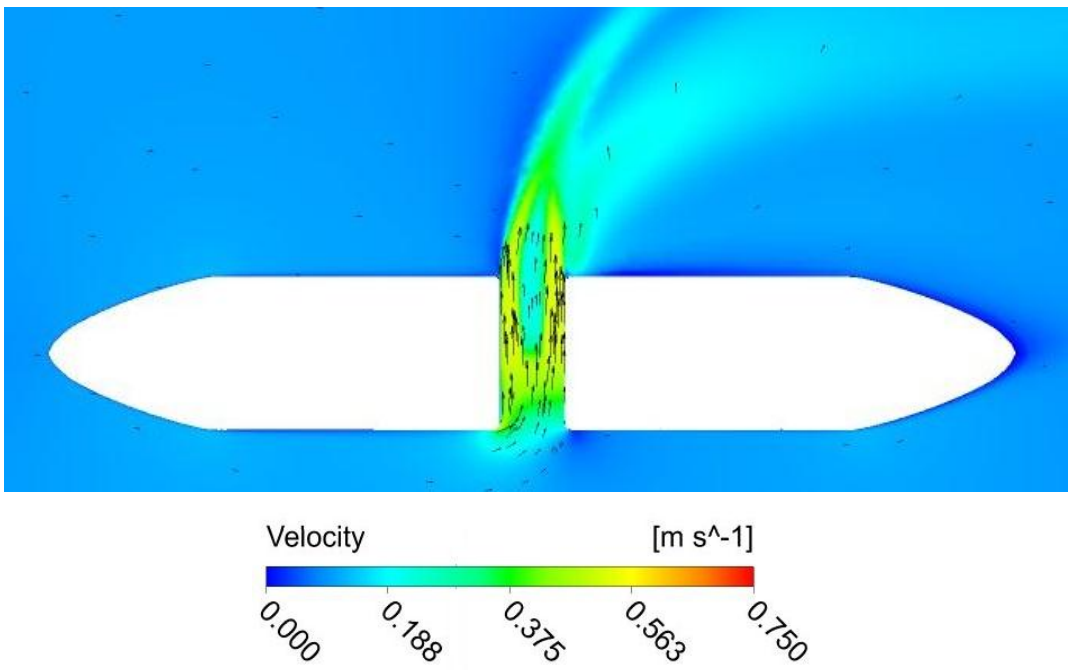

(a) Velocity magnitude distribution

(b) Hydrodynamic pressure. The inlet side(Port)

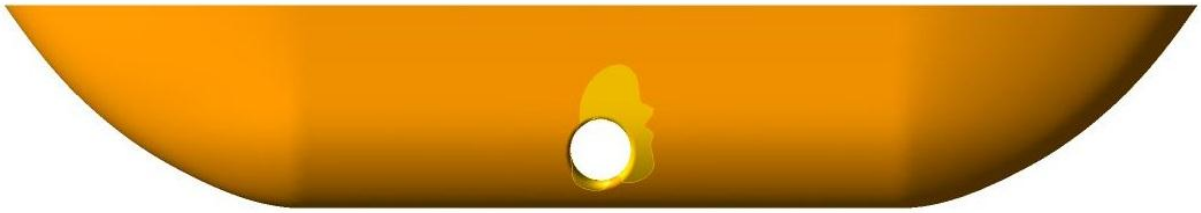

(c) Hydrodynamic pressure. The outlet side (Starboard)

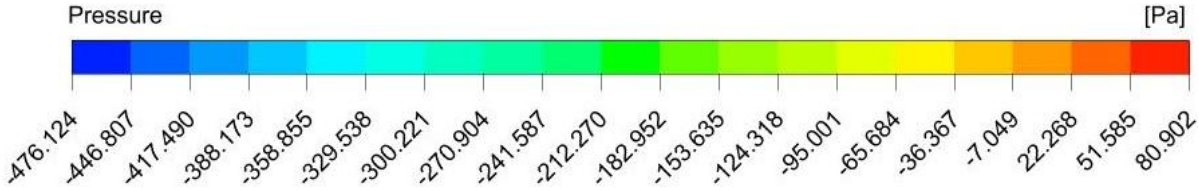

Figure 3.12 V_{ship} = 0.1 m/s, T = 1.78 N

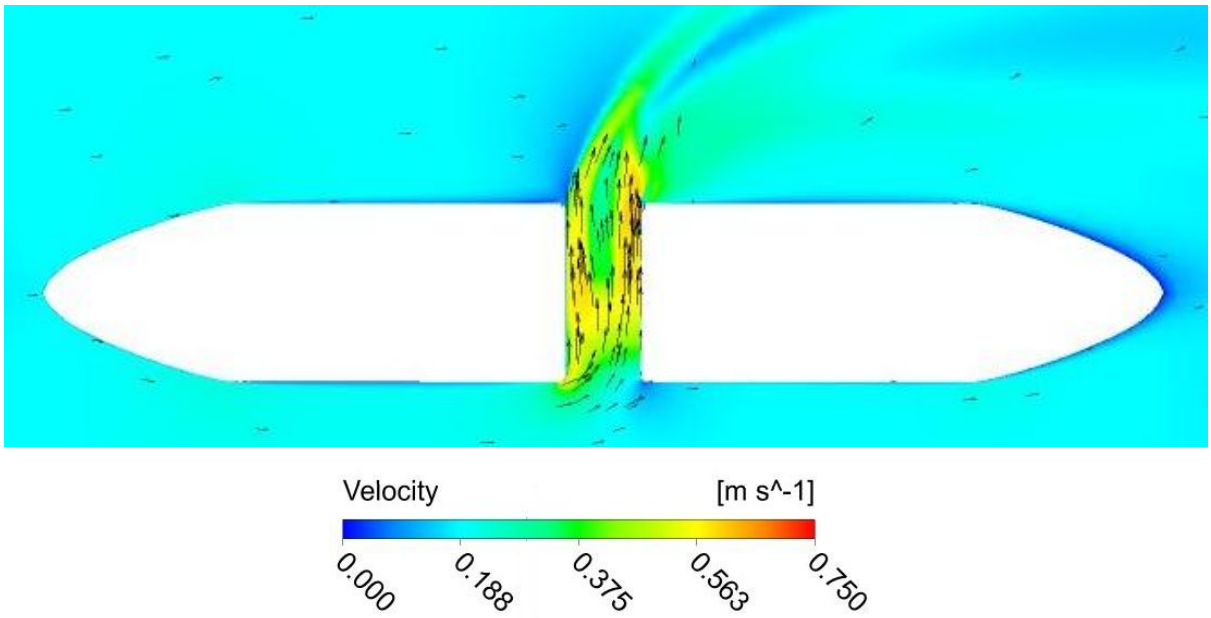

(a) Velocity magnitude distribution

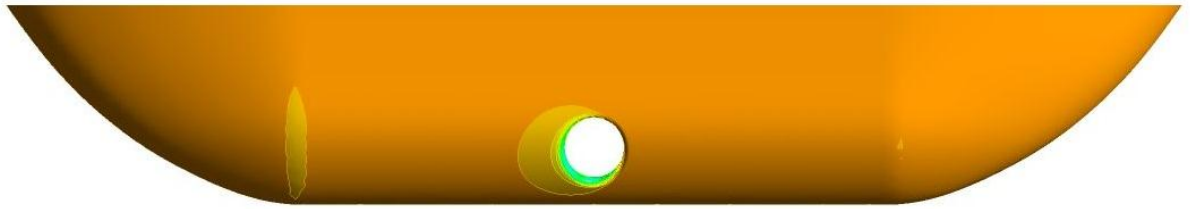

(b) Hydrodynamic pressure. The inlet side(Port)

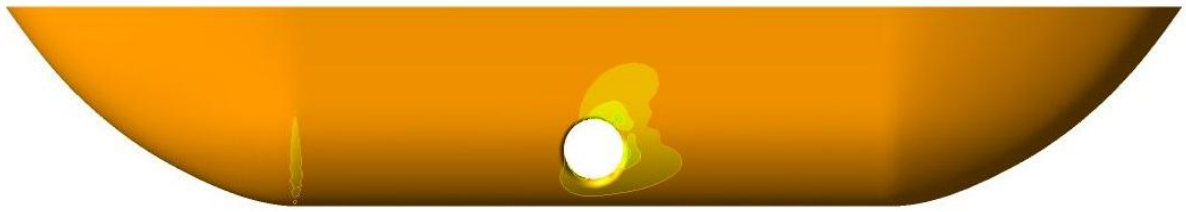

(c) Hydrodynamic pressure. The outlet side (Starboard)

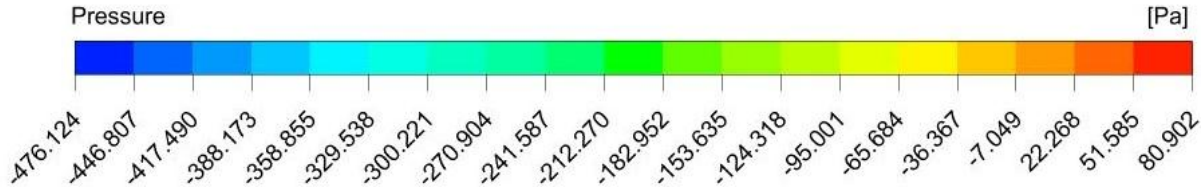

Figure 3.13 V_{ship} = 0.2 m/s, T = 1.78 N

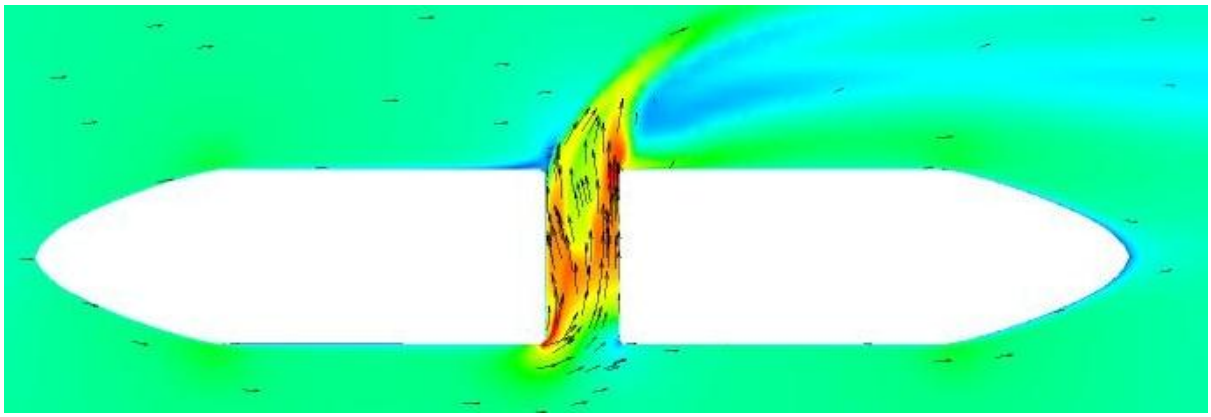

(a) Velocity magnitude distribution

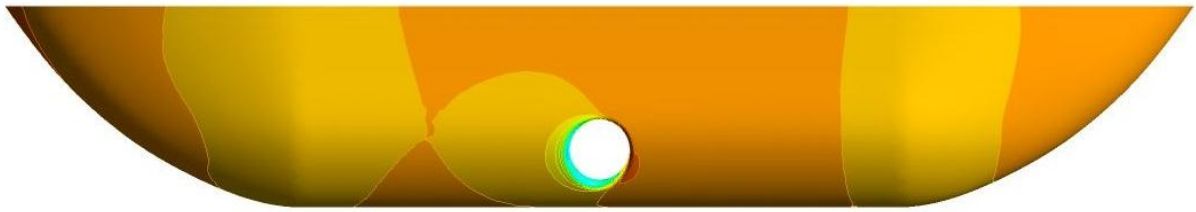

(b) Hydrodynamic pressure. The inlet side(Port)

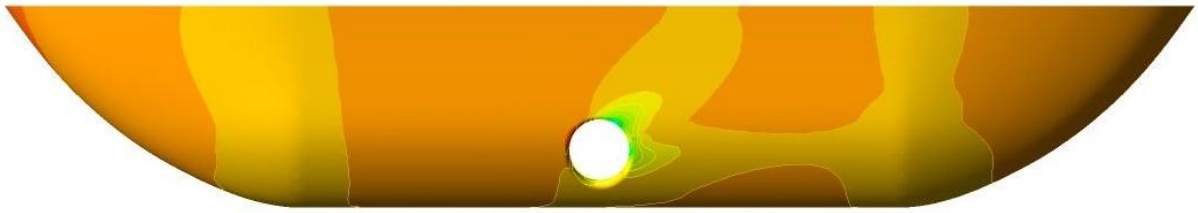

(c) Hydrodynamic pressure. The outlet side (Starboard)

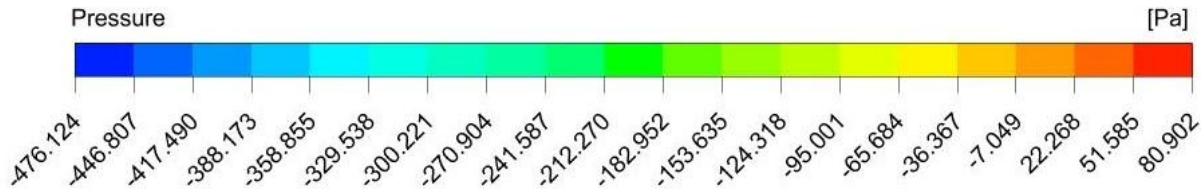

Figure 3.14 V_{ship} = 0.3 m/s, T = 1.78 N

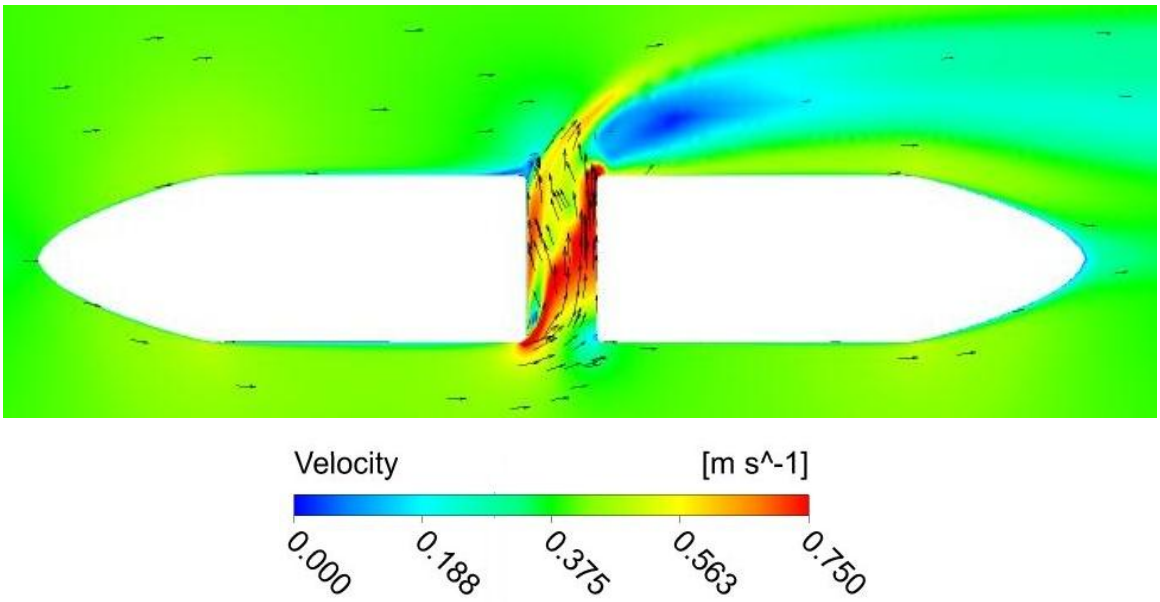

(a) Velocity magnitude distribution

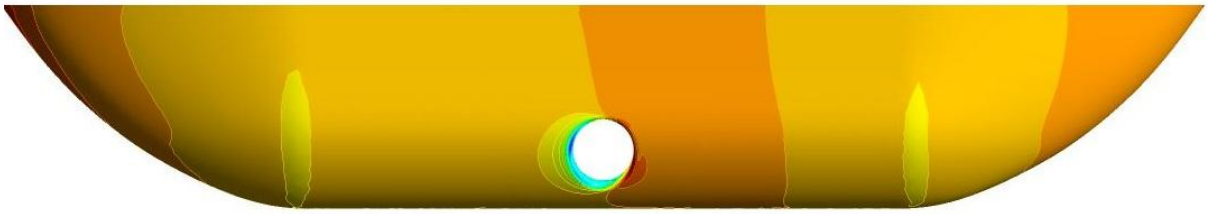

(b) Hydrodynamic pressure. The inlet side(Port)

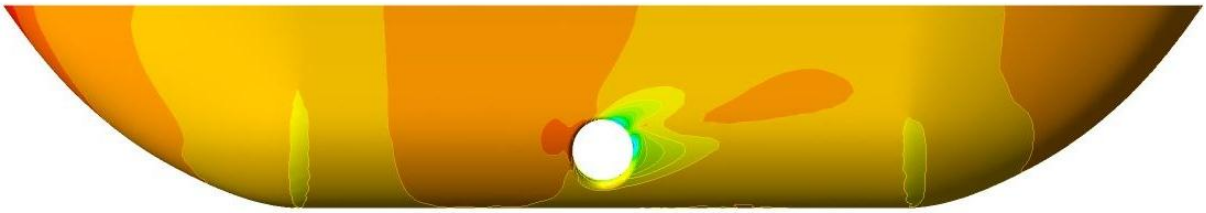

(c) Hydrodynamic pressure. The outlet side (Starboard)

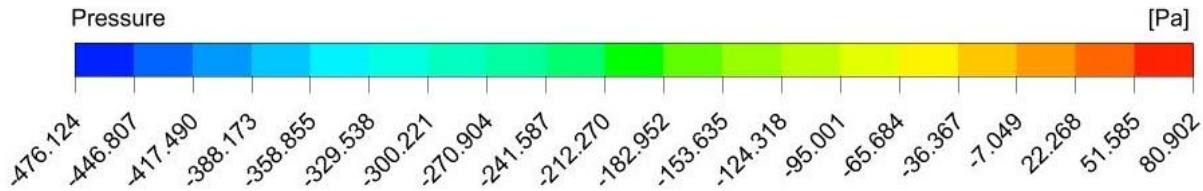

Figure 3.15 V_{ship} = 0.4 m/s, T = 1.78 N

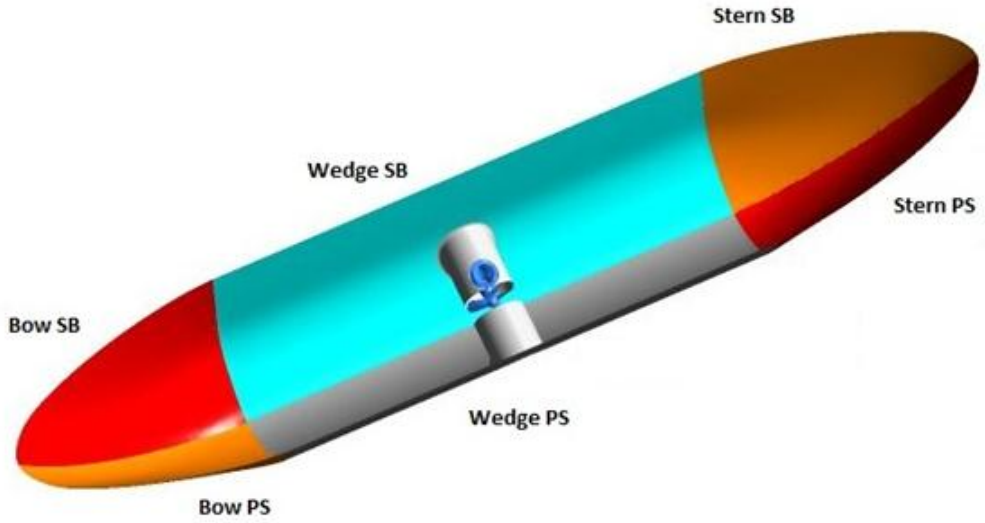

Figure 3.16 Parts of the hull to observe different components of transverse force

	Bow [N]	Wedge [N]	Stern [N]	Tunnel end [N]	Tunnel [N]	
Port side	0.326	0.481	0.203	-0.786	0.028	
Starboard	-0.392	-0.262	-0.252	0.070	0.041	
Total [N]	-0.066	0.218	-0.048	-0.716	0.069	: -0.543

Table 3.5 Forces for V_{ship} = 0.0015 m/s, T = 1.78 N

	Bow [N]	Wedge [N]	Stern [N]	Tunnel end [N]	Tunnel [N]	
Port side	-0.217	-0.826	-0.127	-0.815	0.028	
Starboard	0.133	1.055	0.072	0.102	0.042	
Total	-0.084	0.229	-0.055	-0.713	0.070	: -0.553

Table 3.6 Forces for V_{ship} = 0.1 m/s, T = 1.78 N

	Bow [N]	Wedge [N]	Stern [N]	Tunnel end [N]	Tunnel [N]	
Port side	-0.291	-0.528	0.187	-0.942	0.034	
Starboard	0.116	0.601	-0.386	0.227	0.050	
Total	-0.175	0.073	-0.200	-0.715	0.085	: -0.933

Table 3.7 Forces for V_{ship} = 0.2 m/s, T = 1.78 N

	Bow [N]	Wedge [N]	Stern [N]	Tunnel end [N]	Tunnel [N]	
Port side	-1.777	-5.188	-1.657	-1.190	0.043	
Starboard	1.397	4.979	0.957	0.462	0.064	
Total	-0.380	-0.209	-0.700	-0.728	0.107	: -1.909

Table 3.8 Forces for V_{ship} = 0.3 m/s, T = 1.78 N

	Bow [N]	Wedge [N]	Stern [N]	Tunnel end [N]	Tunnel [N]	
Port side	-3.157	-8.963	-3.080	-1.310	0.050	
Starboard	2.631	8.511	1.783	0.663	0.074	
Total [N]	-0.526	-0.452	-1.297	-0.646	0.124	: -2.797

Table 3.9 Forces for V_{ship} = 0.4 m/s, T = 1.78 N

Comparison with Karlikov and Sholomovich

The authors in [12] observed that the performance of bow thrusters is hampered by the strong dependence of their effectiveness on the ship's speed. There is an initial decrease in lateral forces on the ship, and the effectiveness is eventually restored as the speed increases. The behavior observed in [12] is given in Figure 3.17. In this figure, the coefficient

$$C = \frac{C_y}{C_{y,0}} \tag{3.4}$$

where the lateral force coefficient C_y is defined as

$$C_y = \frac{2F_y}{\rho {V_{jet}}^2 A_{tunnel}} \tag{3.5}$$

where F_y is the lateral force on the ship, V_{jet} the tunnel jet speed and A_{tunnel} the area of the tunnel. $C_{y,0}$ is the force coefficient at zero forward speed, and the parameter m is the ratio of the ship speed and the velocity of the jet given by

$$m = \frac{V_{ship}}{V_{jet}} \tag{3.6}$$

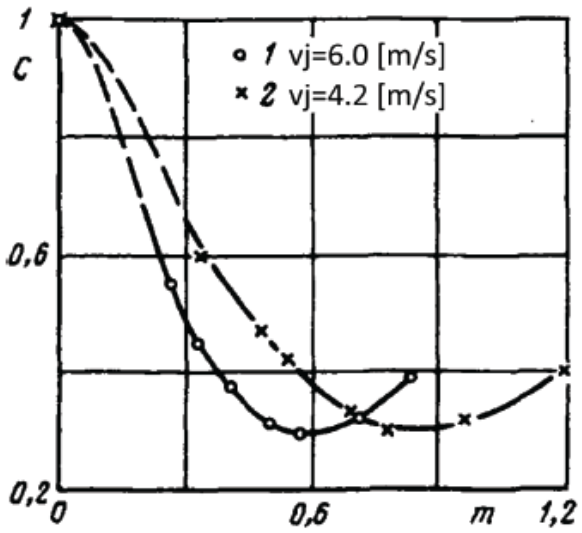

Figure 3.17 *C*-*m* plot from Karlikov and Sholomovich

The results of the simulations is as shown in Figure 3.18. The CFD results obtained differ vastly from the results in literature in terms of magnitude and behaviour of *C*. In place of a drop in value of *C*, a monotonous increase is observed in the computed results and thrust deduction is not observed. However, it must be noted that the hull used by Karlikov and Sholomovich [12] is different from the Nienhuis wedge, and the behaviours in Figure 3.17 and Figure 3.18 need not necessarily agree.

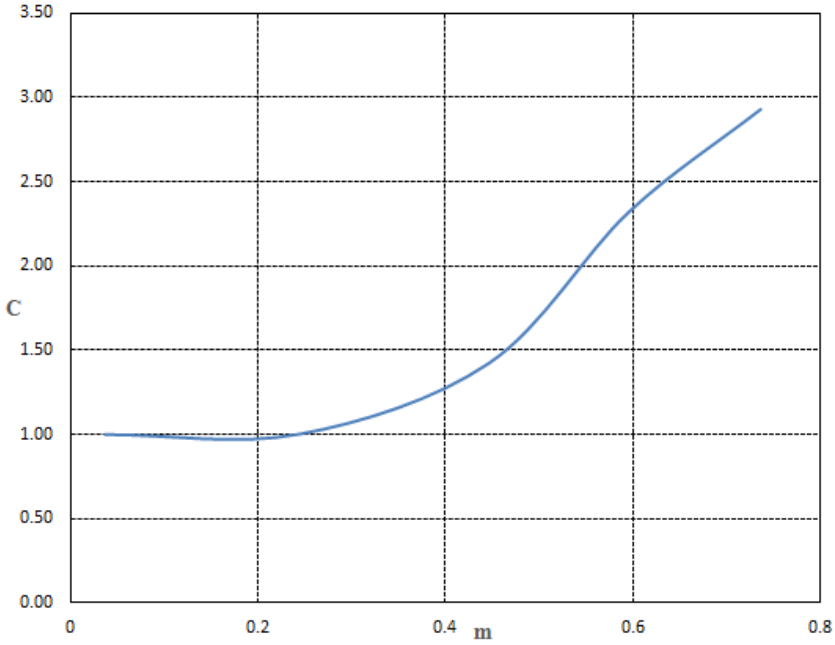

Figure 3.18 *C-m* plot for T = 1.78 N

Further, experiments [6] indicate that the performance, in case of the hopper, initially decreases with forward speed before increasing again. It is concluded that a Nienhuis wedge, with a tunnel thruster approximated by an actuator disk for thrust T = 1.78 N, shows a different behaviour. The Nienhuis wedge behaves as a slender body in the flow, with redistributed pressure over the hull (including the bow and stern) due to the inflow interacting with the jet from the tunnel. As a result, the wedge experiences a transverse force which manifests as an increase in the net F_y, and hence in the coefficient C.

Thrust T = 10 N

The thrust by the actuator disk is set at 10 N and simulations are performed for a range of forward speeds as in the preceding case. Figure 3.19 shows the distributions of velocity magnitude and hydrodynamic pressure on the hull for the ship speed 0.4 m/s. As in the previous case with thrust T = 1.78 N, the performance of the thruster does not decrease, and, instead, an increase is obtained with increasing forward ship speed. Table 3.10 – 3.13 show the forces on the different parts of the hull for T = 10 N for various forward speed conditions.

	Bow [N]	Wedge [N]	Stern [N]	Tunnel end [N]	Tunnel [N]		
Port side	-0.351	-3.270	-0.220	-4.580	-0.006		
Starboard	0.044	3.710	0.130	0.220	0.000		
Total [N]	-0.307	0.440	-0.090	-4.360	-0.006	:	-4.323

Table 3.10 Forces for V_{ship} = 0.1 m/s, T = 10 N

	Bow [N]	Wedge [N]	Stern [N]	Tunnel end [N]	Tunnel [N]		
Port side	0.124	-1.200	0.099	-4.640	-0.006		
Starboard	-0.268	2.510	-0.002	0.220	0.000		
Total [N]	-0.144	1.310	0.097	-4.420	-0.006	:	-3.163

Table 3.11 Forces for *Vship* = 0.2 m/s, T = 10 N

	Bow [N]	Wedge [N]	Stern [N]	Tunnel end [N]	Tunnel [N]		
Port side	1.680	2.690	1.090	-4.490	-0.006		
Starboard	-1.820	-2.520	-1.010	0.190	0.000		
Total [N]	-0.140	0.170	0.080	-4.300	-0.006	:	-4.196

Table 3.12 Forces for V_{ship} = 0.3 m/s, T = 10 N

	Bow [N]	Wedge [N]	Stern [N]	Tunnel end [N]	Tunnel [N]		
Port side	4.230	8.850	2.700	-4.450	-0.006		
Starboard	-4.430	-8.840	-2.640	0.150	0.000		
Total [N]	-0.200	0.010	0.060	-4.300	-0.006	:	-4.436

Table 3.13 Forces for V_{ship} = 0.4 m/s, T = 10 N

In Figure 3.19(a), it is seen that the jet is only minimally influenced by the cross-flow even for a high forward speed of 0.4 m/s. This implies a uniform pressure distribution over the hull, with variations around the inlet and outlet, as seen in Figure 3.19(b) and (c). Similar to the case explained in Figure 3.11 (T = 1.78 N, minimum speed case), the contribution on the tunnel ends result in a force F_y that is negative implying a gain in thrust.

It is seen from Table 3.10 – 3.13 that the force at tunnel ends contribute the most towards the net negative F_y for all speeds considered. The magnitude of the forces at tunnel ends are also similar in the four cases, resulting in little variation in the net transverse force. It is seen the forces at the bow, wedge and stern regions vary with the forward speed. However, the magnitude of force contributions by these areas are much smaller compared to the force resulting from the acceleration of the flow at tunnel inlet.

This study further reinforces the previously obtained conclusion that numerical simulations on Nienhuis wedge does not agree with the experimental observations [6] indicating a decrease

in performance of the thruster. Further numerical studies with the Nienhuis wedge may be performed with a full thruster unit with hub and strut, instead of the actuator disk approach.

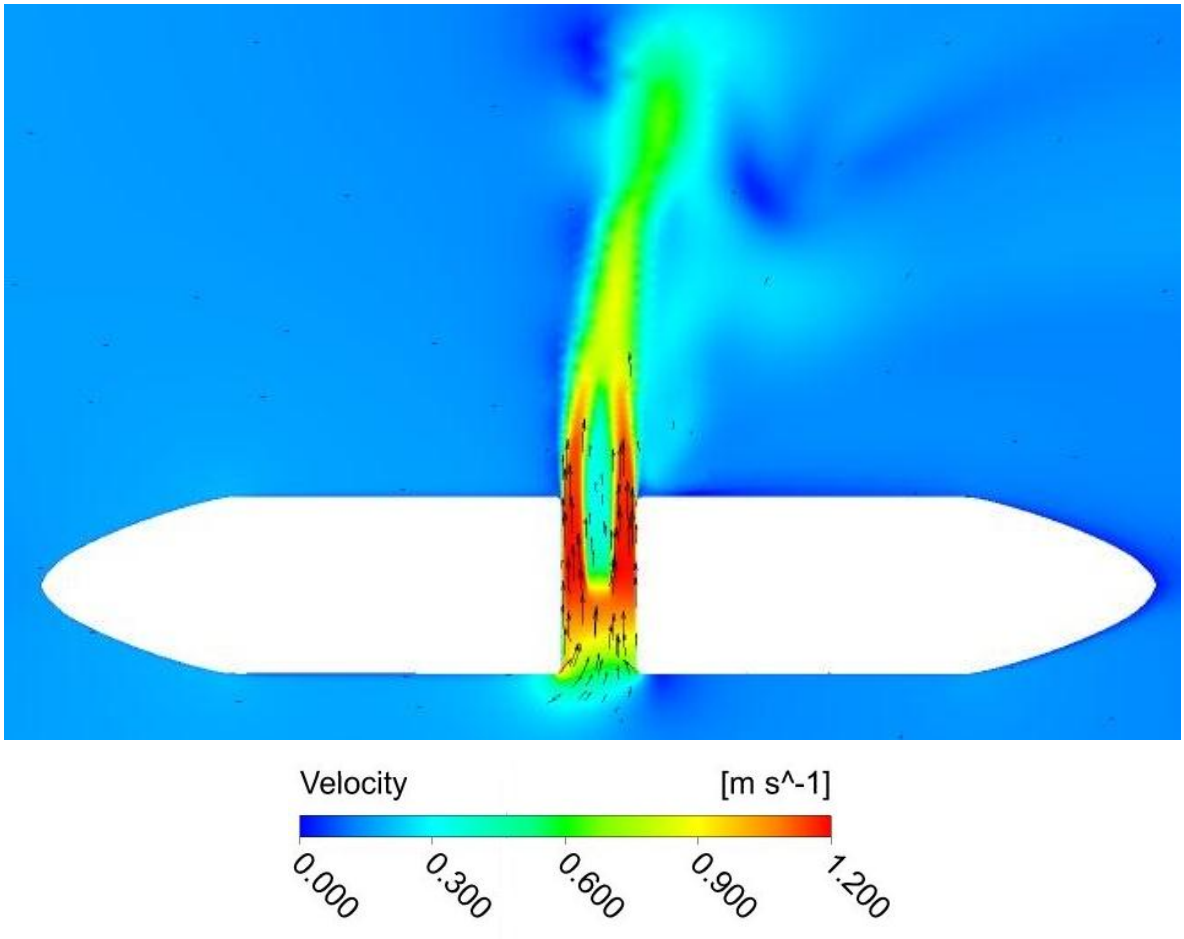

(a) Velocity magnitude distribution

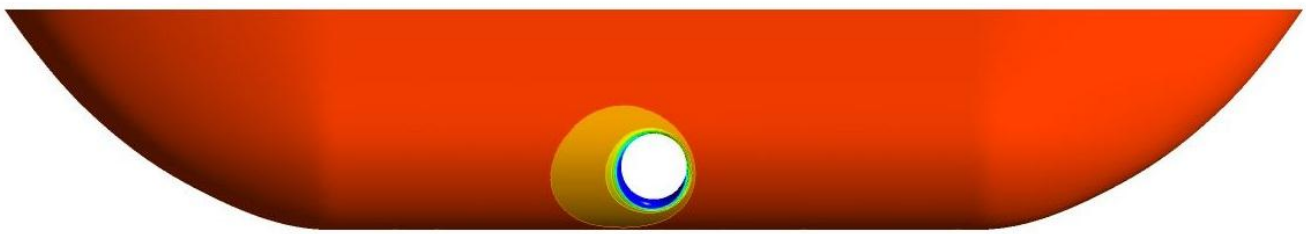

(b) Hydrodynamic pressure. The inlet side (Port)

(c) Hydrodynamic pressure. The outlet side (Starboard)

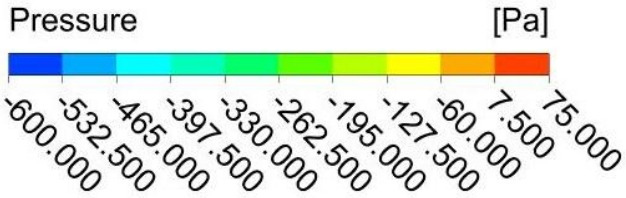

Figure 3.19 V_{ship} = 0.4 m/s, T = 10 N

3.3 Isolated Thruster in a tunnel

In order to investigate the influence of the use of an actuator disk to model the thrust on the numerical results, the actuator disk is replaced by a full thruster unit in the tunnel. This thruster unit is shown in Figure 3.20, consisting of the propeller blades, a hub and a strut.

In order to deliver the same thrust as that used in the actuator disk, the thruster unit's propeller characteristics must be determined. For this purpose, the thruster unit is placed inside an isolated tunnel as shown in Figure 3.21 and a numerical simulation is carried out for a given propeller rotation speed. Then, from similarity the propeller rotation speed for the desired thrust can be calculated.

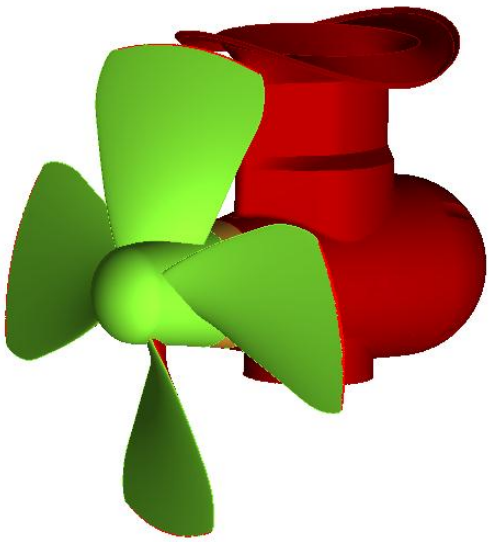

Figure 3.20 The thruster unit

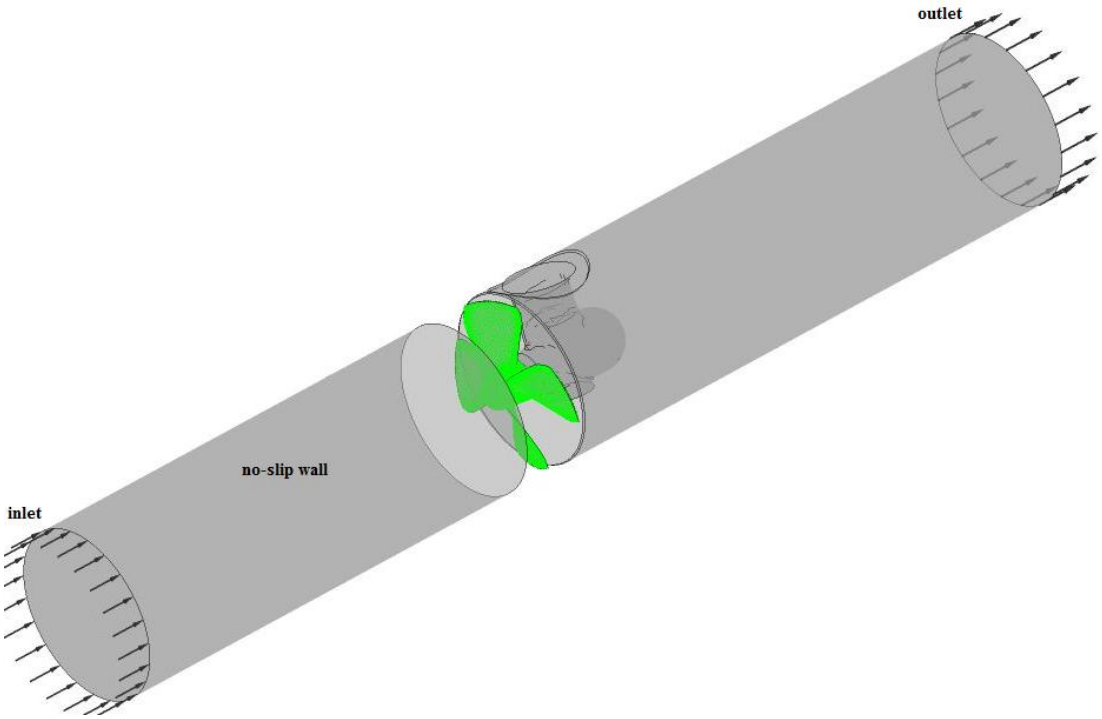

Figure 3.21 Isolated thruster in a tunnel: Computational domain

3.3.1 Computational model

Numerical Formulation

To simulate the rotating propeller of the thruster unit the frozen rotor approach is employed. In this approach, the propeller is fixed in a given position with respect to the hub and strut, while the rotation effects are accounted for by including source terms in the Navier-Stokes equations, viz. the centrifugal and Coriolis forces. Note that doing so, the frozen rotor model does not resolve the unsteadiness of the wakes in time resulting from the propeller blades passing the hub and strut, however, the results resemble a snapshot in time of the actual flow corresponding to the chosen propeller blade position.

Computational Domain

The thruster unit is simulated in the center of an isolated tunnel as shown in Figure 3.21. The rotating part of domain containing the propeller blades is highlighted in this figure. This rotating part of the domain is connected to the remaining stationary domain at the interfaces as indicated in Figure 3.22 using the General Grid Interface (GGI) technique which is a method for connecting non-conformal and conformal mesh regions.

At the solid walls, that is the thruster unit and the tunnel walls, a no-slip conditions is applied. It can be argued that a tunnel thruster unit on a vessel operates in bollard-pull condition, as the unit is directed perpendicular to the main forward speed of the vessel. Therefore, at the inlet and outlet boundaries of the tunnel, a constant pressure boundary condition is applied, as opposed to the use of a boundary condition prescribing a given velocity. The computational grid on the thruster unit surface is shown in Figure 3.23.

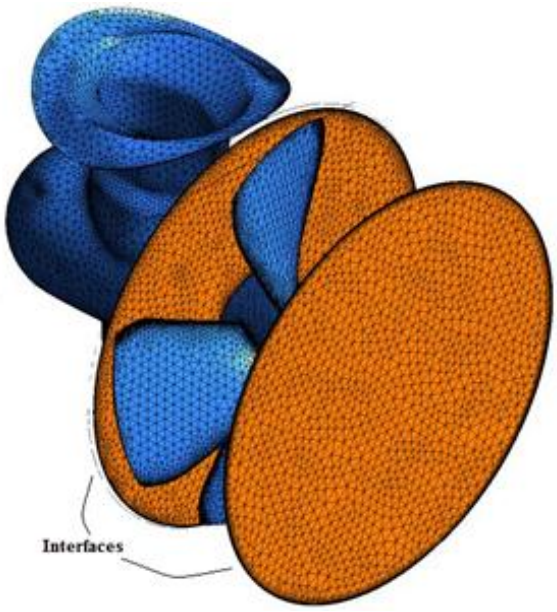

Figure 3.22 Interfaces between rotating and stationary domains

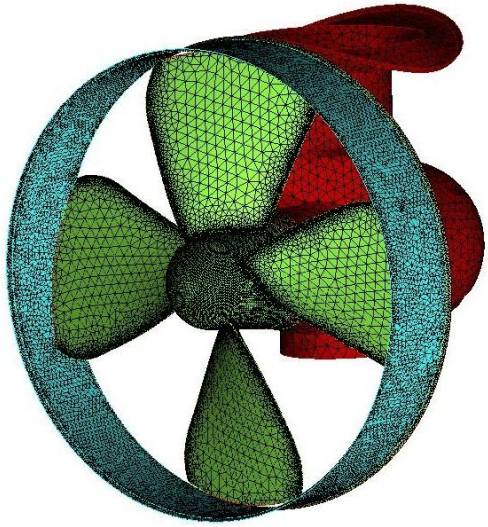

Figure 3.23 Grid on the propeller

3.3.2 Computational results

In order to verify similarity, simulations are performed for two propeller rotation speeds, n = 504 rpm and n = 762 rpm. The resulting calculated thrust for both rotation speeds are given in Table 3.14.

n [rpm]	T [N]
504	4.78
762	10.95

Table 3.14 Values of rpm and thrust for thruster unit in a tunnel

Now, similarity can be checked by considering the thrust coefficient K_T, defined as:

$$K_T = \frac{T}{\rho n^2 D^4} \tag{3.7}$$

where T [N] is the total thrust of the unit, ρ [kg/m^3] is the fluid density and D [m] the propeller blades diameter. From similarity (K_T = constant) it follows that from a given thrust and corresponding rotation speed (T_1, n_1), desired conditions (T_2, n_2) can be calculated from

$$\frac{T_1}{{n_1}^2} = \frac{T_2}{{n_2}^2} \tag{3.8}$$

From the numerical results it follows that

$$\frac{T_1}{{n_1}^2} \Big/ \frac{T_2}{{n_2}^2} = 0.998$$

which confirms that similarity applies in the numerical results.

In Figure 3.24, the calculated flow field for n = 504 rpm is shown in a cross section through the center of the tunnel. Note that the velocity magnitude is increased behind the thruster unit at the outer diameters of the tunnel, while a wake is formed behind the hub in the center of the tunnel.

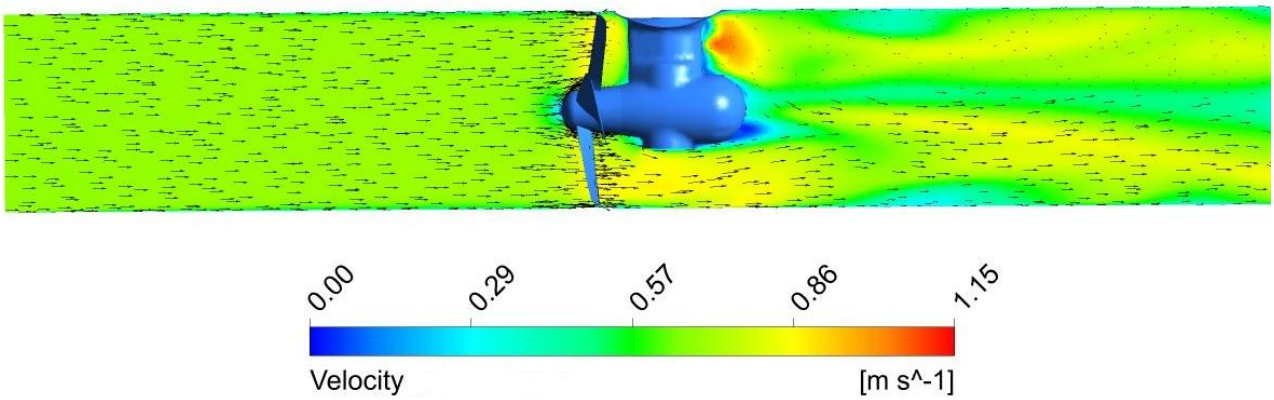

Figure 3.24 Flow field for n = 504 rpm

3.4 Nienhuis wedge with a thruster unit

In order to investigate the influence of the actuator disk approach as employed previously, the tunnel thruster is now investigated by using a full thruster unit, using the rotation speed as calculated in the previous section.

Computational Domain

For consistency with the actuator disk simulations, the center plane of the thruster unit's propeller blades is positioned in the center of the tunnel, see Figure 3.25.

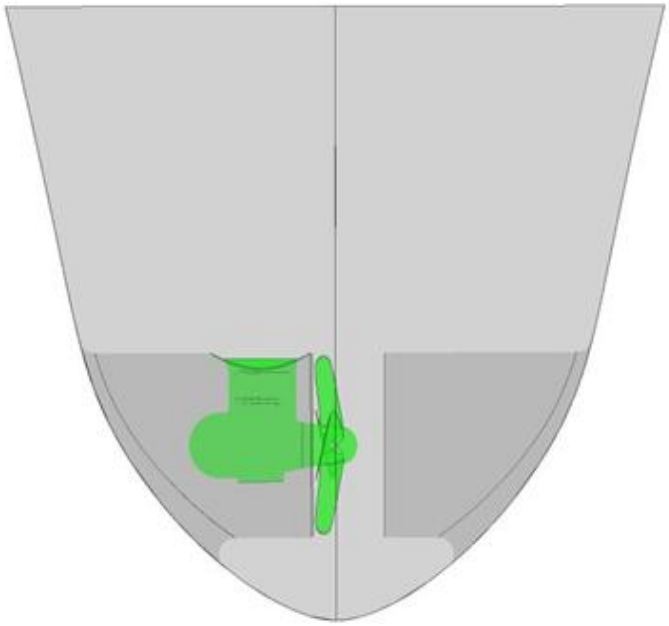

Figure 3.25 The thruster in the bow tunnel

The computational domain and settings remain the same as described in previous sections. Similarly as in the previous simulations, Mesh 2 is chosen as an optimal grid for future simulations following the grid convergence study described in section 3.1.2. The grid containing the thruster unit is similar to that given in section 3.3.1.

3.4.1 Thruster unit with 307 rpm

A rotation speed of n = 307 rpm corresponds to a thrust of T = 1.78 N, based on the similarity as described in section 3.3.1. Simulations are performed for a range of forward speeds for this rotational speed and the efficiency of the thruster is investigated.

Comparison with Karlikov and Sholomovich

The CFD results obtained differ from the results in literature in terms of magnitude of variation in the coefficient C (explained in section 3.2.1) although there is resemblance in the behaviour. In case of the obtained results, there is a slight 'gain' in thrust for lower values of m before the decrease. The distribution of forces on the hull can be investigated for a value of m that shows an increase in C above 1 as well as one for which $C < 1$ and an attempt for an explanation is made. The hull can be divided into different parts for convenience of analysis as in Figure 3.16, and the force on each part may be computed. The results for 307 rpm, as shown in Figure 3.26 show a deduction in thrust for the value of parameter m = 0.485 or V_{ship} = 0.2 m/s.

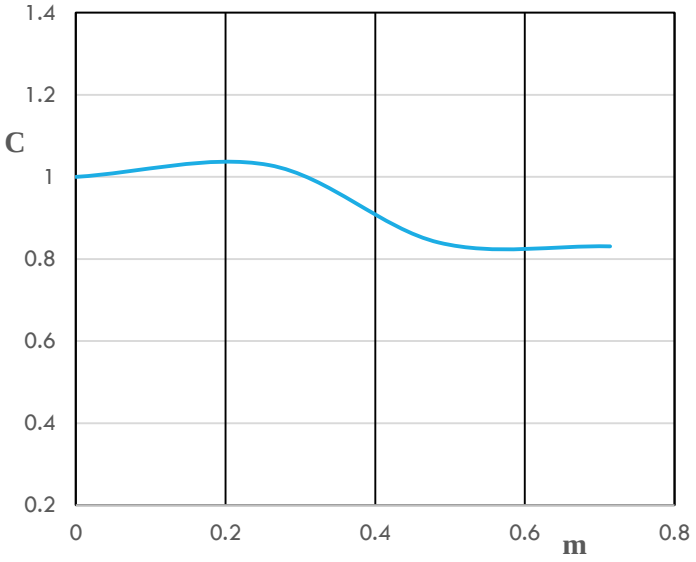

Figure 3.26 *C-m* plots for 307 rpm

The thrust of the thruster unit can also be calculated by integrating the pressure and shear stress on the thruster. It is found that the computed thrust is not just much higher than the assumed value of 1.78 N, it also varies with forward speed. These observations may be attributed to the thruster-hull interaction and the change in inflow to the thruster with forward speed. The thrusts and the corresponding speeds are as tabulated in Table 3.15.

V_{ship} [m/s]	Computed thrust [N]
0.01	3.03
0.1	3.16
0.2	2.69
0.3	2.58
0.4	3.96

Table 3.15 Thrusts computed for 307 rpm and the corresponding forward speeds

It is concluded that the relation based on similarity as obtained in section 3.3.1 does not hold for a thruster in a tunnel with the vessel having a forward speed. Hence, obtaining the desired thrust for a given forward speed requires some trial and error with the propeller rotation speed. It is seen that an approximately steady thrust of 10 N can be obtained by varying the rotation speed between 488 and 500 rpm. Results obtained using these rotation speeds can be compared to the actuator disk cases with 10 N thrust. Further, C-m plots can be obtained for both the actuator disk approach and the thruster unit, for the delivered thrust of 10 N, and compared.

3.4.2 Thruster unit vs Actuator disk with delivered thrust of 10 N

The velocity distribution for the thruster unit for 488 rpm with forward speed 0.4 m/s is shown in Figure 3.27. The computed thrust for this rotation speed is 9.3 N. The velocity distribution for the actuator disk approach for the same forward speed is given in Figure 3.28.

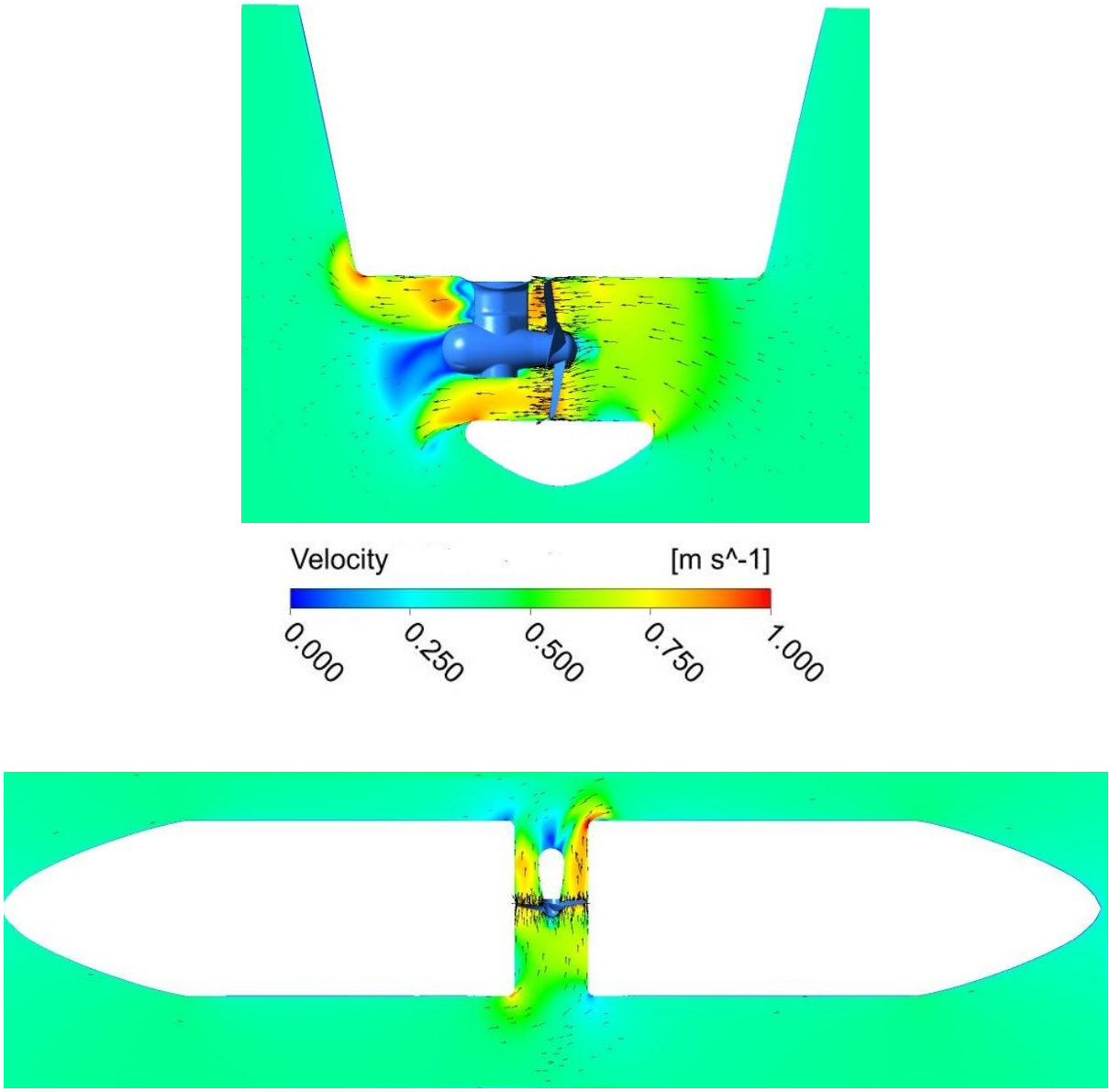

Figure 3.27 Velocity magnitude distribution, 488 rpm, V_{ship} = 0.4 m/s

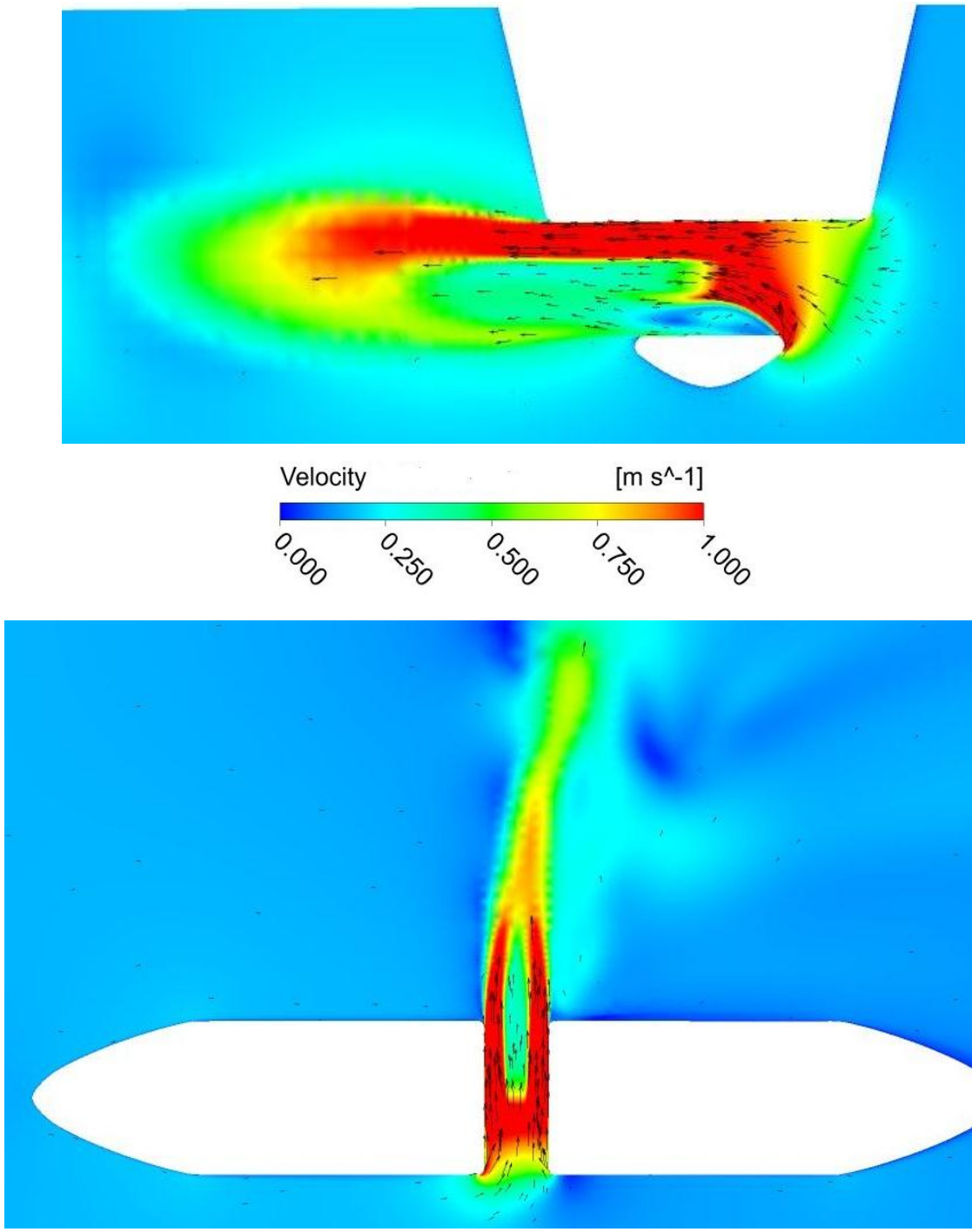

Figure 3.28 Velocity magnitude distribution for actuator disk, T = 10 N, V_{ship} = 0.4 m/s

A stronger jet is seen in the actuator disk case compared to the one with the thruster unit although both cases have similar delivered thrusts.

The *C-m* plots for both cases can be plotted and compared, as shown in Figure 3.29. It is seen from Figure 3.29 that for the thruster unit case, higher values of *m* show a deduction in thrust, while the actuator disk approach indicate a gain in thrust for the whole range of *m*.

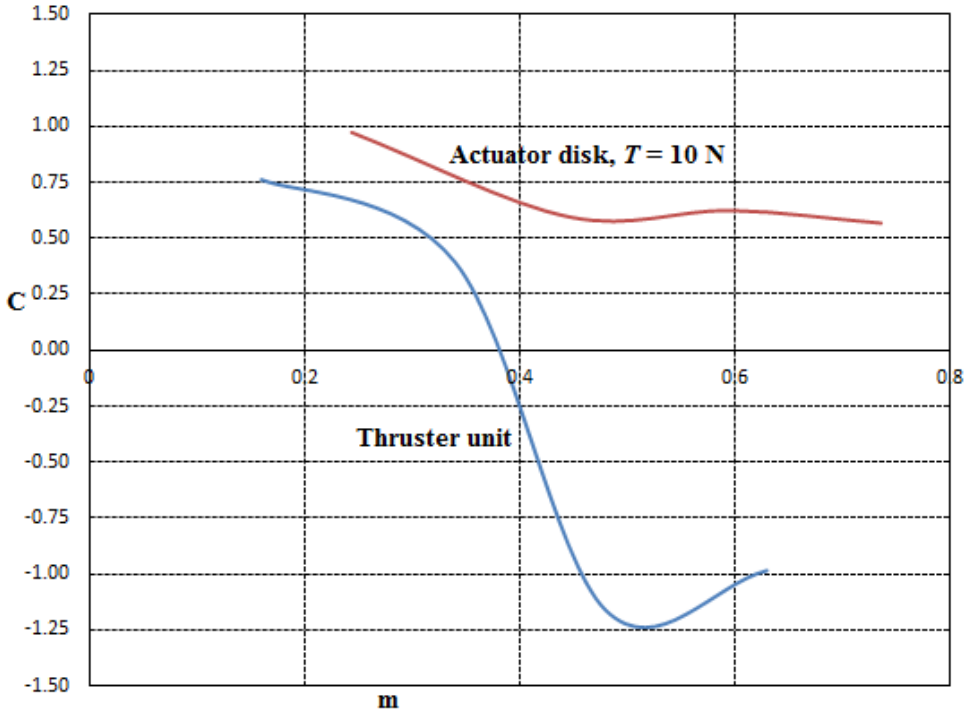

Figure 3.29 *C*-*m* plots for actuator disk and thruster unit cases for delivered thrust = 10 N

Higher values of *m* imply weaker jets. Hence, for weaker jets, the thruster unit shows a deduction in thrust. On the contrary, the value of the coefficient *C* does not vary much with *m* in case of the actuator disk approach. The rotation imparted by the thruster and the wake region that forms behind the hub of the thruster unit results in a significantly different flow field.

3.4.3 Comparison with experimental values

The test results from Nienhuis[1] are used for quantitative comparison with the numerical results. Nienhuis has provided a plot of thrust deduction factor C_F against transverse speed of the hull from model tests. Since the current work deals with the hull having forward speeds, the provided values of C_F at zero speed can be used to make a quantitative comparison. Based on Schaap[2], the thrust deduction factor C_F is defined for the actuator disk approach as:

$$C_F = \frac{F_y}{T} \tag{3.9}$$

where F_y is the transverse force on the hull with the actuator disk delivering thrust T. In case of simulations with a thruster unit, C_F is given by Schaap[2] as:

$$C_F = \frac{T - F_y}{T} \tag{3.10}$$

where T is the computed thrust delivered by the thruster and F_y is the transverse force on the hull.

While comparing the values quantitatively, it is to be noted that the geometry of the thruster unit used by Nienhuis is different from the one used in the current work. Nienhuis has provided

the values of C_F for various rpm's of the thruster. The value of 504 rpm is close to the value used in the current work, corresponding to a thrust of 10 N. The value of C_F given by Nienhuis for 504 rpm is 0.62. The computed value of C_F for the actuator disk approach is -0.24, while the value of C_F obtained from simulation with the thruster unit is -0.16. The negative sign in the computed results show a gain in thrust.

The conclusion is that the thruster unit gives a value of C_F closer to the value by Nienhuis although both numerical results are significantly different from to the experimental value. As noted before, the thruster geometries are different for the model tests and the computations. Also, as explained in section 3.2.1, the zero forward speed condition did not provide sufficiently converged solutions. These values of C_F are therefore computed at a small, non-zero forward speed. These factors must account for the variation in the results.

4 CFD study of the Hopper wedge

The Hopper wedge geometry is based on a Trailing Suction Hopper Dredger, and is given in Figure 4.1. The main particulars of the wedge are given in Table 4.1. As in the case of the Nienhuis wedge in the chapter 3, the thruster is approximated by an actuator disk as well as a propeller with hub and strut. Upon comparing the results from actuator disk approximation of the tunnel thruster and the use of a thruster unit, and considering the fact that the latter case takes more time to converge, the actuator disk approximation is given prominence. The use of the full propeller is restricted to a single case due to time constraints.

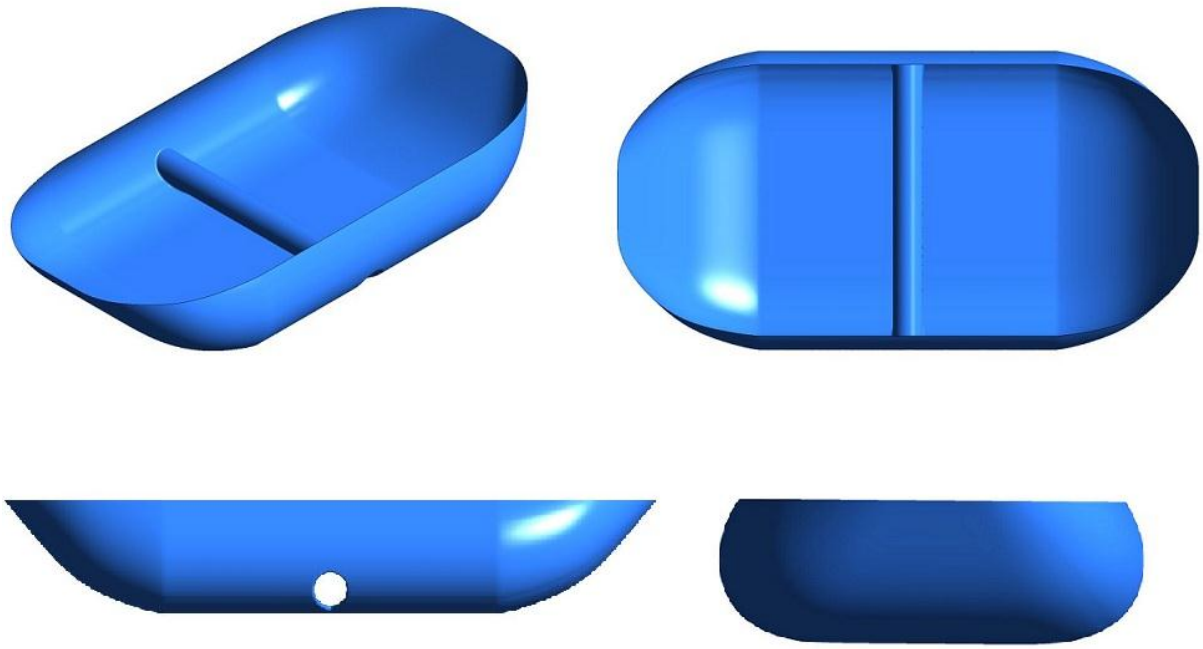

Figure 4.1 Hopper Wedge with straight tunnel

Particular	Symbol	Unit	
Length overall	L	[mm]	3100
Beam	B	[mm]	1506
Draft	T	[mm]	508
Tunnel diameter	D	[mm]	150
Tunnel center location above keel	z_{ref}	[mm]	109.6

Table 4.1 Particulars of the Hopper wedge

4.1 Simulations with the Hopper wedge

The grid convergence study from section 3.1.2 yielded an optimal grid for which the simulations thereafter were carried out for the Nienhuis wedge. The conclusions of the grid convergence study – the cell sizes for local mesh refinements - are used to mesh the Hopper wedge, so that in view of time a time-consuming convergence study is not repeated.

4.1.1 Computational Model

The computational domain and approach are as in section 3.1.1. The actuator disk geometry and dimensions are also the same as in Figure 3.4 and Table 3.2, except the center coordinates. Aside from the differences in geometry between the Nienhuis and Hopper wedges, other aspects of the computational model are the same in both cases.

The actuator disk for the Hopper wedge is first set to deliver a thrust of 1.78 N, for a forward speed 0.1 m/s, as in section 3.2. However, converged results could not be obtained for this value of thrust for the Hopper wedge even after a large number of time steps. At a higher thrust of 10 N, converged results were readily obtained and it was decided that the focus will be on this value of thrust. Simulations are then performed for a range of forward ship speeds. The cases with forward ship speed V_{ship} = 0.1 m/s, 0.2 m/s, 0.3 m/s and 0.4 m/s are considered. Two types of tunnel geometries are considered. At first, the geometry given in Figure 4.1, with a straight tunnel, is used in the numerical study. The loss of performance of the thrusters, as in the experiments, is attempted to be demonstrated. The actuator disk is then replaced by a thruster unit, as in section 3.4, with an rpm to deliver a thrust of approximately 10 N. The thruster unit is employed only for the forward speed of 0.4 m/s for comparison. Next, the inlet and outlet of the tunnel are bent forward (towards the bow) as shown in Figure 4.2 wherein the angle is 45^0 to the longitudinal axis. It is intended that the bent inlet provides a better inflow. At the outlet, the cross-flow is expected to counteract the bent jet flow and hence the low pressure on the hull associated with it. The forces are analyzed for both geometries and it is investigated whether the jet at an angle to the cross-flow improves the performance of the thruster at different forward speeds. The longitudinal (drag) force F_x and the transverse force on the hull F_y for straight and bent tunnel for each forward speed can be tabulated and compared, as in Table 4.11.

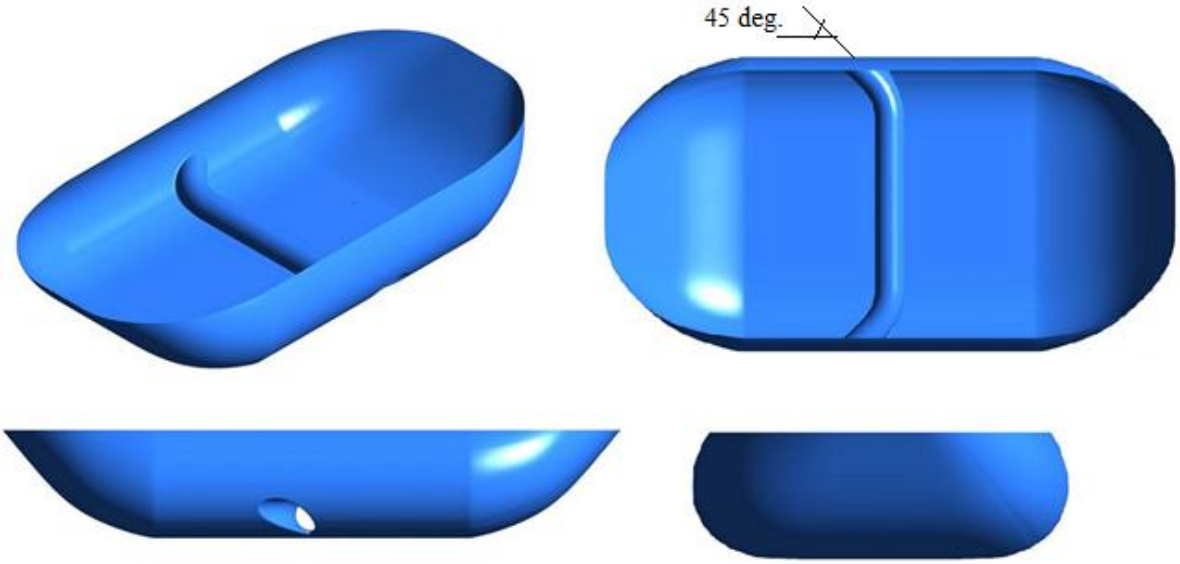

Figure 4.2 Hopper wedge with (45^0) bent tunnel

4.1.2 Results

Straight tunnel with Actuator disk

The velocity distributions and pressure distributions on the hull in case of the straight tunnel for ship speeds V_{ship} = 0.1 m/s, 0.2 m/s, 0.3 m/s and 0.4 m/s are given in Figure 4.4 through Figure 4.7. As in section 3.2.1, varying deflection of the jet is seen as forward speed varies. The pressure contours give an indication of the redistribution of pressure on the hull. As shown in

Figure 4.3, same as the case with Nienhuis wedge in Figure 3.16, the hull can be split into parts and the contribution of each towards the net transverse force can be tabulated. Tables 4.2 - 4.5 present the force contribution of each part in case of each forward ship speed.

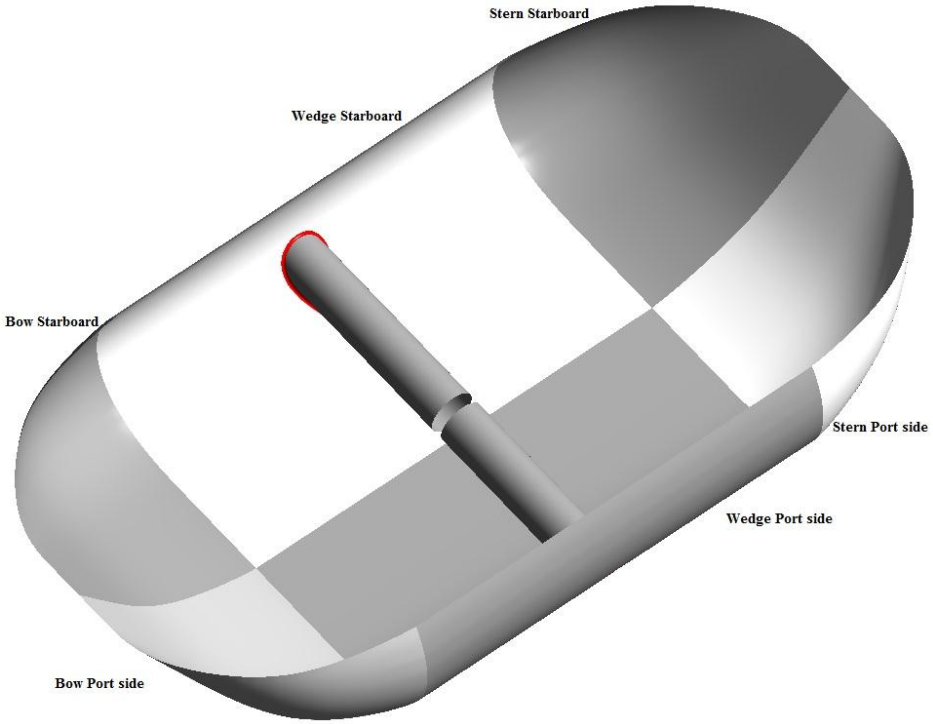

Figure 4.3 Hull split into parts for analysis of forces

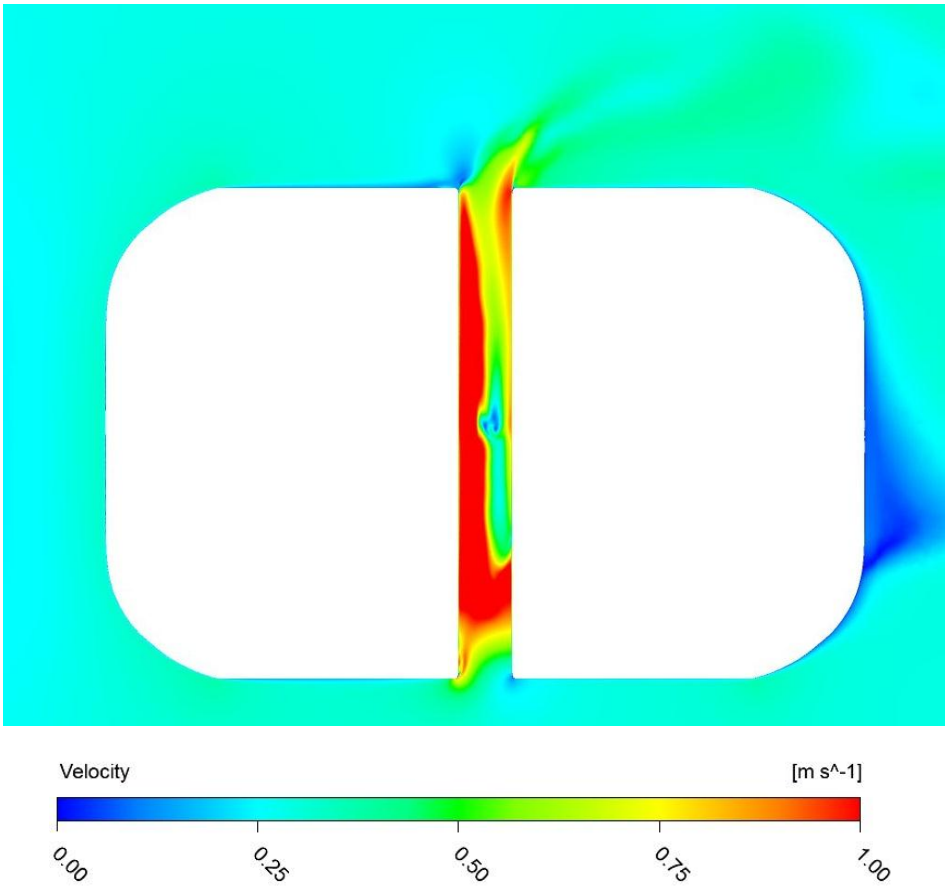

(a) Velocity magnitude distribution

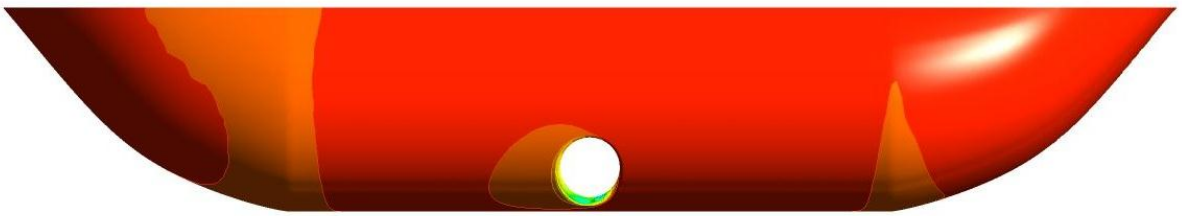

(b) Hydrodynamic pressure. The inlet side (Port)

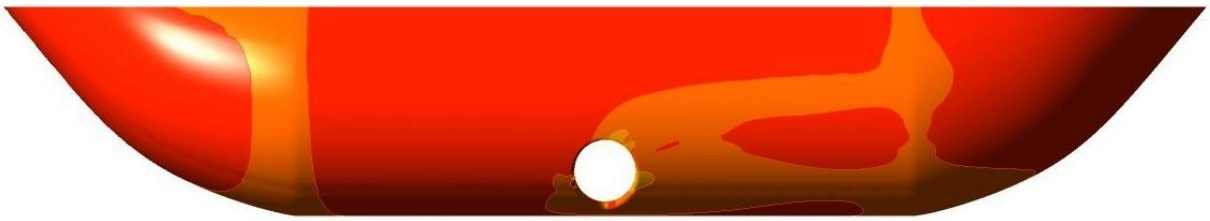

(c) Hydrodynamic pressure. The outlet side (Starboard)

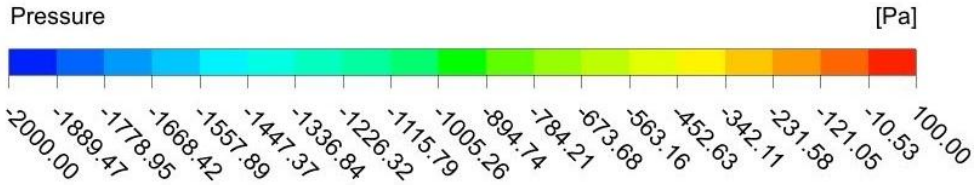

Figure 4.4 V_{ship} = 0.1 m/s, T = 10 N

	Bow [N]	Wedge [N]	Stern [N]	Tunnel end [N]	Tunnel [N]	
Port side	-1.100	-1.920	0.001	-2.600	-0.005	
Starboard	0.490	4.320	1.110	0.380	0.000	
Total [N]	-0.610	2.400	1.111	-2.220	-0.005	: 0.676

Table 4.2 Forces for V_{ship} = 0.1 m/s

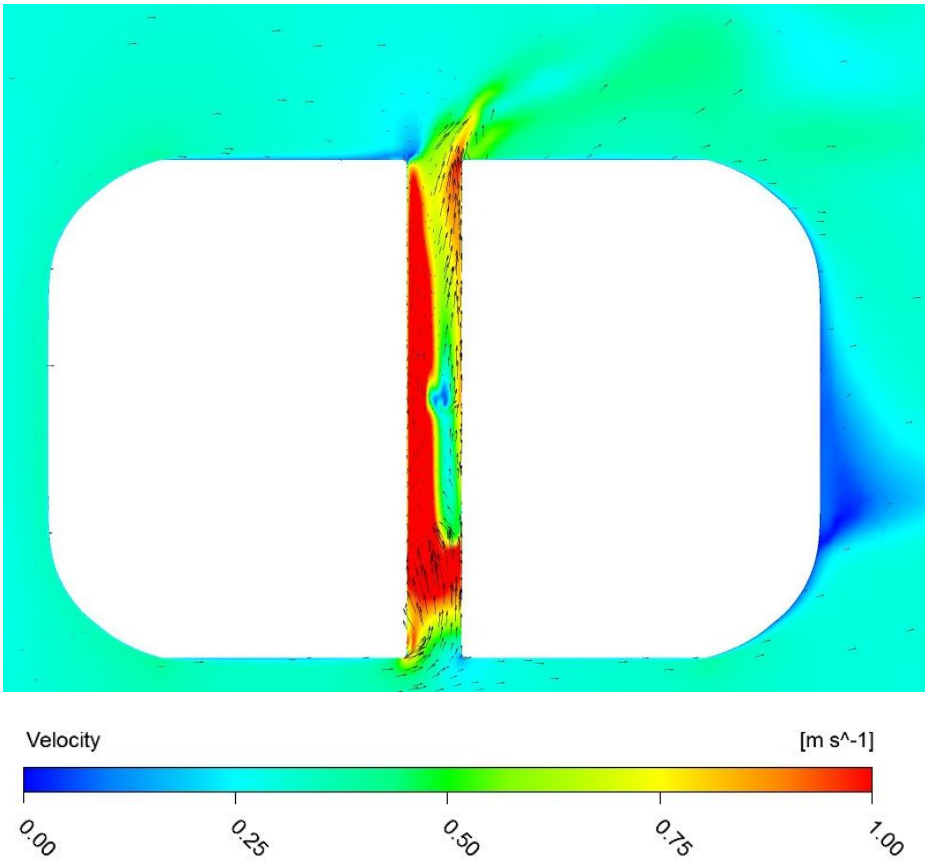

(a) Velocity magnitude distribution

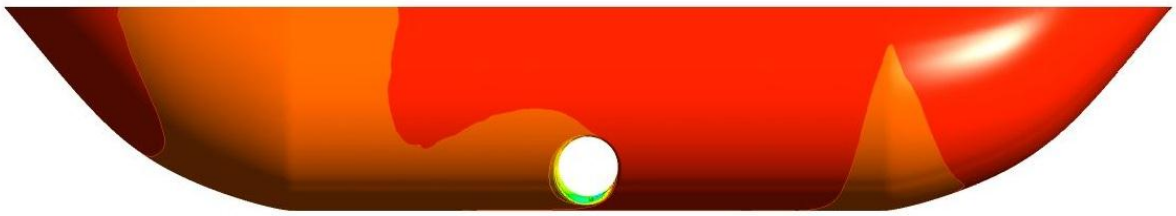

(b) Hydrodynamic pressure. The inlet side (Port)

(c) Hydrodynamic pressure. The outlet side (Starboard)

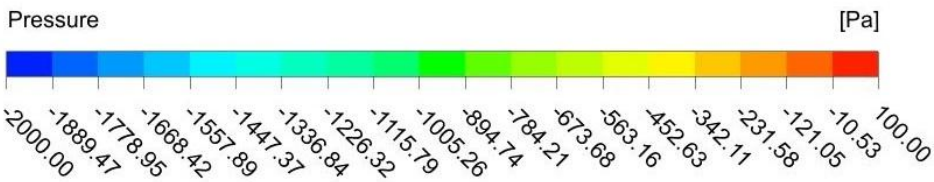

Figure 4.5 V_{ship} = 0.2 m/s, T = 10 N

	Bow [N]	Wedge [N]	Stern [N]	Tunnel end [N]	Tunnel [N]		
Port side	-3.19	-6.82	-1.08	-2.63	-0.01		
Starboard	2.54	9.00	2.22	0.44	0.00		
Total [N]	-0.65	2.18	1.14	-2.19	-0.01	:	0.47

Table 4.3 Forces for V_{ship} = 0.2 m/s

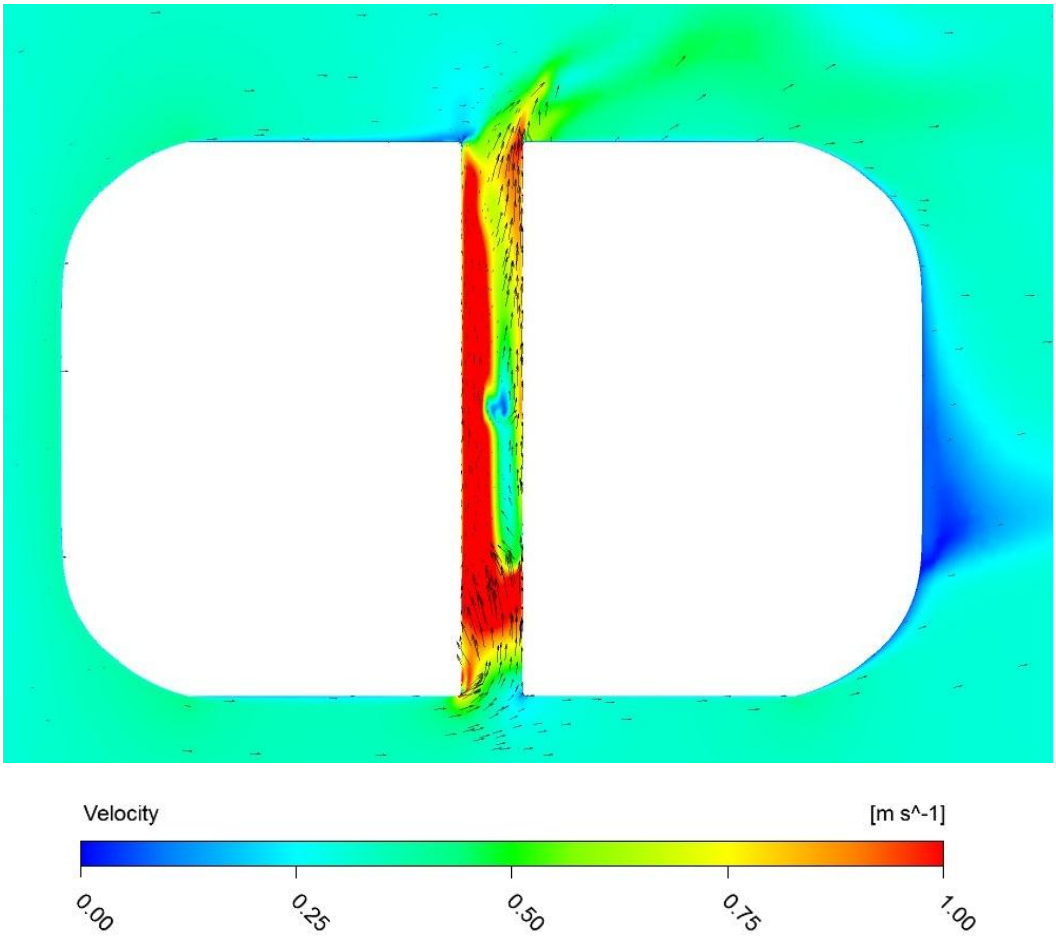

(a) Velocity magnitude distribution

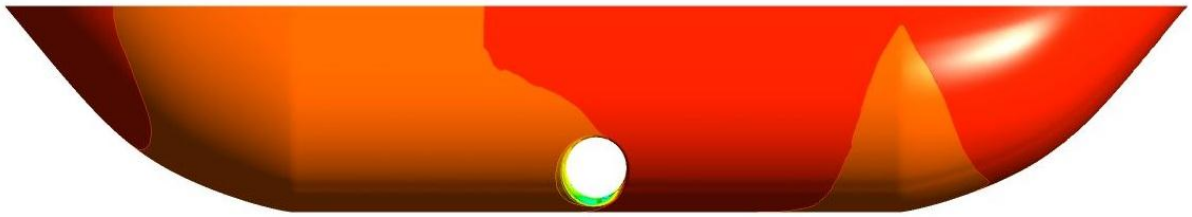

(b) Hydrodynamic pressure. The inlet side (Port)

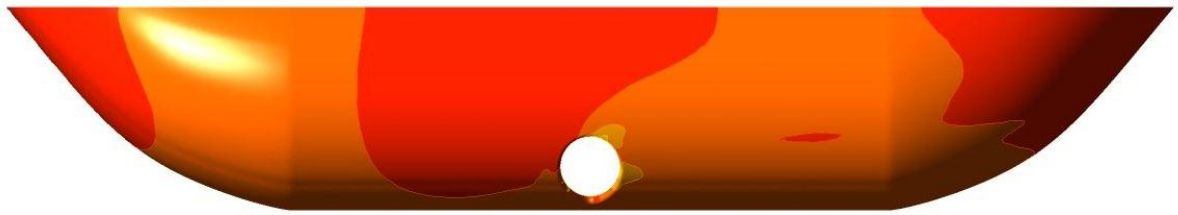

(c) Hydrodynamic pressure. The outlet side (Starboard)

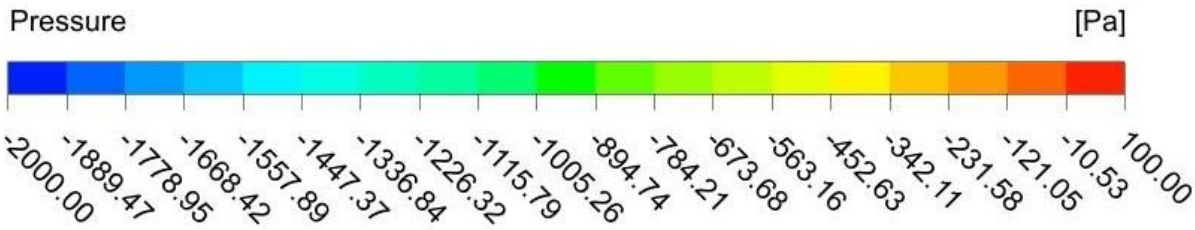

Figure 4.6 V_{ship} = 0.3 m/s, T = 10 N

	Bow [N]	Wedge [N]	Stern [N]	Tunnel end [N]	Tunnel [N]		
Port side	-4.21	-9.19	-1.61	-2.65	-0.01		
Starboard	3.54	11.33	2.84	0.46	0.00		
Total [N]	-0.67	2.14	1.23	-2.19	-0.01	:	0.50

Table 4.4 Forces for V_{ship} = 0.3 m/s

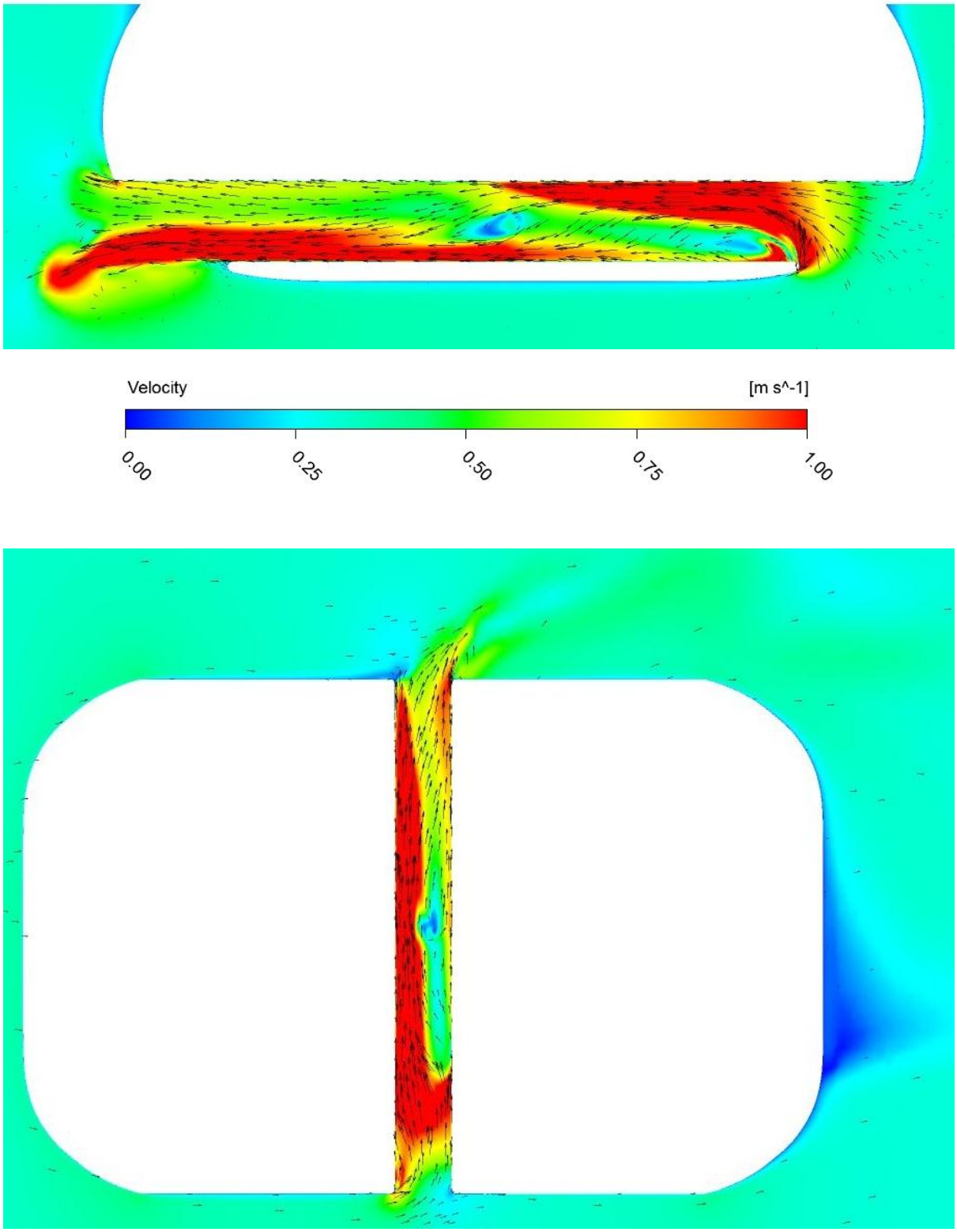

(a) Velocity magnitude distribution

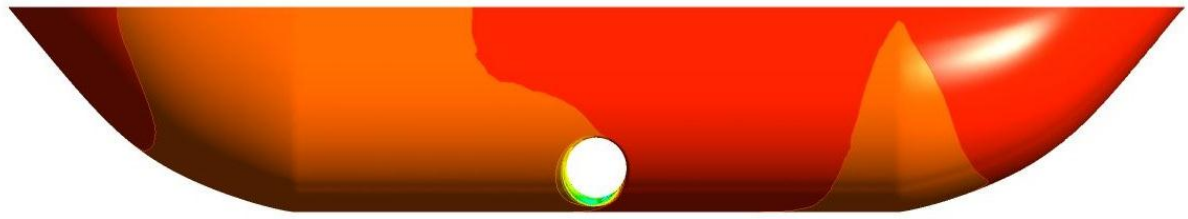

(b) Hydrodynamic pressure. The inlet side (Port)

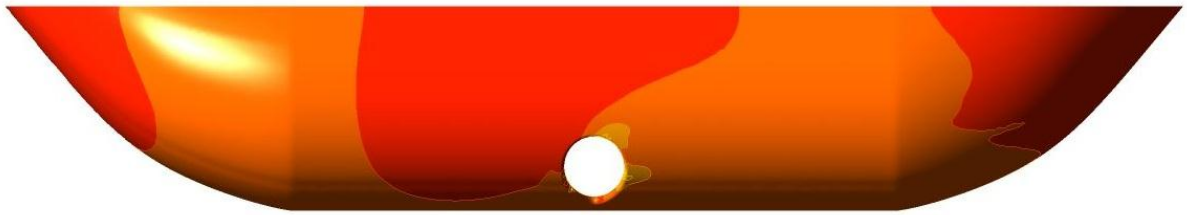

(c) Hydrodynamic pressure. The outlet side (Starboard)

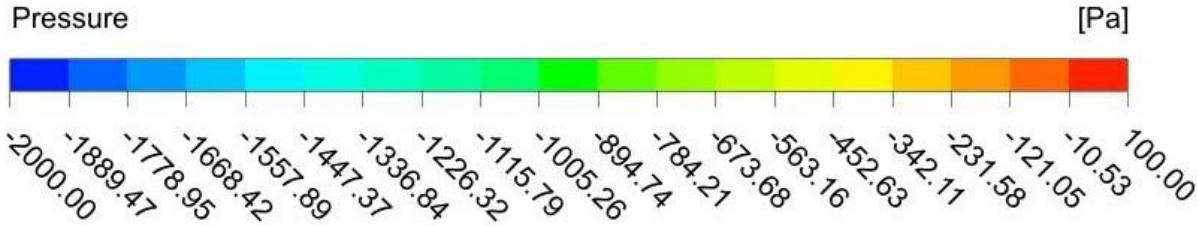

Figure 4.7 V_{ship} = 0.4 m/s, T = 10 N

	Bow [N]	Wedge [N]	Stern [N]	Tunnel end [N]	Tunnel [N]	
Port side	-4.260	-9.097	-1.560	-2.620	-0.005	
Starboard	3.540	11.000	2.750	0.485	0.000	
Total [N]	-0.720	1.903	1.190	-2.135	-0.005	: 0.233

Table 4.5 Forces for V_{ship} = 0.4 m/s

From Tables 4.2 – 4.5, it is observed that there is a loss of performance in all four ship speeds considered with a straight tunnel. The forces on the hull have positive signs which, according to sign conventions, implies that the net transverse forces oppose the thrust. This is in line with the experimental observation that a hopper suffered loss of thruster performance at forward speeds [6].

For V_{ship} = 0.1 m/s (Table 4.2), the major contribution to the net transverse force is from the wedge part, which has a high positive force contribution, and the tunnel ends which has a negative contribution comparable in magnitude to that of the wedge. The contribution at the stern is positive and is larger (in magnitude) compared to the negative contribution at the bow. The net transverse force is thus a small positive value, indicating a thrust deduction. Upon closer examination, it is seen that the force at the inlet (port) side of the wedge part has a negative sign is much smaller in magnitude than the positive force at the outlet (starboard) side. Also, the tunnel end at the inlet has a force with larger magnitude and negative sign when compared to the force at the outlet which has a small magnitude and positive sign. This means that the bending of the jet at the outlet (starboard) side results in a higher force on the wedge than the accelerating flow at inlet (port) side of the wedge. As for the tunnel ends, the accelerating inflow results in much higher force compared to the flow at outlet. The pressure contours in Figure 4.4 also indicates a redistribution of pressure which is consistent with the interaction of the bent jet at the starboard side of the wedge resulting in a higher magnitude of force at the region.

It is observed from Tables 4.3 – 4.5 that the distribution of forces in the different parts of the hull are similar for all ship speeds considered. The same reasoning is applicable in every case to explain the net transverse force with small magnitude and positive sign. Further, it is concluded that the transverse force F_y shows a decreasing trend as forward speed increases, i.e. the performance of the thruster increases as forward speed increases.

Straight tunnel with Thruster unit

The actuator disk is replaced by the thruster unit and simulations carried out for a propeller rotation speed of 625 rpm, corresponding to a thrust of 10 N, and the results compared with those by the actuator disk. The forward speed of 0.4 m/s is considered. The results are shown in Figure 4.8, and the transverse forces on various parts of the hull is as given in Table 4.6.

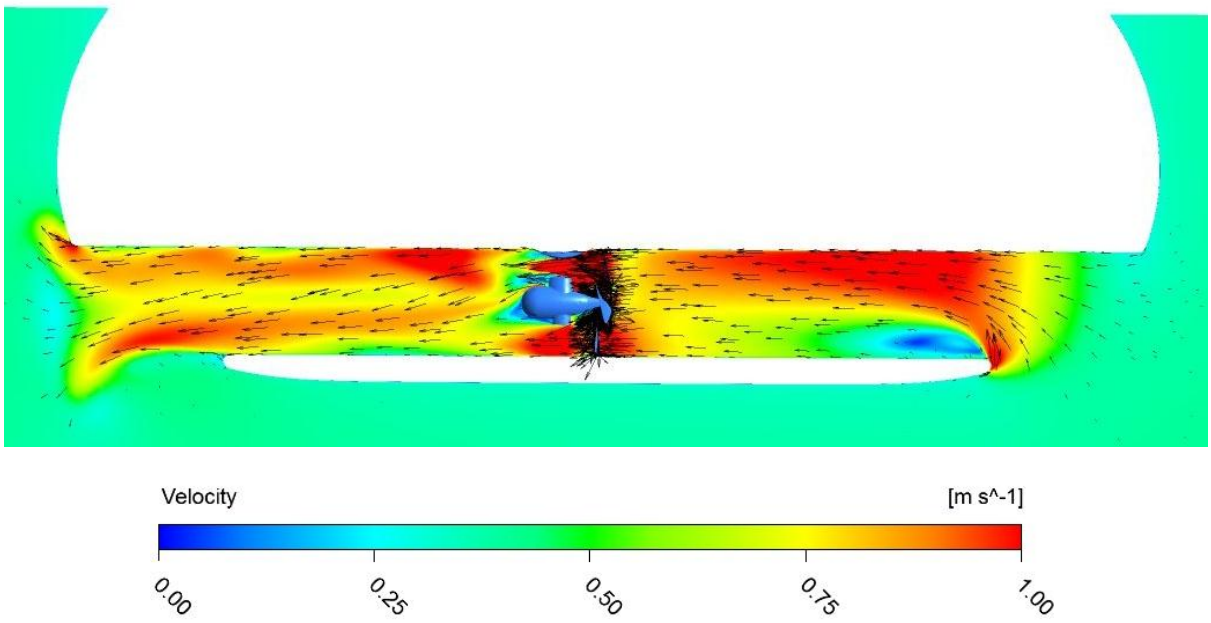

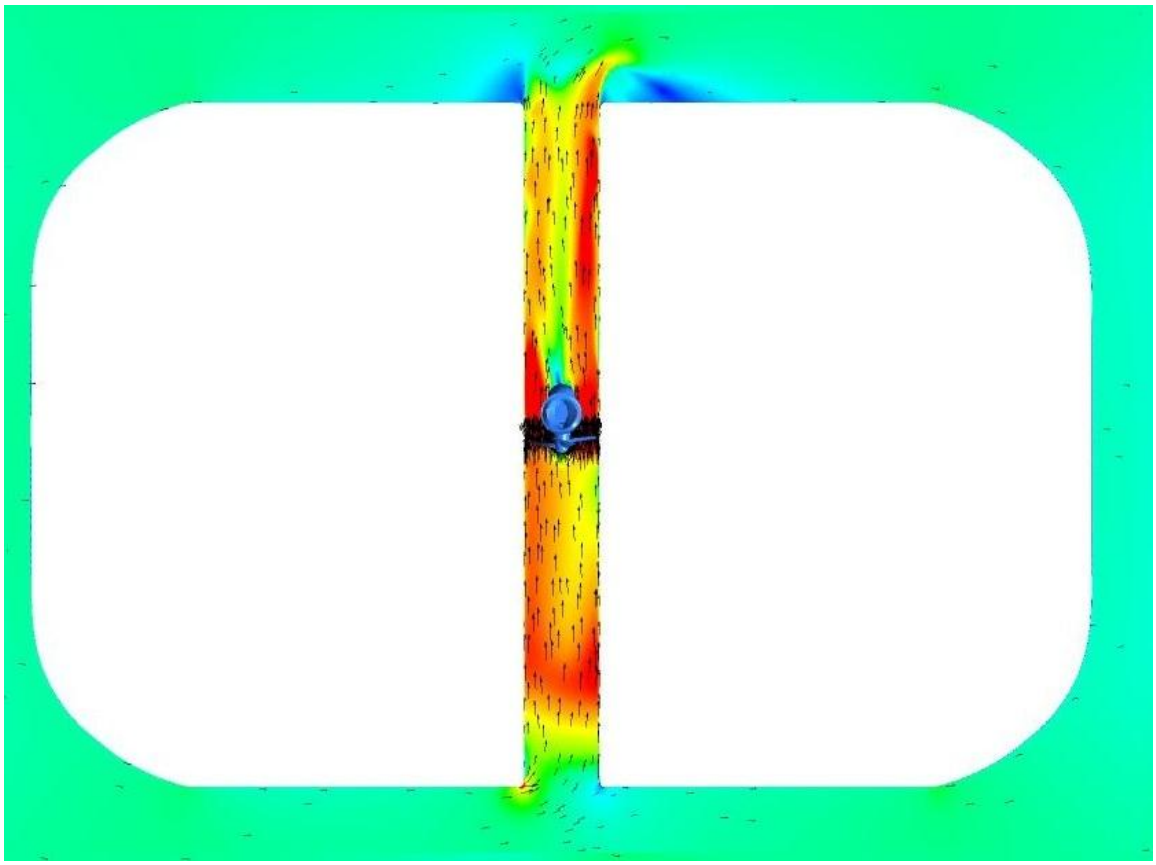

(a) Velocity magnitude distribution

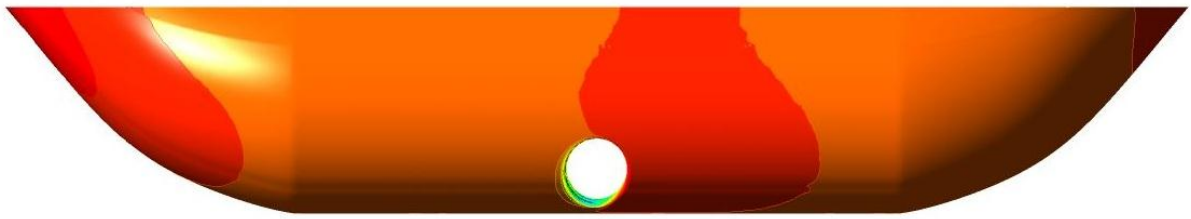

(b) Hydrodynamic pressure. The inlet side (Port)

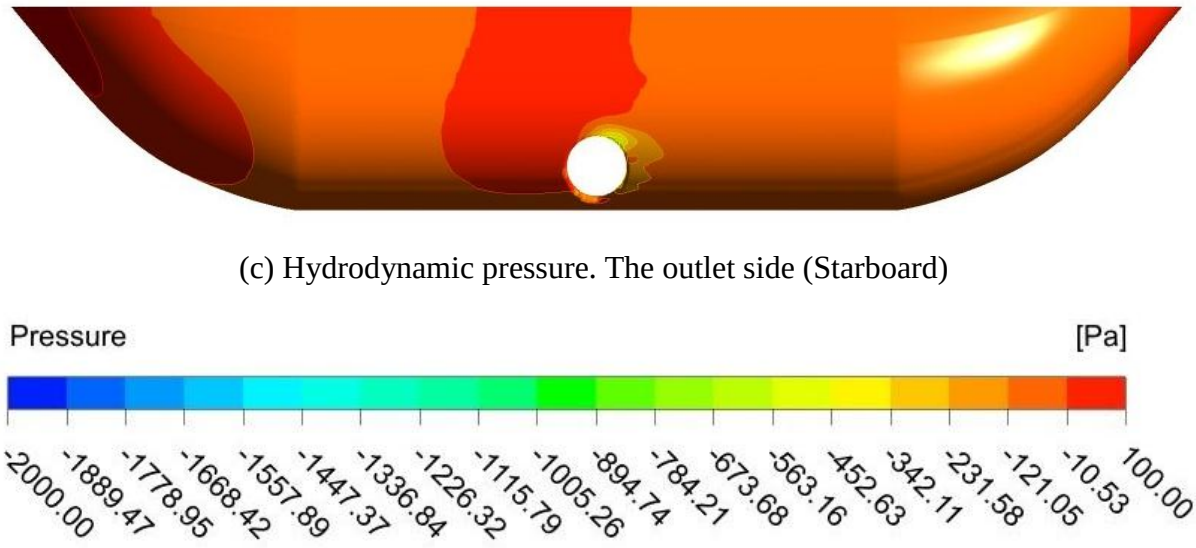

(c) Hydrodynamic pressure. The outlet side (Starboard)

Figure 4.8 V_{ship} = 0.4 m/s, 625 rpm

	Bow [N]	Wedge [N]	Stern [N]	Tunnel end [N]	Tunnel [N]		
Port side	3.00	-16.42	-10.96	-0.66	0.00		
Starboard	-2.27	14.67	10.70	2.97	0.00		
Total [N]	0.73	-1.75	-0.26	2.31	0.00	:	1.03

Table 4.6 Forces on the hull for 625 rpm

The results with the thruster unit can be compared with those with the actuator disk, in Figure 4.7 and Table 4.5. It is seen that while both cases indicate lowered thruster performance, the deduction in thrust, equal to the total transverse force F_y, is much higher with the thruster unit as compared to the actuator disk approach. The velocity magnitude distribution as well the pressure contours on the hull as shown in Figure 4.7 and Figure 4.8 also show significant qualitative variation. Upon comparing the distribution of forces in case of the actuator disk approach in Table 4.5 with that with the thruster unit in Table 4.6, the major contribution towards the net transverse force in the former case occurs at the outlet (starboard) side of the wedge. In the latter case, this contribution is concentrated at the tunnel end of the outlet side.

The difference can be attributed to the rotation that the thruster adds to the flow which is absent in the actuator disk approach. The presence of the hub and strut of the thruster unit also contributes to the difference in flow field.

Bent tunnel: 45^0

In order to investigate the possibility to improve tunnel thruster performance, the tunnel inlet and outlet are bent forward (as shown in Figure 4.2). This shape provides a more aligned inflow and, additionally, it directs the jet forward counteracting the jet bending off the outflow. It is investigated whether the resulting pressure distribution on the hull would aid or oppose the

thrust. The results are shown in Figures 4.9 through 4.12, and the forces on various parts of the hull are as given in Tables 4.7 through 4.10.

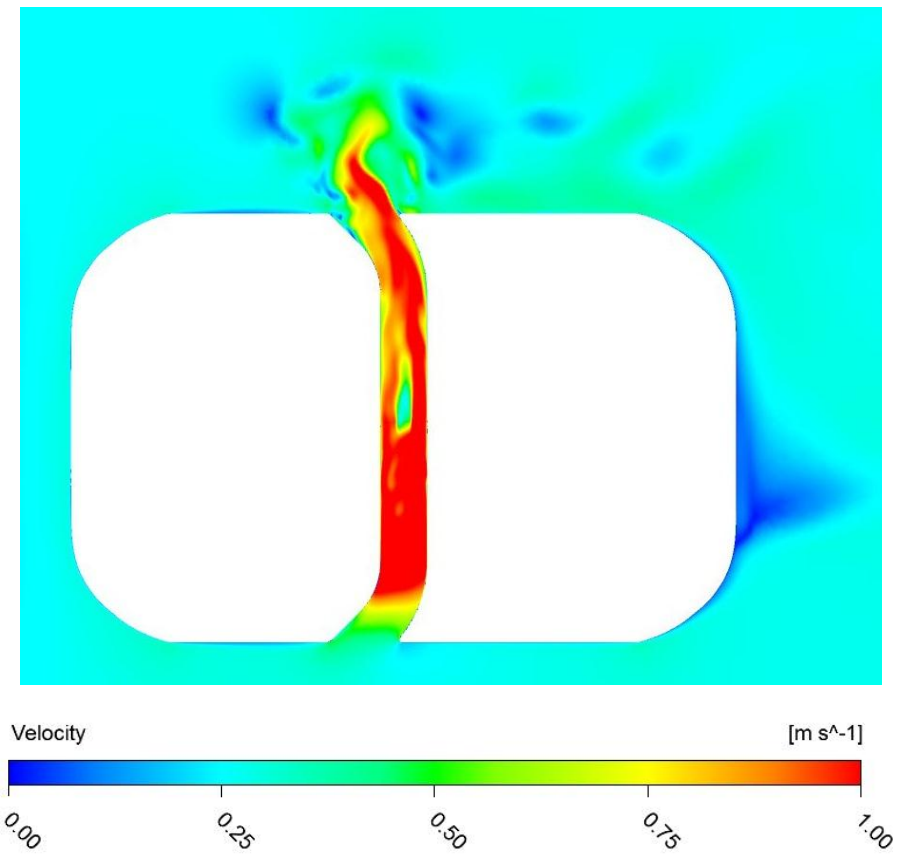

(a) Velocity magnitude distribution

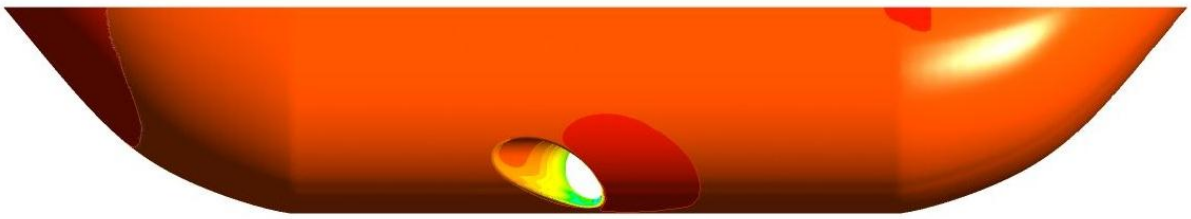

(b) Hydrodynamic pressure. The inlet side (Port)

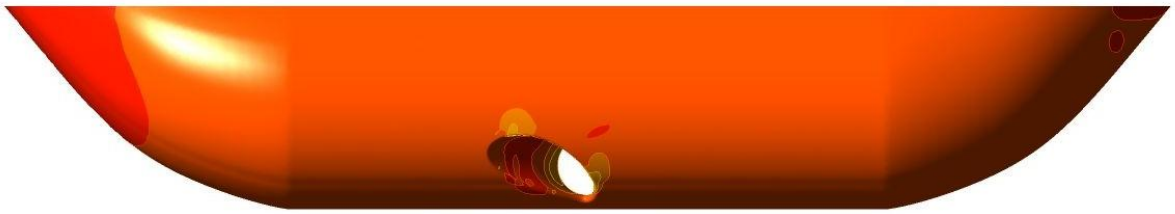

(c) Hydrodynamic pressure. The outlet side (Starboard)

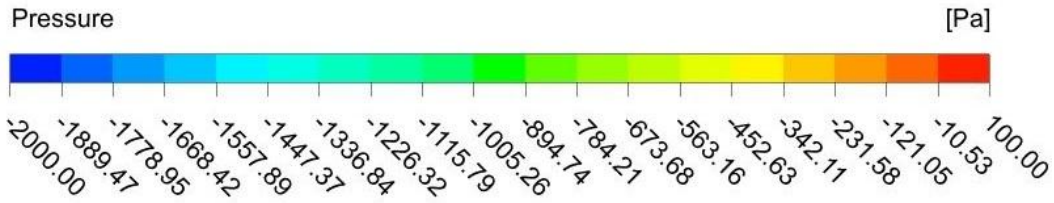

Figure 4.9 V_{ship} = 0.1 m/s, T = 10 N, bent tunnel

	Bow [N]	Wedge [N]	Stern [N]	Tunnel end [N]	Tunnel [N]	
Port side	1.010	3.940	1.170	-2.460	-2.460	
Starboard	-1.980	3.230	-0.180	0.160	1.510	
Total [N]	-0.970	7.170	0.990	-2.300	-0.950	: 3.940

Table 4.7 Forces for V_{ship} = 0.1 m/s, bent tunnel

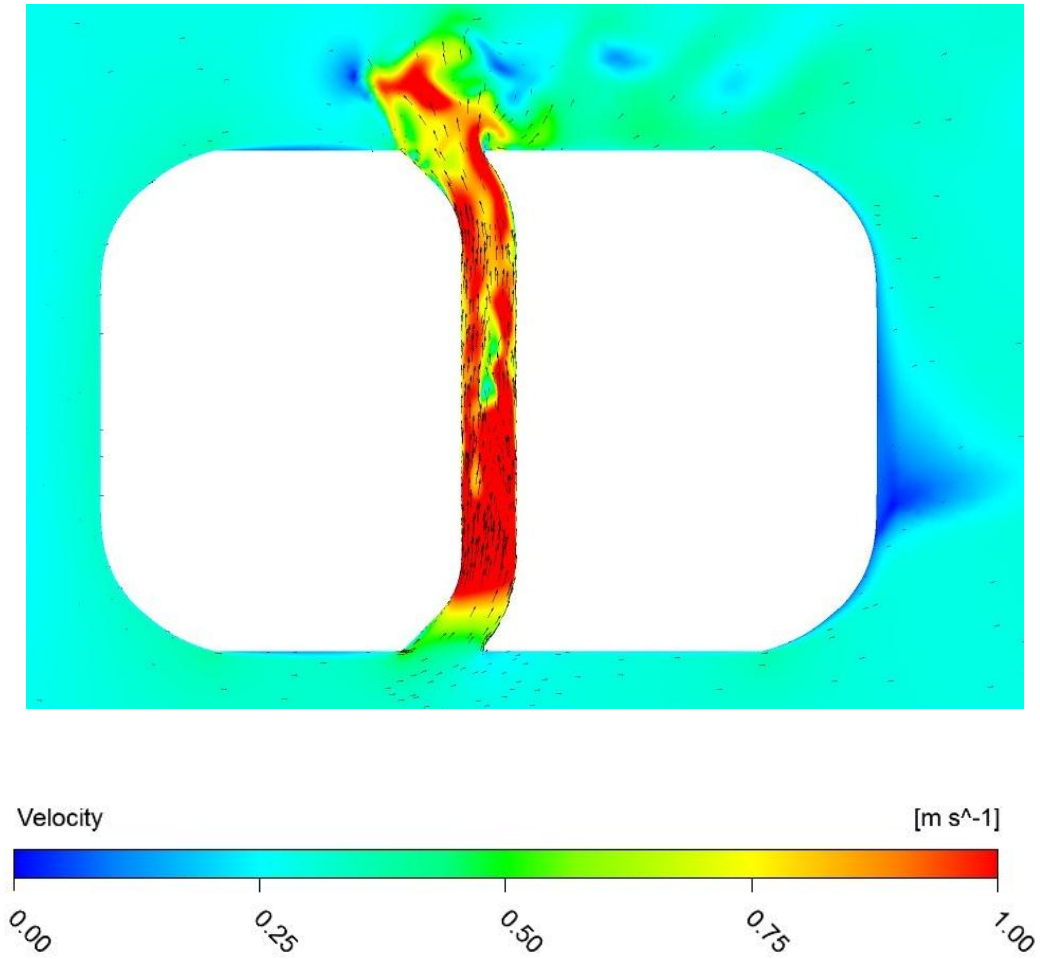

(a) Velocity magnitude distribution

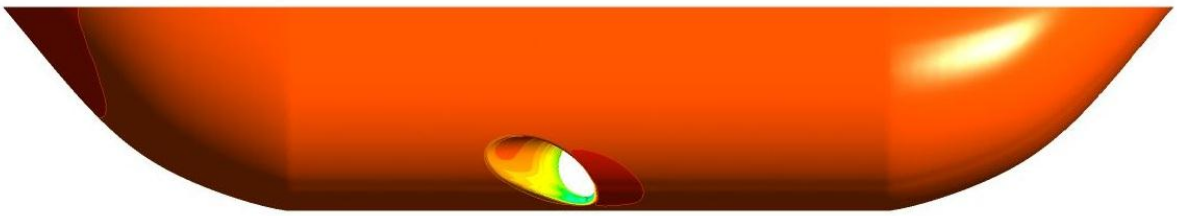

(b) Hydrodynamic pressure. The inlet side (Port)

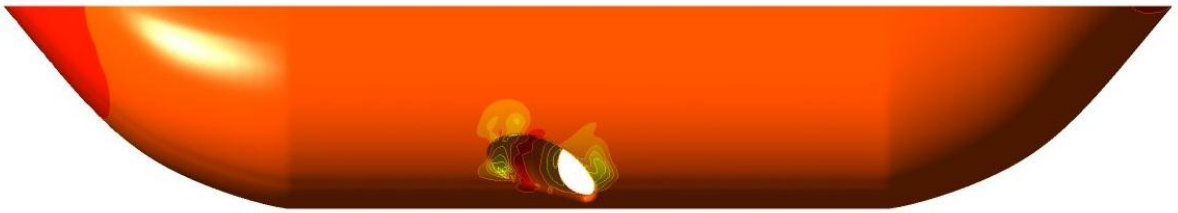

(c) Hydrodynamic pressure. The outlet side (Starboard)

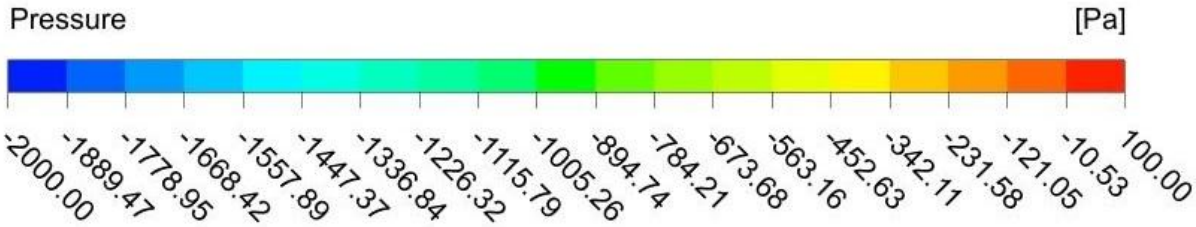

Figure 4.10 V_{ship} = 0.2 m/s, T = 10 N, bent tunnel

	Bow [N]	Wedge [N]	Stern [N]	Tunnel end [N]	Tunnel [N]		
Port side	-2.34	-4.17	-0.69	-2.61	-2.70		
Starboard	0.93	11.12	1.84	0.49	2.62		
Total [N]	-1.41	6.95	1.15	-2.12	-0.08	:	4.49

Table 4.8 Forces for V_{ship} = 0.2 m/s, bent tunnel

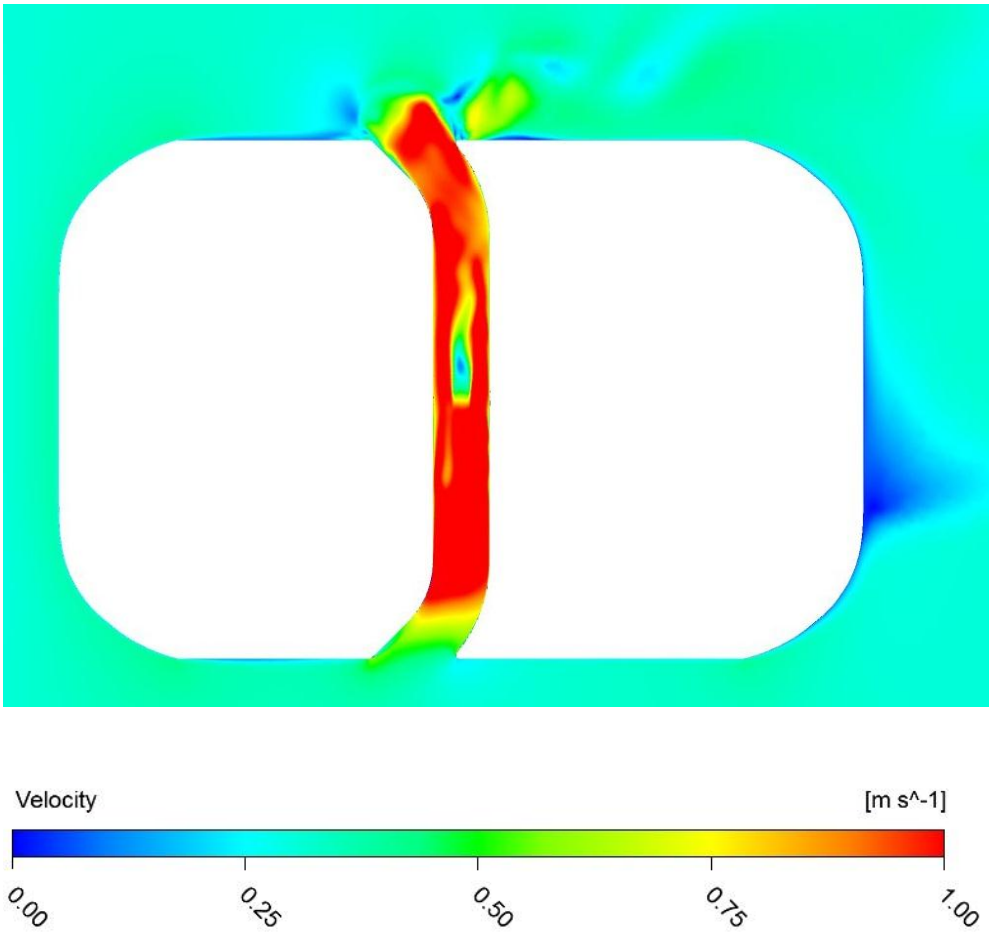

(a) Velocity magnitude distribution

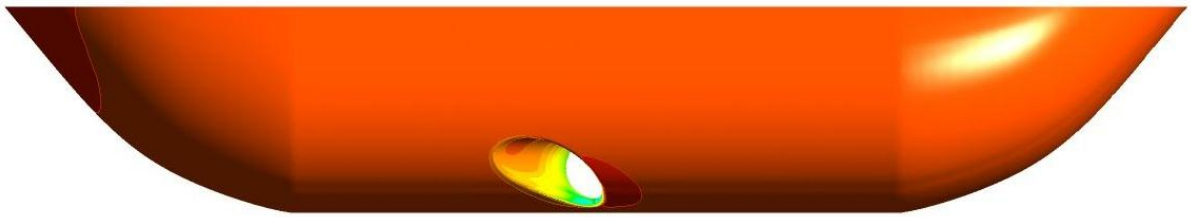

(b) Hydrodynamic pressure. The inlet side (Port)

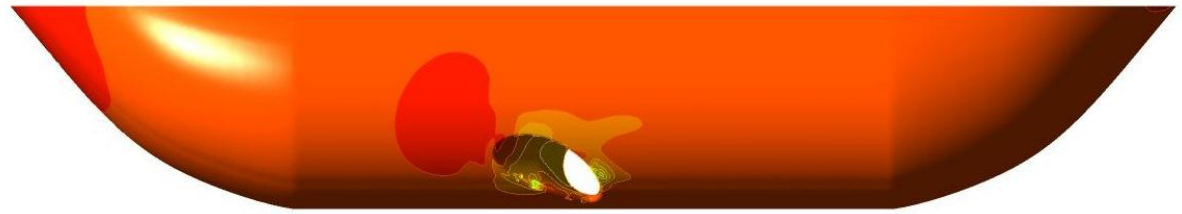

(c) Hydrodynamic pressure. The outlet side (Starboard)

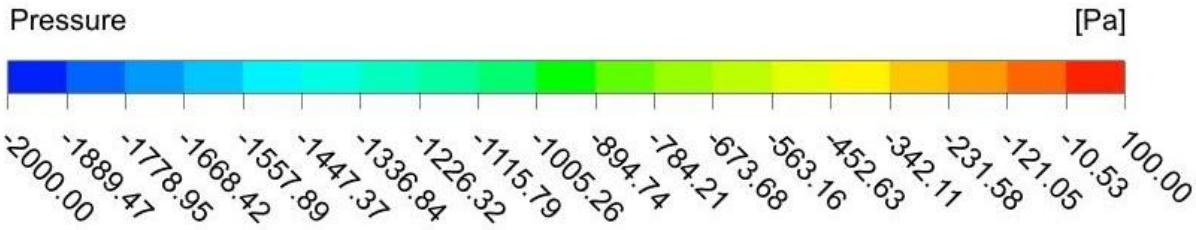

Figure 4.11 V_{ship} = 0.3 m/s, T = 10 N, bent tunnel

	Bow [N]	Wedge [N]	Stern [N]	Tunnel end [N]	Tunnel [N]	
Port side	-4.16	-8.66	-1.61	-2.69	-2.86	
Starboard	2.55	11.02	2.83	0.81	3.30	
Total [N]	-1.61	2.36	1.22	-1.88	0.44	: 0.53

Table 4.9 Forces for V_{ship} = 0.3 m/s, bent tunnel

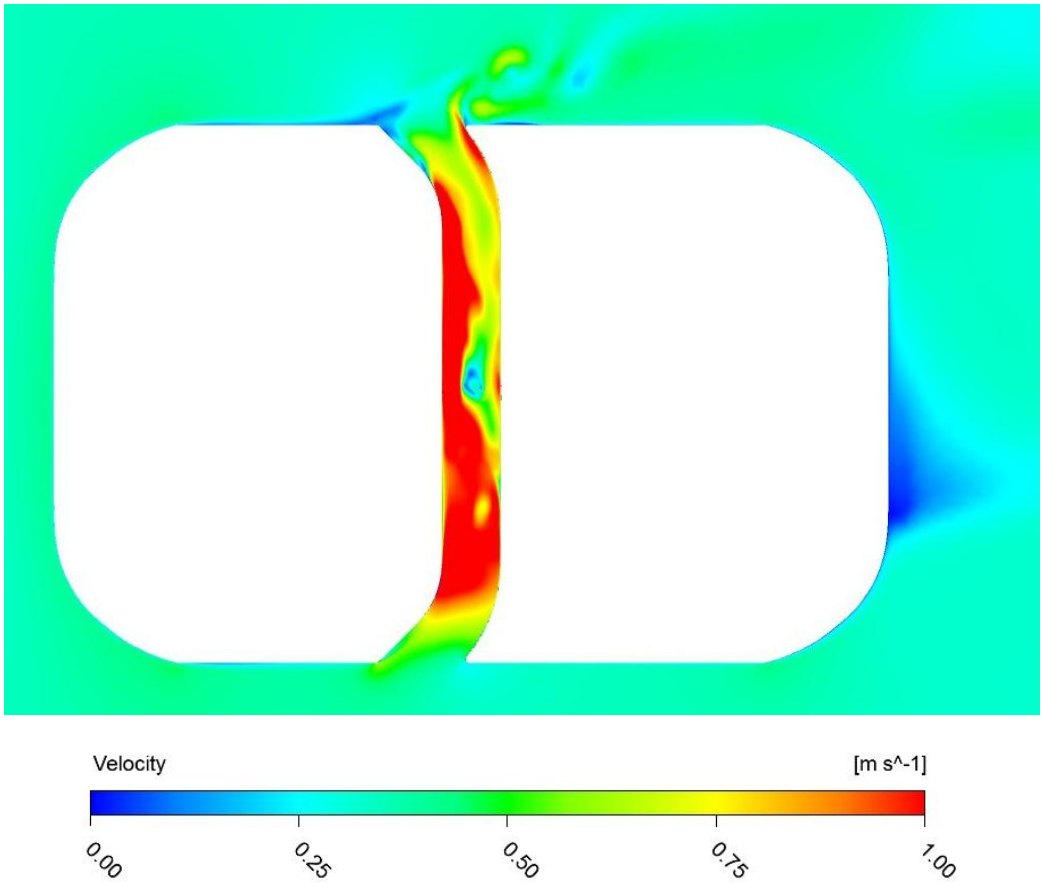

(a) Velocity magnitude distribution

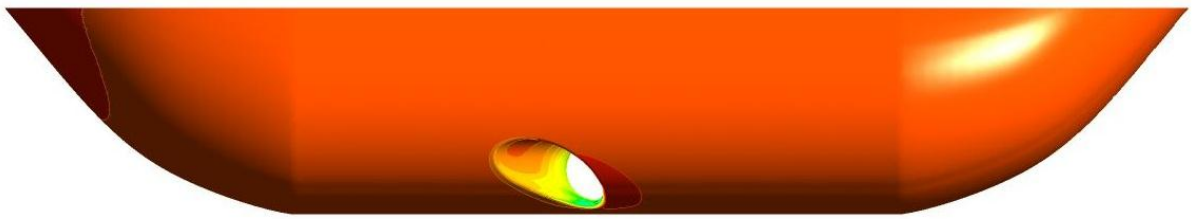

(b) Hydrodynamic pressure. The inlet side (Port)

(c) Hydrodynamic pressure. The outlet side (Starboard)

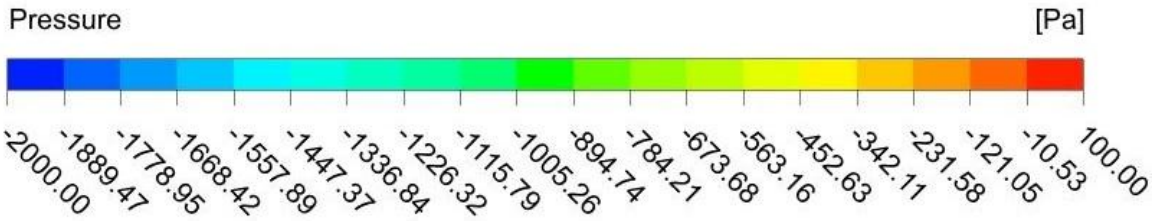

Figure 4.12 V_{ship} = 0.4 m/s, T = 10 N, bent tunnel

	Bow [N]	Wedge [N]	Stern [N]	Tunnel end [N]	Tunnel [N]	
Port side	-4.55	-9.24	-1.65	-2.38	-2.88	
Starboard	3.25	10.67	2.77	0.65	1.52	
Total [N]	-1.30	1.43	1.12	-1.73	-1.36	: -1.84

Table 4.10 Forces for V_{ship} = 0.4 m/s, bent tunnel

For V_{ship} = 0.1 m/s and V_{ship} = 0.2 m/s, it can be seen from Table 4.7 and Table 4.8 respectively that a large and decisive contribution to the net (positive) transverse force F_y is from the wedge part. Since the cross-flow is small in magnitude, the resulting jet is at an angle to the longitudinal. This results in high pressures forward of the outlet. The transverse force on the hull, F_y, has a high positive value indicating high thrust deduction.

In case of V_{ship} = 0.3 m/s, the relatively low, though positive, value of the transverse force on the hull indicates that the bent tunnel is advantageous only at higher forward speeds. This is further clear in the case V_{ship} = 0.4 m/s, wherein F_y is negative which implies a gain in thrust instead of deduction. From Table 4.9 and Table 4.10, it is seen that the forces at the outlet (starboard) side of the wedge remain large in magnitude and with positive sign. So, it is the variation of the forces at the inlet (port) side of the wedge that is decisive. The larger forward speed results in a better inflow into the tunnel, resulting in lower pressure forward of the inlet. This results in a force contribution with negative sign thus decreasing counteracting the force at the outlet side. Hence, with increasing forward speed, the net transverse force decreases.

The straight and bent tunnel can be compared in terms of the transverse force F_y as shown in Figure 4.13 and Table 4.11. There is a large difference in the variation of the transverse forces as seen in Figure 4.13. There is an interesting observation that at 0.3 m/s, the forces for

both tunnel geometries are nearly the same. Further investigation with smaller bending angles is needed to know whether an optimal angle can be obtained at which the deduction in thrust is minimal for the whole range of speeds.

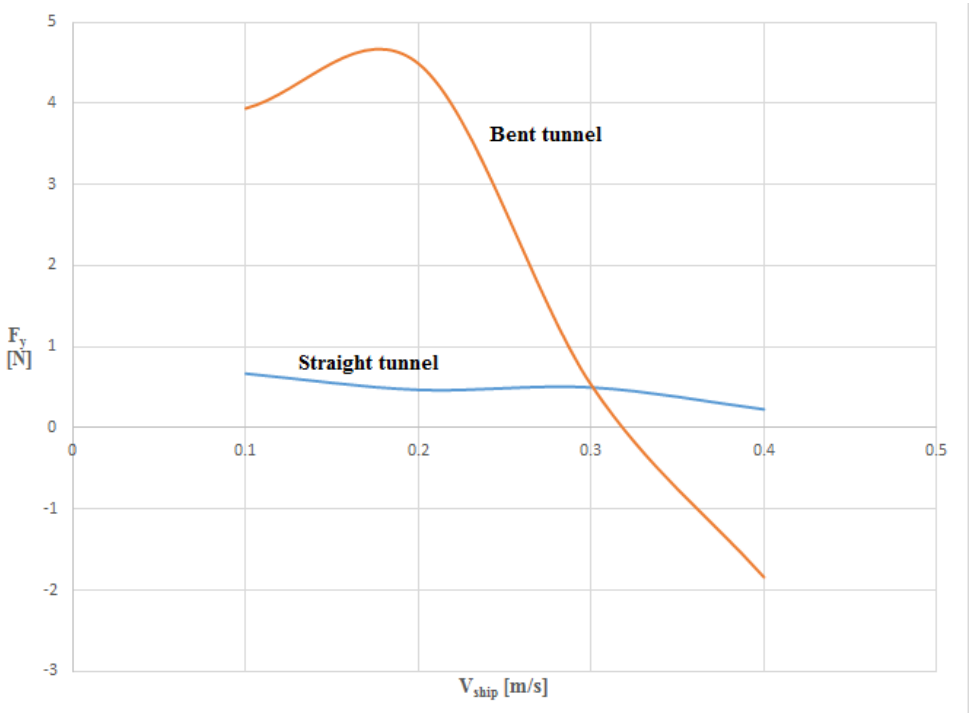

Figure 4.13 Variation of transverse forces with forward speed for straight and bent tunnels

	F_y [N]		F_x [N]	
V_{ship} [m/s]	Straight tunnel	Tunnel at 45^0	Straight tunnel	Tunnel at 45^0
0.1	0.67	3.94	12.49	20.91
0.2	0.47	4.49	10.32	19.53
0.3	0.5	0.53	9.93	19.44
0.4	0.23	-1.84	11.01	16.55

Table 4.11 Comparison of transverse and longitudinal forces for the two tunnel geometries

From Table 4.11, another factor which gains significance is the longitudinal (drag) force, F_x. A high increase in F_x is observed for each ship speed for the bent tunnel. It almost doubles in case of the bent tunnel in two smaller forward speed cases. The explanation must lie in the angle the jet makes with the longitudinal which results in a component of the thrust along the ship length, in the direction of the flow (i.e. positive x direction), which increases the net F_x.

5 Conclusions and Recommendations

In this work, a CFD study of bow tunnel thruster effectivity is performed using the general purpose finite volume based solver ANSYS CFX. The tunnel thruster operates with the vessel in slow forward speed conditions. The thruster is modelled by an actuator disk as well as a full thruster unit. The Nienhuis wedge, based on a containership, and the Hopper wedge, based on a trailing suction hopper dredger, are used in the study. Simulations are carried out for different thrusts, of the actuator disk, and rpm's, for the thruster unit, for varying forward ship speeds and the effectivity of the thruster is studied. In addition, the tunnel geometry of the Hopper wedge is altered by giving a forward bend of 45^{o} at the tunnel inlet and outlet and possible improvement in thruster performance is investigated.

5.1 Conclusions

The conclusions are provided for studies with the Nienhuis wedge and those with the Hopper wedge.

5.1.1 Conclusions for the Nienhuis wedge

It is shown by an initial grid convergence study, which did not result in a converged grid, that the sharp tunnel ends needed to be provided with fillets. With the sharp ends removed, the occurrence of flow separation at the location is minimised. A grid study then performed on the wedge resulted in an optimal grid to be used for further simulations.

In case of simulations with the actuator disk, the transverse force on the hull increases with increasing forward speed and indicated an increase in thruster performance. It is seen that the wedge behaves as a slender body in a flow, with the jet from the tunnel interacting with the cross-flow due to forward speed, resulting in a transverse force similar to Kutta-Joukowski lift. As such, there is a net transverse force in the direction of the thrust resulting in a gain in thruster effectivity. When a full thruster unit is used in place of the actuator disk, different the flow behaviour as well as the variation of the thruster performance with forward speed result. The rotation added to the flow by the modelled rotating thruster is one possible reason for the difference from the outcome of an actuator disk. Another reason is the inclusion of the hub and strut of the thruster unit that changes the geometry. Also, the thrust delivered is a function of both the rpm and the inflow to the thruster (which, in turn, depends on the forward speed). Since there is no straightforward relation to obtain the rpm required for a desired thrust at a given forward speed, the rpm corresponding to approximately the same thrust as desired will have to be arrived at by trial and error.

Upon comparison, the numerical results from both actuator disk approach and thruster unit differ significantly from experimental results by Nienhuis. A possible explanation lies in the fact that the hull used by Nienhuis was only a wedge, while a stern and a bow were attached to the wedge for stability in the numerical simulations. The numerical results with the thruster unit are closer to the experimental values than those with the actuator disk approach.

5.1.2 Conclusions for the Hopper wedge

In case of the Hopper wedge, for both actuator disk and thruster unit, the numerical results show lowering of thruster performance in forward speeds as observed in sea trials at Royal IHC. The redistribution of pressure on the hull due to bending of the jet from the thruster by the cross-flow due to the forward speed towards the hull results in a force that opposes the thrust, leading to reduced thruster effectivity. It is seen the transverse force on the hull, and hence the effectivity, decreases with increasing forward speed. It can be concluded that the increasing bending of the jet from the tunnel towards the hull (aftwards) contributes to the thrust deduction.

The tunnel is given a forward bend of 45^{o} at the inlet and outlet to investigate whether the bending of the jet by the cross-flow, towards the aft, can be counteracted and whether the effectivity improved. The inflow into the tunnel is also improved because of the bend. It is concluded that the forward bend improves thruster performance for high forward speeds. For lower speeds the tunnel jet results in high velocities forward of the tunnel outlet leading to a net transverse force opposing the thrust and lowered effectivity.

5.2 Recommendations

Based on the conclusions of the current work, several potential areas for further research are identified.

Further studies with the thruster unit

The thruster unit was not used extensively in simulations, especially in case of the Hopper wedge. It was observed from comparison that the numerical results from the Nienhuis wedge with the thruster unit were closer to the with the experimental results than those from the actuator disk approach. The thruster unit can therefore be used in further simulations with more combinations forward speed and rpm.

Rotation speed, forward speed and desired thrust

It was established that the thrust delivered by the thruster depends on not just its rpm but the forward speed as well. The relation used in section 3.4, based on the definition of the thrust coefficient, does not hold for a thruster in a tunnel especially when the inflow into the tunnel depends on the forward speed of the vessel. A relation between the rpm, forward speed and the desired thrust is beneficial in comparison with actuator disk approach wherein a constant thrust is delivered. The time-consuming trial and error approach with the rpm of the thruster to obtain a thrust approximately the same as the desired value can thus be avoided.

Frozen rotor vs Transient approach

In the current work, frozen rotor approach in ANSYS CFX is used to model the rotating flow field in case of simulations with the thruster unit. Frozen rotor method, a steady state approach that solves RANS equations, is less accurate compared to the Transient rotor-stator approach that solves unsteady RANS equations and also available in ANSYS CFX. Frozen rotor approach was chosen mainly because of time constraints. Application of the Transient method can be of interest if future studies demand that the transient effects be accounted for.

Smaller bending angles

In case of the Hopper wedge with the bending angles at tunnel inlet and outlet, improvement in thruster performance was observed only for high forward speeds. The angle of bending in the forward direction can be reduced and the effects studied. It is possible that an optimal angle will be found at which the thruster performance improves for the whole range of forward speeds.

Quantitative comparison with data from full-scale experiments

All computations herein are performed on model scale. Also, no experimental results were available for comparison in case of the Hopper wedge. If full-scale experiments are to be performed and the results available for comparison, numerical studies can be performed on full scale and verified.

Appendix A. SST-Menter turbulence model equations

The SST k-ω turbulence model [Menter 1993] is a two-equation eddy-viscosity model which blends k-ω and k-ε formulations. The use of a k-ω formulation in the inner parts of the boundary layer makes the model suitable to resolve the boundary layer. The SST formulation switches to a k-ε behaviour in the free-stream thereby avoiding the common k-ω issue of high sensitivity to the inlet free-stream turbulence properties.

The eddy viscosity μ_t is defined using turbulent kinetic energy K and the dissipation rate of the turbulent frequency ω as:

$$\mu_t = \frac{\frac{\rho K}{\omega}}{\max\left\{1, \frac{\Omega F_2}{a_1 \omega}\right\}} \tag{A.1}$$

where ρ is the density, F_2 is an auxiliary function, Ω is the absolute value of the vorticity and a_1 is taken as 0.31. F_2 is defined using wall distance d as:

$$F_2 = \tanh\left(\left[\max\left\{2\frac{\sqrt{K}}{0.09d\omega}, \frac{500\mu}{\rho d^2 \omega}\right\}\right]^2\right) \tag{A.2}$$

A blending function F_1 is used to blend between the k-ω and k-ε models:

$$F_1 = \tanh\left(\left[\min\left\{\max\left\{\frac{\sqrt{K}}{0.09d\omega}, \frac{500\mu}{\rho d^2 \omega}\right\}, \frac{4\rho\sigma_{\omega 2}\kappa}{CD_{\kappa\omega} d^2}\right\}\right]^4\right) \tag{A.3}$$

where

$$CD_{\kappa\omega} = \max\left\{\frac{2\rho\sigma_{\omega 2}}{\omega}\frac{\partial K}{\partial x_j}\frac{\partial \omega}{\partial x_j}, 10^{-20}\right\} \tag{A.4}$$

The transport equations are given as:

$$\frac{\partial \rho K}{\partial t} + \frac{\partial}{\partial x_j}\left(\rho U_j K - (\mu + \sigma_k \mu_t)\frac{\partial K}{\partial x_j}\right) = \tau_{tij} S_{ij} - \beta^* \rho \omega K \tag{A .5}$$

$$\frac{\partial \rho \omega}{\partial t} + \frac{\partial}{\partial x_j}\left(\rho U_j \omega - (\mu + \sigma_\omega \mu_t)\frac{\partial \omega}{\partial x_j}\right) = P_\omega - \beta \rho \omega^2 + 2\left(1 - F_1 \frac{\rho \sigma_{\omega 2}}{\omega}\frac{\partial K}{\partial x_j}\frac{\partial \omega}{\partial x_j}\right) \tag{A.6}$$

The production term P_ω is defined as:

$$P_\omega = 2\gamma\rho\left(S_{ij} - \frac{\omega S_{nn}\delta_{ij}}{3}\right)S_{ij} \tag{A.7}$$

The constants of the SST k-ω model are given as:

$$a_1 = 0.31 \qquad \beta^* = 0.09 \qquad \kappa = 0.41 \tag{A.8}$$

The coefficients of the k-ω models, ϕ_1, and k-ε model, ϕ_2, are blended as:

$$\phi = F_1 \phi_1 + (1 - F_1)\phi_2 \tag{A.9}$$

where $\phi = \{\beta, \gamma, \sigma_k, \sigma_\omega\}$. Table A.1 shows the constants.

Coefficient	ϕ_1 (k-ω model)	ϕ_2 (k-ϵ model)
σ_k [-]	0.850	1.000
σ_ω [-]	0.500	0.856
β [-]	0.075	0.083
$\gamma = \frac{\beta_1}{\beta^*} - \frac{\sigma_\omega \kappa^2}{\sqrt{\beta^*}}$ [−]	0.553	0.440

Table A.1. Constants used in the SST k-ω Menter model

Appendix B. Dimensional analysis of thrust

The length scale λ between the (full scale) vessel and the model is given by

$$\lambda = \frac{L_{full\ scale}}{L_{model}} \tag{B.1}$$

Froude scaling is assumed, i.e. the Froude number remains the same for both full and model scales.

$$\sqrt{\frac{V_{full\ scale}}{gL_{full\ scale}}} = \sqrt{\frac{V_{model}}{gL_{model}}}\ , \tag{B.2}$$

which gives

$$\frac{V_{full\ scale}}{V_{model}} = \sqrt{\frac{L_{full\ scale}}{L_{model}}} = \sqrt{\lambda} \tag{B.3}$$

M, L and τ being the mass, length and time scales for dimensional analysis, thrust is given as

$$T = ML\tau^{-2} \tag{B.4}$$

Given that $M \propto L^3$, the ratio of thrusts in full scale and model scale is given as:

$$\frac{T_{full\ scale}}{T_{model}} = \left(\frac{L_{full\ scale}}{L_{model}}\right)^3 \left(\frac{L_{full\ scale}}{L_{model}}\right)\left(\frac{\tau_{full\ scale}}{\tau_{model}}\right)^{-2} = \left(\frac{L_{full\ scale}}{L_{model}}\right)^2 \left(\frac{V_{full\ scale}}{V_{model}}\right)^2 = \lambda^3 \tag{B.5}$$

$$T_{full\ scale} = T_{model}\,\lambda^3 \tag{B.6}$$

Appendix C. Numerical uncertainty estimation

Uncertainty

The solution verification procedure by Eça and Hoekstra estimates the uncertainty U_ϕ of a functional or local quantity ϕ from the data obtained from n_g grids ($n_g \geq 4$). The method is based on power series expansions that neglect high-order terms and assume that ϕ has atleast second-order finite derivatives. It is also assumed that the lowest-order schemes used in the discretization are second or first-order accurate. U_ϕ is determined from an error estimate ϵ_ϕ times a safety factor F_s. The error is estimated (in the current work) as

$$\epsilon_\phi \simeq \delta_{12} = \phi_i - \phi_0 = \alpha_1 h_i + \alpha_2 {h_i}^2 \quad \text{(C.1)}$$

To assess the quality of the fit used to obtain ϵ_ϕ, a data range parameter is determined as

$$\Delta_\phi = \frac{(\phi_i)_{max} - (\phi_i)_{min}}{n_g - 1} \quad \text{(C.2)}$$

The uncertainty U_ϕ can be obtained from ϵ_ϕ and the safety factor F_s (= 3 in the present case) using the values of the standard deviation σ and Δ_ϕ to distinguish between "good" and "bad" error estimations:

- for $\sigma < \Delta_\phi$:
$$U_\phi(\phi_i) = F_s \epsilon_\phi(\phi_i) + \sigma + |\phi_i - \phi_{fit}| \quad \text{(C.3)}$$
- for $\sigma \geq \Delta_\phi$:
$$U_\phi(\phi_i) = 3\frac{\sigma}{\Delta_\phi}(\epsilon_\phi(\phi_i) + \sigma + |\phi_i - \phi_{fit}|) \quad \text{(C.4)}$$

Least-squares solutions of power series expansions

Non-weighted and weighted approaches are defined such that

- non-weighted approach:
$w_i = 1$ and $nw_i = 1$, w_i being the weights.
- weighted approach:
$$w_i = \frac{\frac{1}{h_i}}{\Sigma_{i=1}^{n_g} \frac{1}{h_i}} \quad \text{(C.5)}$$
so that $\Sigma_{i=1}^{n_g} w_i = 1$.

The two-term expansion with first and second order terms is given as

$$\phi_{fit} = \phi_0 + \alpha_1 h_i + \alpha_2 {h_i}^2 \quad \text{(C.6)}$$

ϕ_0, α_1 , and α_2 are determined from the minimum of the function

$$S_{12}(\phi_0, \alpha_1, \alpha_2) = \sqrt{\Sigma_{i=1}^{n_g} w_i (\phi_i - (\phi_0 + \alpha_1 h_i + \alpha_2 {h_i}^2))^2} \quad \text{(C.7)}$$

Setting $\frac{\partial S_{12}}{\partial \phi_0} = 0$, $\frac{\partial S_{12}}{\partial \alpha_1} = 0$, $\frac{\partial S_{12}}{\partial \alpha_2} = 0$ leads to a system of linear equations:

$$\begin{bmatrix} 1 & \Sigma_{i=1}^{n_g} w_i h_i & \Sigma_{i=1}^{n_g} w_i {h_i}^2 \\ \Sigma_{i=1}^{n_g} w_i h_i & \Sigma_{i=1}^{n_g} w_i {h_i}^2 & \Sigma_{i=1}^{n_g} w_i {h_i}^3 \\ \Sigma_{i=1}^{n_g} w_i {h_i}^2 & \Sigma_{i=1}^{n_g} w_i {h_i}^3 & \Sigma_{i=1}^{n_g} w_i {h_i}^4 \end{bmatrix} \begin{bmatrix} \phi_0 \\ \alpha_1 \\ \alpha_2 \end{bmatrix} = \begin{bmatrix} \Sigma_{i=1}^{n_g} w_i \phi_i \\ \Sigma_{i=1}^{n_g} w_i \phi_i h_i \\ \Sigma_{i=1}^{n_g} w_i \phi_i {h_i}^2 \end{bmatrix} \quad \text{(C.8)}$$

with standard deviation given by

$$\sigma_{12} = \sqrt{\frac{\Sigma_{i=1}^{n_g} n\, w_i (\, \phi_i - (\phi_0 + \alpha_1\, h_i + \alpha_2\, {h_i}^2))^2}{n_g - 3}} \quad \text{(C.9)}$$

Bibliography

[1] U. Nienhuis, *Analysis of thruster effectivity for dynamic positioning and low speed manoeuvring*, Ph.D. thesis, TU Delft, Delft University of Technology (1992).

[2] T. Schaap, *Changing the cross-sectional geometry of a bow tunnel thruster - Effects on the performance of the thruster at slow forward motion using Computational Fluid Dynamics*, Master Thesis, Faculty of Mechanical, Maritime and Materials Engineering, Delft University of Technology (2015).

[3] T. Schaap, *Changing the cross-sectional geometry of a bow tunnel thruster - Effects on the performance of the thruster at slow forward motion using Computational Fluid Dynamics*, Master Thesis Definition study, Faculty of Mechanical, Maritime and Materials Engineering, Delft University of Technology (2015).

[4] S. I Baniela, *The Performance of a Tunnel Bow Thruster with Slow Speed Ahead: A Revisited Issue*, Journal of Navigation 62, 631 (2009).

[5] P. Maciel, A. Koop and G. Vaz, *Modelling Thruster-Hull Interaction With CFD*, ASME 2013 32nd International Conference on Ocean, Offshore and Arctic Engineering, Volume 7: CFD and VIV, Nantes, France (2013).

[6] F. Lafeber, *CJK01 dredger (122 M); Bow thruster performance computations*, MARIN Report, Confidential report made for IHC 25868-1-POW (2014).

[7] J. L. Beveridge, *Bow-thruster jet flow*, Journal of Ship Research, 15:177-195 (1971).

[8] Ridley, D. E, *Effect of Tunnel Entrance Configuration on Thruster Performance*, SNAME paper, San Diego Section Technical Library (1967).

[9] Ridley, D. E, *Observations of the effect of vessel speed on bow thruster performance*, Marine Technology (1971).

[10] L. Eça and M. Hoekstra, *Verification and validation for marine applications of CFD*, International Shipbuilding Progress 60 (2013).

[11] L. Eça and M. Hoekstra, *A procedure for the estimation of the numerical uncertainty of CFD calculations based on grid refinement studies* , Journal of Computational Physics 262, 104 (2014).

[12] V. Karlikov and G. Sholomovich, *Some features of body-flow interaction in the presence of transverse jets*, Fluid dynamics 33, 3 (1998).

[13] J. C. Neitzel, M. Pergande, S. Berger and M. Abdel-Maksoud, *Influence of the numerical propulsion modelling on the velocity distribution behind the propulsion device and manoeuvring forces*, Fourth International Symposium on Marine Propulsors, Austin, Texas, USA. (2015).

[14] J. S. Carlton, *Marine propellers and propulsion*, Second Edition, Butterworth-Heineman, ISBN: 978-0-7506-8150-6 (2007).

[15] R. Th. Van Dijk and A. B. Aalbers, *"What Happens in Water" - The use of Hydrodynamics to Improve DP*, Dynamic Positioning Conference, Houston, Texas (2001)

[16] H. K. Versteeg and W. Malalasekera, *Introduction to Computational Fluid Dynamics, The Finite Volume Method*, Second edition, Pearson Education Limited, ISBN: 978-0-13-127498-3 (2007)

[17] ANSYS Inc., *ANSYS CFX Introduction*, Documentation for Release 15.0 (2013)

[18] ANSYS Inc., *ANSYS ICEM CFD Help Manual*, Documentation for Release 15.0 (2013)

[19] J. L. Beveridge, *Design and performance of bow thrusters*, Society of Naval Architects and Marine Engineers, New York Chesapeake Section, New York, USA (1972)

[20] S. B. Pope, *Turbulent Flows*, Cambridge University Press, ISBN: 9780521598866 (2000)

[21] MAN, *Basic Principles of Ship Propulsion*, MAN Diesel & Turbo, Denmark (2011)

[22] L. Yu, M. Greve, M. Druckenbrod, M. Abdel-Maksoud, *Numerical analysis of ducted propeller performance under open water test condition*, Journal of Marine Science and Technology (2013)

[23] B. B. Waterman, *Analysis of jet-crossflow interactions with applications to ship bow thrusters*, Master's thesis, Naval Postgraduate School, Monterey, California, USA (1980)

[24] J. de Jong, *Numerical modelling of Bow Thrusters at open quay structures*, Master's thesis, Delft University of Technology (2014)

[25] G. Wang, A. Schwoppe, R. Heinrich, *Comparison and Evaluation of cell-centered and cell-vertex discretization in the unstructured Tau-code for turbulent viscous flows*, European Conference on Computational Fluid Dynamics, Lisbon, Portugal (2010)

[26] G. Venkatachalapathy, *Performance Prediction of Power Recovery Turbines with combined 1D-CFD methods*, Master's thesis, Delft University of Technology (2016)